Spring 2011

Synthesis of ALD Zinc Oxide and Thin Film Materials Optimization for UV Photodetector Applications

Kandabara Nouhoum Tapily
Old Dominion University

SYNTHESIS OF ALD ZnO AND THIN FILM MATERIALS OPTIMIZATION

FOR UV PHOTODETECTOR APPLICATIONS

by

Kandabara Nouhoum Tapily
B.S. May 2006, Old Dominion University

A Dissertation Submitted to the Faculty of Old Dominion University in Partial Fulfillment of the Requirements for the Degree of

DOCTOR OF PHILOSOPHY

ELECTRICAL AND COMPUTER ENGINEERING

OLD DOMINION UNIVERSITY
May 2011

Approved by:

Helmut Baumgart (Director)

Gon Namkoong (Member)

Ravindra Joshi (Member)

Zhili Hao (Member)

ABSTRACT

SYNTHESIS OF ALD ZnO AND THIN FILM MATERIALS OPTIMIZATION FOR UV PHOTODETECTOR APLLICATIONS

Kandabara Nouhoum Tapily
Old Dominion University, 2011
Director: Dr. Helmut Baumgart

Zinc oxide (ZnO) is a direct, wide bandgap semiconductor material. It is thermodynamically stable in the wurtzite structure at ambient temperature conditions. ZnO has very interesting optical and electrical properties and is a suitable candidate for numerous optoelectronic applications such as solar cells, LEDs and UV-photodetectors. ZnO is a naturally n-type semiconductor. Due to the lack of reproducible p-type ZnO, achieving good homojunction ZnO-based photodiodes such as UV-photodetectors remains a challenge. Meanwhile, heterojunction structures of ZnO with p-type substrates such as SiC, GaN, NiO, AlGaN, Si etc. are used; however, those heterojunction diodes suffer from low efficiencies. ZnO is an n-type material with numerous intrinsic defect levels responsible for the electrical and optical behaviors. Presently, there is no clear consensus about the origin of those defects.

In this work, ZnO was synthesized by atomic layer deposition (ALD). ALD is a novel deposition technique suitable for nanotechnology engineering that provides unique features such as precise control of ZnO thin film with atomic resolution, high uniformity, good conformity and high aspect ratio. Using this novel deposition technique, the ALD ZnO deposition process was developed and optimized using diethyl zinc as the precursor for zinc and water vapor as the oxygen source. In order to optimize the film quality for use in electronic applications, the physical, mechanical and electrical properties were

investigated. The structural and mechanical properties of the ALD ZnO thin films were investigated by X-ray diffraction (XRD), transmission electron microscopy (TEM), atomic force microscopy (AFM), scanning electron microscopy (SEM), spectroscopic Ellipsometry, X-ray photoelectron spectroscopy (XPS), Raman spectroscopy, UV-VIS absorption and nanoindentation. The electrical characterizations were performed using C-V, I-V, DLTS, Hall Effect, and four-point probe.

The intrinsic defects responsible for the electrical and optical properties of the ALD ZnO films were analyzed and identified. ALD ZnO based electronic devices were fabricated, optimized and their electrical characteristics measured. The photocurrent characteristics of ALD ZnO were also optimized, and high efficiency UV-photodetectors were achieved.

To my parents Nouhoum Tapily and Oumou Yalcoue for their unconditional love and support.

ACKNOWLEDGMENTS

I would like to thank my advisor Professor Helmut Baumgart for his guidance and financial support. His expertise made this work possible. I am grateful for having the opportunity to work on several projects and the knowledge I gained in these past few years working with him.

I would like to also thank my advisory committee: Dr. Gon Namkoong, Dr. Ravindra Joshi and Dr. Zhili Hao for their contribution to this work. My gratitude extends to Dr. Diefeng Gu and my colleagues, Patrick Boland, Kurniawan Foe and Pragya Shresta for their help during experimental work at the Applied Research Center. I would like to thank Dr. Sylvain Marsillac and Dr. Jaetae Seo for their help in some of the characterization techniques such as quantum efficiency and Raman spectroscopy. My gratitude goes to Dr. Abdelmageed Elmustafa for his help and teaching about the nanomechanical properties of very thin films. I would like to thank Prof. Sacharia Albin for his guidance and for introducing me to the microelectronics. My gratitude also extends to the administrative staff in the ECE department and at the Applied Research Center, especially to Pamela Foshee.

This work wouldn't be possible without the love, support and patience of my friends and family. To my family Nouhoum and Oumou Tapily, Tandou Tapily, Aly Tapily, Mariam Tapily, Barka Toure, Sylvia Morrings, Wanda Edwards, Kimberly Edwards, and Robert Edwards, this work wouldn't be possible without your unconditional love and support. Thank you.

Last but not least, to 'Coumba Ndoye, a special thanks and gratitude for her support and help throughout this dissertation.

NOMENCLATURE

AFM = Atomic Force Microscope

ALD = Atomic Layer Deposition

TEM = Transmission Electron Microscopy

SEM = Scanning Electron Microscope

XPS = X-ray Photoelectron Spectroscopy

CVD = Chemical Vapor Deposition

PVD = Physical Vapor Deposition

MBE = Molecular Beam Epitaxy

ZnO = Zinc Oxide

Si = Silicon

Ar = Argon

N_2 = Nitrogen

CSM = Continuous Stiffness Measurement

DEZ = Diethyl Zinc

Zn_i = Zinc interstitial

V_o = oxygen vacancy

V_{Zn} = Zinc vacancy

DI = Deionized Water

β = correction factor for Berkovich indenter

ν_s = substrate Poisson's ratio

ν_i = indenter Poisson's ratio

E_s = substrate Young's modulus

E_i = indenter Young's modulus

E_{eff} = Film's effective modulus

H= Meyer's hardness

E_{hv}= energy of a photon

K= Boltzmann's constant = 1.38×10^{-23} J/K

q = electron charge = 1.6×10^{-19} C

h= Planck's constant = 6.626×10^{-34} m^2kg/s

A^{**} = Richardson's constant

T = temperature in ^{o}K

c= Speed of light = 3×10^{8} m/s

TABLE OF CONTENTS

Page

LIST OF TABLES

LIST OF FIGURES

CHAPTER 1

INTRODUCTION

1.1 Material Properties

ZnO is a wide bandgap, II-VI semiconductor. ZnO crystallizes in either a cubic or hexagonal structure. The three known crystal structures of ZnO are zincblende, rocksalt and wurtzite structure. The first two are cubic while the latter is hexagonal. The wurtzite crystal structure of ZnO is the thermodynamically stable form of ZnO at ambient temperature conditions. The wurtzite structure has a unit cell with two lattice parameters a and c. Like most wurtzite crystal structure materials, ZnO belongs to the hexagonal system with space group C_{6v}^4 ($P6_3mc$) with two formula units per primitive cell, where all atoms occupy C_{3v} sites.[1] Each Zn atom is surrounded by four O atoms and each O atom is surrounded by four Zn atoms. Figure 1 shows a schematic configuration of the wurtzite of ZnO.

ZnO exhibits many technologically important properties such as piezoelectric, ferromagnetic properties. ZnO reveals high resistivity in the order of $\sim 10^{12}$ Ω-cm when doped with Li ions. ZnO has many technologically interesting properties such as piezoelectric, ferroelectric, ferromagnetic properties that can be modulated by doping with transition metals. ZnO is thermochromic. These properties make ZnO an ideal candidate for spintronics, medical applications such as ointments and sun screen lotion, solar cells, UV light-emitting diodes, sensors, surface acoustic devices, transparent electronics like those in transparent thin film transistor and transparent conductive electrodes. ZnO is a good and less expensive alternative to indium tin oxide (ITO).[2] A

comparison of key properties of ZnO and the leading competing wide bandgap semiconductor materials is displayed in Table 1. With a binding energy of 60 *meV*, lasing operation can occur in ZnO even at room temperature. The high binding energy and relatively inexpensive processing cost give ZnO an edge over GaN (with a band energy ~3.4 *eV*) for LED applications. ZnO exhibits superior UV emissions.[3] The undoped ZnO has a bandgap of ~3.4 *eV*. This bandgap can be modulated according to the doping level with various dopants. Magnesium doping increases the bandgap of ZnO.[4] However doping ZnO with CdO decreases the bandgap.[5] Consequently, one can tune the bandgap to applications where a range of wavelengths is required or to cut off undesired wavelengths. In addition, ZnO is very stable under ionizing radiation making it a suitable candidate for optical applications in outer space.

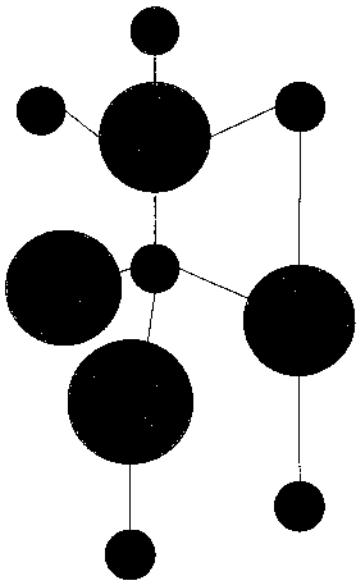

Figure 1. Wurtzite structure of ZnO showing tetrahedral bonding. Blue spheres (or larger spheres) represent Zn atoms and red spheres (smaller spheres) represent O atoms.

Various forms of ZnO such as single crystal bulk, thin films, powder, and nanostructures such as nanotubes,[6] nanosheets, [10] needles,[7,8] nanorods, [9] shells, [11] ribbons, [10] and tetrapods [11] can be synthesized by numerous techniques. Some of the growth techniques used to deposit ZnO are sputtering,[12] pulsed laser deposition, [13,14] electrochemical decomposition,[15] thermal evaporation,[9] vapor liquid phase,[16] metal organic chemical vapor deposition (MOCVD), [17] molecular beam epitaxy (MBE)[18] and, most recently, atomic layer deposition (ALD). [19,20]

Table 1. Comparison of keys parameters of most studied wide bandgap materials.[21]

Material	Crystal structure	Lattice parameter a(Å) c(Å)	Bandgap energy (*eV*)	Energy of cohesion (*eV*)	Energy of fusion (^{o}K)	Excitonic binding (*meV*)	Dielectric constant ε(0)
ZnO	Wurtzite	3.25 5.21	3.37	1.89	2248	60	8.75
ZnS	Wurtzite	3.82 6.26	3.8	1.59	2103	30	9.6
ZnSe	Zincblende	5.66	2.7	14.29	1793	20	9.1
GaAs	Zincblende	5.65	1.43			4.2	
GaN	Wurtzite	3.19 5.19	3.39	2.24	1973	21	8.9
6H-SiC	Wurtzite	3.18 15.12	2.86	3.17	>2100	-	9.66

Although ZnO has been studied for decades, it is attracting more attention due to its optical properties. It exhibits visible emission, such as green, yellow, and red/orange emission, due to the presence of intrinsic and extrinsic defect levels in the ZnO film. In fact, the emission wavelengths in ZnO photoluminescence can be modulated according to the defect levels present in the film.

1.2 Defects in ZnO

Defect related luminescence in ZnO occurs in three main bands: green luminescence, yellow luminescence and red/orange luminescence. The green emission occurs at ~2.3 *eV* or at a wavelength of 510 *nm*. The yellow emission occurs at 2.1 *eV* or at a wavelength of 570 *nm*. The red/orange emission occurs at 1.8 *eV* or at a wavelength of 650 *nm*.[22] Despite the well known emission at the green, yellow and red wavelengths, there remains great controversy about the origins of those emissions. Green emission is thought to be due to the transition of a singly ionized oxygen vacancy and a photo excited hole,[23] transition between an electron close to the conduction band and a deeply trapped hole at a doubly ionized oxygen vacancy,[24] and surface defects.[25] Yellow/red-orange emission is associated with excess oxygen.[26] Different surface treatments have been proposed in order to reduce the defect level and to study their effects on the photoluminescence. Roy et al.[27] have demonstrated that the introduction of water was found to reduce the defect related luminescence. Hydrogen is an impurity that is always found in ZnO due to the current growth techniques. Hydrogen acts as a shallow donor when incorporated into ZnO. Incorporating hydrogen leads to a weakening of the donor-bound exciton line at 3.62 *eV*.

Visible emissions in ZnO are due to intrinsic and extrinsic defects. Defects in ZnO are usually zinc interstitials (Zn_i), oxygen vacancies (V_o), hydrogen, dislocations, carbonates, and hydrogen carbonates. Intrinsic defects are either elemental impurities, such as hydrogen, or structural defects in the ZnO crystal lattice such as Zn_i, V_o and V_{Zn}, and dislocations. These defects are also called deep-level defects. The intrinsic defects,

which are found about 0.01-0.05 *eV* below the conduction band, are referred to as shallow defect levels

The two most common intrinsic defects found in ZnO are oxygen and zinc vacancies and interstitials. An oxygen vacancy has a lower formation energy than a Zn interstitial. Therefore, a region with a higher concentration of zinc has a higher oxygen vacancy concentration. In an oxygen rich region, zinc vacancy concentration is higher. Defect related emission in ZnO is also dependent on the sample preparation techniques. Deposition parameters such as pressure, temperature, and flow rate, influence the defect types and concentrations which in turn affect visible photoluminescence emission. Due to the variety of the defects and the fact that defects can exist both at the sub-lattice level and in different charge states, interpreting experimental results becomes complex. Another defect type in ZnO is hydrogen. Hydrogen easily diffuses in ZnO and attaches itself to an oxygen atom forming an OH group. H atoms always act like donors. It is thought hydrogen defect level in ZnO is responsible for the undoped n-type conductivity.[28]

Extrinsic defects in contrast are due to intentional impurities introduced to change the optical and electrical properties of the material. The common dopants in ZnO include Li, Na, Cu, N, P and As. Cu doping is effective in enhancing the green luminescence. Li and the group I elements are used as p-type dopants. Because of their small radii, group I elements tend to occupy interstitial sites and become donors instead of acceptors and consequently contribute to the n-type conductivity. The native defect levels tend to compensate for the effect of dopants. In order to form a p-type ZnO, it is important to keep the formation energy of donor-type defects very low. P-type ZnO still remains an

interesting challenge to overcome. However, it was found that N-doped ZnO exhibits p-type conduction.[29]

1.3 Photodiodes

A Diode is a two terminal semiconductor device consisting of a single p-n junction. When the p-type material and the n-type material composing the diode are the same, the diode is called a homojunction diode. An example is a Si diode. A heterojunction diode is formed with a p-n junction made of different materials, for example a GaAs/AlGaAs diode. At equilibrium with no external voltage applied, a depletion region forms in a p-n junction due to the diffusion and drift of electron and holes. The electrons diffuse to the p region and the holes diffuse to the n region where they constitute minority carriers. Consequently, a region depleted of charge carriers forms near the metallurgical junction, hence the depletion region is created. The diffusion of holes and electrons from the junction leaves ionized acceptors and donors in the depletion region. The negatively charged acceptors are fixed near the p-region while the positively charged donors are fixed near the n-region. Thus, a built-in voltage develops in the depletion region. The built-in voltage gives rise to an electric field with a maximum at the junction. A photodiode is a diode that converts incident light into electric current.

Figure 2 shows a schematic of a p-n junction diode at equilibrium, and under positive and negative biases. Positive bias reduces the depletion while negative bias increases the depletion region. The effect of the voltage bias on the energy bands and diode characteristics will be discussed in detail in later chapters. The total current of the p-n junction is equal to the sum of the diffusion and drift current. At thermodynamic equilibrium without external bias, the drift current is equal to the diffusion current

resulting in a zero flow of current. When photons of energy E_{hv} greater than the bandgap E_g of the semiconductor material, for example for Si E_g = 1.1 *eV* and for ZnO E_g = ~3.4 *eV*, are absorbed in the material electron-hole pairs are generated. The electrons and holes are separated by the electric field that acts across the depletion region. The electrons and holes that are generated within the depletion width diffuse into the depletion region. Electrons are collected in the n region and the holes to the p region. When the photodiode is electrically connected, a current flows. The generated current, photocurrent, is proportional to incident light.

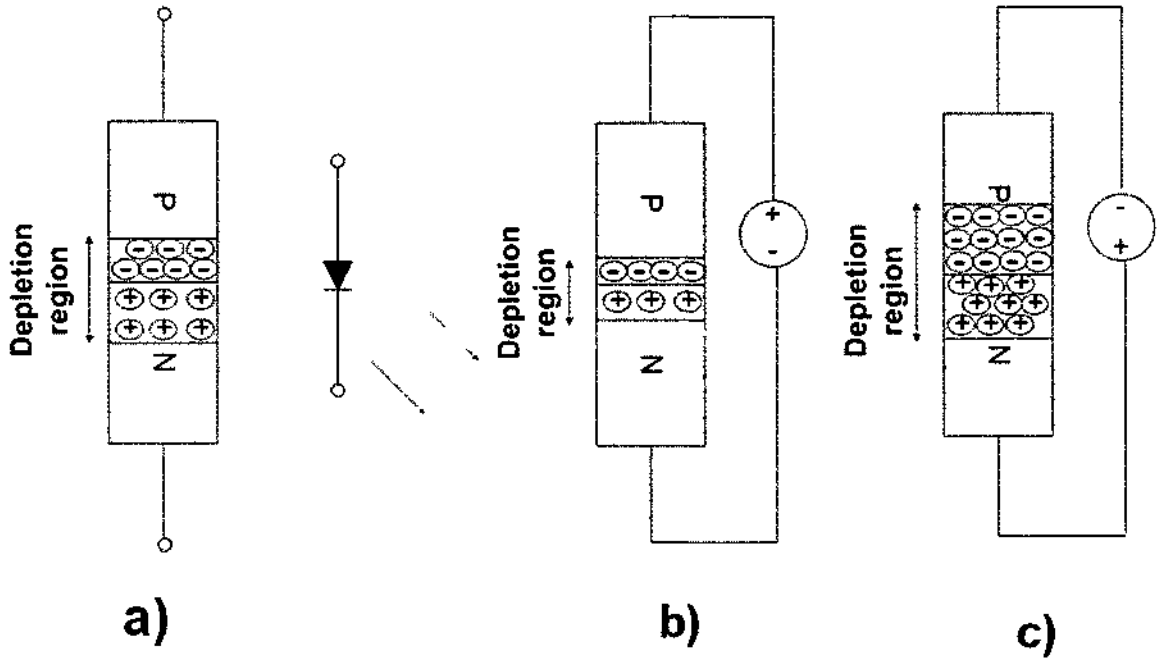

Figure 2. Schematic of a) p-n junction diode and the electrical representation of a photodiode. b) p-n junction under forward bias. c) p-n junction under reverse bias.

The current in a photodiode in the absence of an incident light is similar to a rectifying diode and is called the dark current. The mathematical relationship of the dark current is given as follows

$$I_{dark} = I_s(e^{\frac{qV}{kT}} - 1) \quad (1)$$

where I_{dark} = dark current, V= bias voltage, I_s is the saturation current = current flowing at V=0, q= electron charge, k = Boltzmann's constant and T = temperature in (^oK).

Under optical stimulation, the total current is in terms of the generated photocurrent and is given as follows:

$$I_{total} = I_s(e^{\frac{qV}{kT}} - 1) + I_p \quad (2)$$

where I_p is the generated photocurrent.

The current – voltage (I-V) relationship described above is shown in Figure 3. When the diode is forward biased the current is exponential. In reverse bias mode very little leakage current flows. As the reverse bias increases, a sharp increase in current is observed. The voltage at which the sharp increase occurs is called the breakdown voltage.

The electrical representation of a photodiode is shown in Figure 4. The shunt resistance R_{shunt} is the inverse slope of the I-V curve at V=0. Ideally, R_{shunt} should be infinite. In practice, a very large R_{shunt} is desired. A large R_{shunt} results in lower noise current. The photodiode has a resistance in series, R_{series}. R_{series} rises from the contacts resistance. The series resistance of a photodiode should be as small as possible. The boundaries of the depletion region form a capacitance. The junction capacitance C_j is indirectly proportional to the reverse bias and affects the device response time.

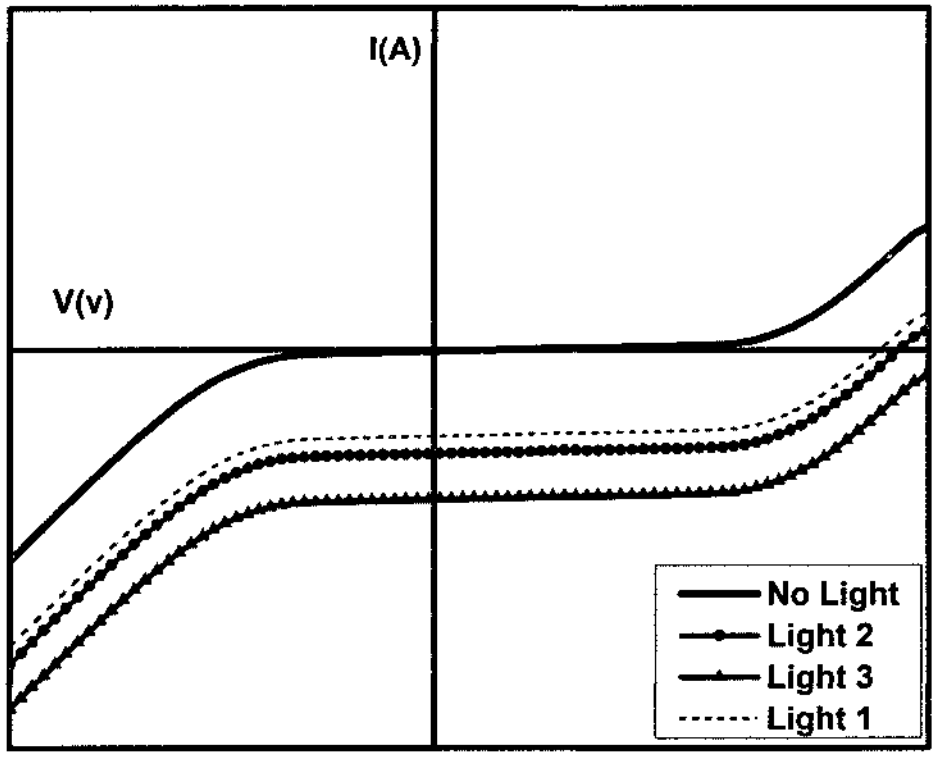

Figure 3. I-V characteristics of a photodiode as a function of illumination. Light 1 – Light 3 represent different incident light intensity. As the intensity increases the shift in the current is more pronounced.

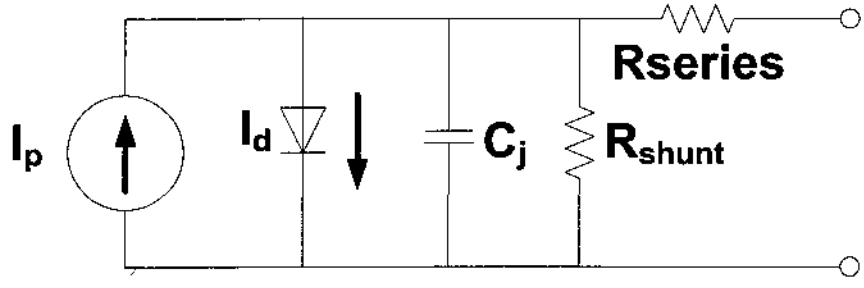

Figure 4. Equivalent electrical representation of a photodiode. I_p = photogenerated current. I_d= diode current. C_j = junction capacitance. R_{shunt} = shunt resistance, R_{series}= series resistance.

Photodiodes have two main modes of operation. The first mode is the photovoltaic mode, and the second one is the photoconductive mode. In the photovoltaic mode, the photodiode is unbiased. While in photoconductive mode, a reverse bias is applied. In photoconductive mode the speed of response is improved; however, the increase in the device speed comes at the expense of noise current. The reverse bias increases the noise current. In photovoltaic mode, the dark current is minimized. The photovoltaic mode is the mode of operation of solar cells.

The responsivity, R, is a measure of the sensitivity of a photodiode. It is defined as the ratio of the photocurrent and the power of the incident light

$$R = \frac{I_p}{P} \quad (A/W) \tag{3}$$

where P is the power of the incident light of a given wavelength. The responsivity varies with wavelength. The percentage of the light that contributes to the photocurrent is called quantum efficiency. It is a measure of the effectiveness of the conversion of light into current. The quantum efficiency (QE) in terms of responsivity is:

$$QE = \frac{Rhc}{\lambda q} \tag{4}$$

where c= speed of light and λ = wavelength of light.

1.4 Metal contacts

The contacts in a photodiode affect its performance, especially the series resistance of the diode. An Ohmic contact is defined as a metal-semiconductor contact

that produces a negligible contact resistance. The I-V characteristic of an Ohmic contact is linear. On the other hand, a Schottky contact of a metal-semiconductor produces a barrier height to the electron flow. The barrier height has to be overcome for current flow. The Schottky contact produces non-linear diode I-V characteristics.[30] The current density of the diode can be written as follows:

$$J = A^{**}T^2 e^{\frac{-q\phi_b}{kT}}\left(e^{\frac{qV}{nkT}} - 1\right) \tag{5}$$

where J = current density, T = temperature, q = electron charge, k= Boltzmann's constant, V = applied voltage, n= diode factor, 1<n<2, and A^{**} = Richardson's constant

$$A^{**} = \frac{4\pi m k^2 q}{h^2} \tag{6}$$

where m = electron effective mass and h = Planck's constant.

The specific contact resistance, ρ_c, of the metal-semiconductor can be written in terms of the current density and voltage.

$$\rho_C = \left(\left.\frac{dJ}{dV}\right|_{V=0}\right)^{-1} \quad (\Omega\text{-}cm^2) \tag{7}$$

Or

$$\rho_C = \frac{k}{qA^{**}T} e^{\frac{q\phi_b}{kT}} \tag{8}$$

1.5 Dissertation Overview

The renewed interest in ZnO is due to its excellent optical and electrical properties and due to novel advanced deposition equipment and technology that hold great promise for technological advancement. Understanding the optical behavior and the root causes of the optical emission is critical to the development of ZnO based

optoelectronic devices. ZnO thin films exhibit a strong UV emission which will benefit UV detectors; however, the difficulty in achieving good homojunction ZnO based photodiodes due to the lack of reproducible p-type ZnO is a challenge. The intrinsic defects are responsible for the electrical and optical behaviors of ZnO. To date, many controversies can be found in the scientific literature about the origin of those intrinsic defects in ZnO. The main objective of this work is to provide an understanding of the native defects and to combine the atomic resolution feature of ALD to deposit, control, characterize the native defects and to optimize ZnO layers for electronic and optoelectronic applications. First, the ALD process of ZnO will be developed. ALD ZnO thin films will be synthesized and the quality of films will be improved. ALD deposition parameters such as temperature, pressure, and surface chemistry will be established and optimized. Then, the native defects responsible for the electrical and optical properties will be investigated to provide a deeper understanding of how to minimize the defects in the ALD ZnO films. High-efficiency ZnO UV photodetectors will be fabricated. The optimization of the diode characteristics will be divided into three main sections:

- Optimization of Schottky and Ohmic contacts to ZnO (Pt, Au, Ni, Al, Ti, W),
- Improvement of ZnO thin film quality and interface,
- Optimization of metal contacts.

To achieve these goals, a variety of different characterization techniques will be used such as spectroscopic ellipsometry, TEM (cross-sectional view and interface study), XRD (crystallinity study), RBS + EDS (ZnO films stoichiometry), XPS (binding energy study, and band energies determinations to accurately study defect levels).

CHAPTER 2

ATOMIC LAYER DEPOSITION (ALD)

2.1 Introduction

Various forms of ZnO such as single crystal, thin films, powder and nanostructures such as nanotubes, nanosheets, needles, nanorods, shells, ribbons and tetrapods can be synthesized. However, most of ZnO growth technique to date studied in technical literature rely on sputtering, pulsed laser deposition, evaporation, vapor liquid phase, metal organic chemical vapor deposition, molecular bean epitaxy. In this work, ZnO is grown using a novel technique offered by ALD to optimize and deposit very uniform thin film for photoelectronics applications such as photodetectors. In this chapter, ALD technique is explored.

2.2 Background

Currently, atomic layer deposition (ALD) is the only deposition technique that can offer thin film uniformity at the atomic resolution at the 32 *nm* technology node and beyond. ALD was developed in Finland by Suntola and colleagues in the late 1970s as atomic layer epitaxy or ALE.[31] ALD is a new version of the old chemical vapor deposition (CVD)-like technique based on alternate saturated surface reactions and provides crucial new techniques for nanotechnology process engineering.[32] One key property of ALD is its self-limiting film growth feature. Each precursor is pulsed into the chamber sequentially, one at a time, and reacts only with the surface until the surface is completely saturated with a monolayer. ALD is a surface reaction driven deposition technique. Unlike other CVD techniques, ALD is capable of depositing thin film on

complex surface morphology with extremely high aspect ratio, excellent conformity and uniformity, and gives the user excellent control over the film thickness with atomic resolution. A variety of materials can be deposited by ALD ranging from semiconductors and metals to insulators. Some of the technologically important materials that can be deposited by ALD are given in Table 2.

Table 2. Period table elements and oxides deposited by ALD

Materials	Chemical Formulas
Metals and elemental semiconductors	W, Pt, Ru, Cu, Mo, Ge, Si, Ni, Ti
Insulators	Al_2O_3, HfO_2, ZrO_2, Ta_2O_5, La_2O_3, SiO_2
Semiconducting metal oxides	ZnO, ZnO:Al, In_2O_3, In_2O_3:X (X= Sn, F, Zr), SnO_2, NiO, WO_3
Nitrides	GaN, AlN, InN, TiN, TaN, NbN, MoN, SiN, WN
II-VI compounds	ZnS, ZnSe, ZnTe, CaS, SrS, BaS
III-V compounds	GaAs, InP, InAs, GaP, AlP, AlAs
Other compounds	$LaCoO_3$, $LaNiO_3$, La_2S_3, PbS, In_2S_3, ZnF_2, CaF_2, $YBa_2Cu_3O_{7-x}$

2.3 ALD Film Growth

Thin film growth in an ALD reactor occurs in a cyclic manner. Each ALD growth cycle is divided into four different process steps. In the first step, the first volatile chemical precursor is pulsed into the chamber and allowed to react with the surface until the surface is saturated. Then in the second step, the ALD chamber is purged by an inert gas such as nitrogen or argon. In this step, the bi-products and any left-over reactants are evacuated to an exhaust system. In the third step, the second chemical precursor is pulsed into the ALD chamber and reacts with the reacted surface from the first chemical

precursor to form the final compound. In the fourth step, the ALD chamber is purged again with an inert gas. A schematic illustrating an ALD cycle is shown in Figure 5. The ALD growth cycles are repeated as many times as necessary to deposit the desired film thickness. Few cycles are usually needed in order to deposit one monolayer of an ALD film depending on the growth rate of the chemical precursor.

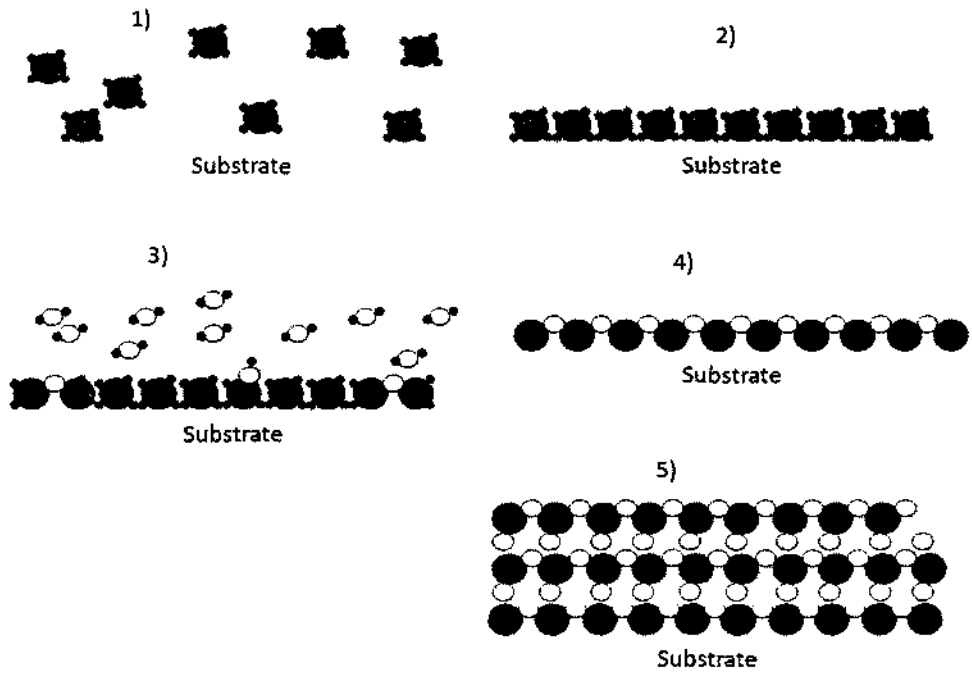

Figure 5. Schematic of an ALD cycle. 1) Pulsing of the first precursor. 2) Purging of the chamber with inert gas. 3) Pulsing of the second precursor. 4) Purging of the chamber with inert gas. 5) Repeat step 1-4 to increase film thickness

Each reaction taking place in an ALD reactor is complete, which implies each precursor reacts with the substrate surface, and the reaction is self terminating as soon as

the surface is saturated. This feature provides ALD its characteristic self-limiting growth nature. Therefore, the chemical precursor dose is irrelevant as long as it is enough to cover and saturate the substrate surface. The deposition rate is independent of the chemical precursor flux and depends only on the number of ALD cycles used. The purge step removes all excess precursor and volatile bi-products. ALD depositions are usually carried out at low temperatures less than 400 ^{o}C. If the deposition temperature is too high, the density of chemically reactive sites is reduced or thermal decomposition of ALD the film and chemical precursors can happen. When the temperature is too low, thermally activated reactions are reduced. Therefore, a careful control of the range of temperatures is required for stable ALD growth. Experimental determination of the ALD process window or ALD temperature window is the most important task in an ALD deposition to ensure the saturation and self-limiting nature of ALD. Establishing an accurate ALD process window ensures proper ALD growth, which means by definition the ideal case of a monolayer per cycle and dependency of the deposition rate only on the number of cycles used. Figure 6 shows schematically the ALD process window as a function of temperature.

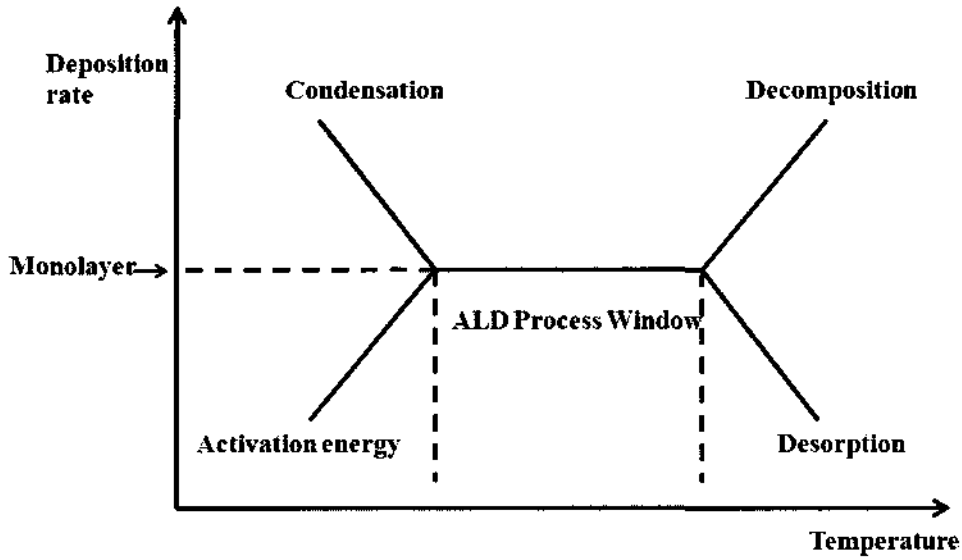

Figure 6. ALD process window as a function of temperature.

2.4 ALD Reactor

Similar to most CVD equipment, ALD depositions can be performed in different types of reactors. The sequential pulsing of the chemical precursors and the need for surface saturation in the reactions require some specific components on all ALD equipment. However, the self-limiting nature of ALD provides a lot more freedom in designing such reactors. All ALD reactors must have the following properties[33]

- Carrier gas supply (usually N_2 or Ar);
- Precursors inlet lines;
- Flow and sequential control of the chemical sources (mass flow controller, high speed valves);
- ALD Reaction chamber;
- Temperature control of the heated precursor and of the reaction chamber;

- Vacuum pump and all related exhaust equipment;.
- High switching speed valves for the delivery of the volatile chemical precursors.

There are many types of ALD reactors that are used in commercial and academic research and development applications.

2.4.1 Viscous Flow Reactor

The flow-type ALD reactors are designed to minimize the purge and pulse time while maximizing the precursor utilization. The reactants are pulsed and delivered to the reaction chamber by a constant flow of the inert gas. Each chemical precursor pulse is separated from the next pulse by a sufficient flow of the inert gas and a sufficiently long purging time. A schematic diagram of an ALD flow reactor is shown in Figure 7.

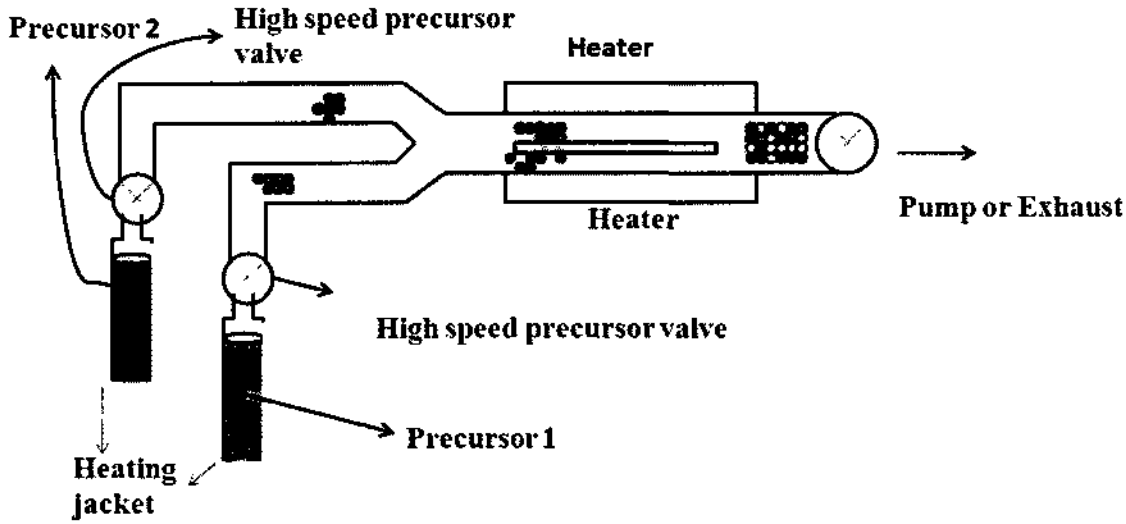

Figure 7. ALD flow type reactor

Some examples of viscous flow type reactors are the cross-flow reactor and the top-flow reactor. In the case of top-flow reactors, the reactants are delivered to the substrates through a shower head configuration or some other kind of mechanism from the top of the reaction chamber.

2.4.2 Molecular flow reactor

Vacuum type reactors or molecular flow type reactors require high vacuum for operation. The deposition rate in a molecular flow reactor is much lower than that of a viscous flow reactor. Due to the high vacuum needed for molecular flow reactors, loadlock chambers are required. Molecular flow reactors allow the implementation of In-situ measurement set-ups such as x-ray photoelectron spectroscopy (XPS) and low energy electron diffraction.

2.5 ALD Precursors

ALD precursor design is an important part of all ALD deposition. A variety of different precursors are used for ALD coatings. The most common types of chemical precursors used are metal halides, metal alkyls, metal alkoxides, metal alkylamides, metal nitrides, metal β-diketonates, and metal cyclopentadienyls. The chemical precursors to be used in an ALD process have to fulfill the following requirements:

- High Volatility;
- Reactivity: very aggressive and complete reactions;
- Thermally stable;
- No self- decomposition;
- No etching of the film;
- Unreactive volatile bi-products;

- Cost effective and environmentally friendly.

2.6 Advantages and Disadvantages of ALD

Each ALD growth cycle deposits exactly the same amount of material making the film thickness only dependant on the number of cycles. This allows the user to accurately control the film thickness. The self-limiting nature of ALD ensures that the chemical precursor flux does not need to be uniform over the substrate as long as it is high enough to saturate the substrate surface. ALD is a CVD-like technique that offers excellent conformity, good uniformity, good film density, good control over the film thickness, high aspect ratio film growth, good repeatability and the capability to deposit multilayer structures in a continuous manner. ALD also offers a wide processing window, which implies uniform films at the same rate can be obtained over a wide range of temperatures as seen in Figure 6. Once the ALD processing window is determined for a specific chemical precursor, uniform film thickness can be deposited with high accuracy and good repeatability.

The one disadvantage of ALD is its relatively slow deposition rate. The average ALD deposition rate per cycle is 0.1 Å to 3 Å.[34] Although ALD is a comparatively slow process. It is useful for deposition where small film thickness is required and where high aspect ratio is needed for complex surfaces. Another limitation of ALD applies for cases when area selective deposition is needed. ALD typically coats substrates uniformly. Table 3 summarizes some important properties of ALD technology compared to other CVD techniques and physical vapor deposition (PVD).[33]

Table 3. A comparison of commonly used deposition techniques.

Material	Thickness uniformity	Step coverage	Sharp interface	Deposition rate
ALD	Good	Good	Good	Poor
MBE	fair	Poor	Good	Fair
CVD	Good	Varies	Fair	Good
PLD	Fair	Poor	Varies	Good
Evaporation	Fair	Poor	Good	Good
Sputtering	Good	Poor	Poor	Good

CHAPTER 3

THIN FILM CHARACTERIZATION TECHNIQUES

3.1 Introduction

This work investigates the novel thin film deposition technology of ALD for ZnO. Very little is known about the ALD synthesis of ZnO thin films. In order to experimentally establish and optimize the crucial ALD process window for ZnO and to measure the ZnO thin film growth rate, spectroscopy ellipsometry has been performed. Since ALD ZnO films are optically transparent, spectroscopic ellipsometry is the best method to accurately measure the ZnO film thickness as a function of ALD growth cycles and deposition temperatures. Spectroscopic ellipsometry determines the optical constants. The ALD ZnO thin films are grown on substrates such as Si, quartz and glass. It is important to investigate the interface of the ZnO films and the underlying substrate because those properties affect the device performance. TEM is one of the best characterization techniques to investigate the cross-sectional properties, grain boundaries and diffraction patterns. A complementary technique to TEM diffraction analysis is XRD. XRD is a non destructive technique that determines the ALD ZnO crystal structure, grain size and orientation. Surface morphology of materials is very important especially in the case of photodiodes. A metal contact is to be deposited on the ALD ZnO for photodetector applications. Therefore, it is indispensable to study the morphology of the as-deposited and treated ALD ZnO samples. One of the best ways to do that is through AFM. A combination of RBS, EDS and XPS determine the film stoichiometry, quality and contamination levels in the ALD ZnO. Combining this information, process

optimization experiments can be designed for ALD ZnO deposition. The intrinsic defect levels and types were characterized by DLTS. The electrical properties were investigated by four point probe, I-V characterization and the Hall Effect. The mechanical properties of bulk are different for a thin film of the same material. For example, bulk single crystal ZnO and polycrystalline ZnO or nanocrystalline ZnO differ in mechanical properties. This affects the device performance in applications such in MEMS. Very little is known about the mechanical properties of ALD ZnO. Nanoindentation was used to accurately calculate modulus and hardness of the ALD ZnO films. These properties are later used for simulation in this work. This chapter explains the theory of ellipsometry measurements, AFM, TEM, XRD, XPS, DLTS, I-V, QE measurements, Hall Effect and four-point probe, PL and Raman spectroscopy, and nanoindentation.

3.2 Structural Characterizations

3.2.1 Ellipsometry Measurements

Spectroscopic ellipsometry is a contactless, non-destructive optical characterization technique used to measure materials' dielectric properties and thickness. Ellipsometers can measure extreme thin film thicknesses as small as the wavelength of the light used for probing, essentially at the atomic level. In this study, spectroscopic ellipsometry was used to measure the thickness of the deposited ALD ZnO thin films. The basic principle of light scattering on a sample surface is shown in Figure 8a. Light with intensity I_i incident to the sample surface at an angle of θ_i hits the sample surface. Part of the light will be reflected at an angle θ_R and intensity I_r. Another part of the light will be transmitted at an angle θ_T and intensity I_T as seen in Figure 8a. The reflection and transmission coefficients can be defined as the ratio of I_r/I_i and I_T/I_i respectively. Using

the basic principles of reflection and transmission of incident lights in Figure 8a, a linearly polarized light with known wavelength λ is sent on the plane of the sample's surface. The linearly polarized light is then converted to an elliptically polarized light. The reflected light is then analyzed by a detector. Information about the film's thickness is then obtained. This principle is shown in Figure 8b. The measurements are expressed in terms of Ψ and Δ.

$$\rho = \tan(\Psi)e^{i\Delta} \tag{9}$$

where ρ = complex reflectance ratio $=R_p / R_s$, R_p and R_s are the Fresnel's reflection coefficients, tan (Ψ) = amplitude upon reflection and Δ is the phase shift.

Spectroscopic ellipsometry measurements are very accurate and highly reproducible. The thickness can be monitored accurately as the reflected light is measured from layer to layer because different materials have different and unique refractive indices. Ellipsometry can be used to measure a single layer thickness and complex structures like in multi-layered specimens.

To measure the ALD ZnO film thickness, a variable angle spectroscopic ellipsometer (VASE) was used. The advantage of VASE over conventional single wavelength ellipsometer is the option of measuring film thickness and optical constant (refractive index) over a wide spectral range and at a different angle of incident. The variable angle feature gives the user the option to measure the film thickness and optical properties at different angles. Each angle provides new data about the material; hence it improves the confidence of measurements. Ellipsometry measurements are performed at angles near the Brewster angle to obtain high sensitivity. The refracted light is linearly polarized. The Brewster angle is dependent on the refractive index of the materials under

study. Because different materials have different refractive indices, different materials exhibit different Brewster conditions. Therefore, a VASE would offer high sensitivity in the measurements which is not possible with a single angle ellipsometer.[35]

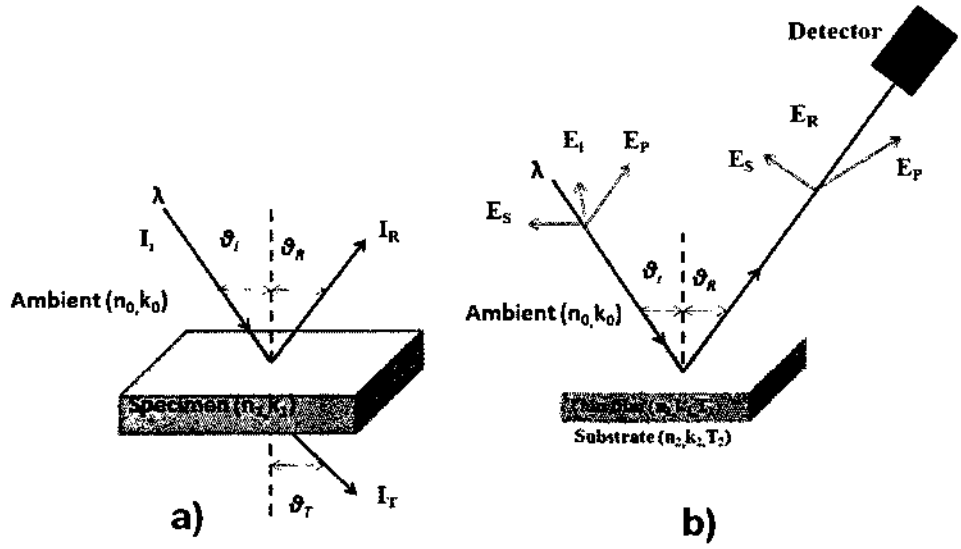

Figure 8. a) Basic principle of light scattering in a material showing the incident light, reflected light and transmitted light. b) Ellipsometry principle showing the thickness measurement of a multi-layered specimen. n and k are the refractive indices. n defines the phase velocity of light and T the thickness. λ is the wavelength of the incident light. The parallel and perpendicular polarization directions are denoted by subscript p and s respectively.

3.2.2 X-Ray Diffraction

X-ray diffraction (XRD) is a non-destructive characterization technique used to identify crystalline phases and their preferred orientation in crystalline solid materials. XRD can also provide information about the crystal lattice constant, the grain size, thin film thickness, defects in the film, strain and stress of thin film. XRD does not required vacuum equipment or sample preparation and it can be used in an ambient environment at room temperature. A typical X-ray diffractometer is shown schematically in Figure 9a. The X-rays are generated by an X-ray vacuum tube where high energy electrons impinge on a solid metal target-the anode. X-ray radiation with energy characteristic of the metal target used is emitted. Some common X-ray targets used in X-ray diffractometer are Cu, Co and Mo. The emitted X-rays are collimated through a set of slits and are sent on the sample under study. Since the wavelength of X-rays is of the order of magnitude of the lattice constant of crystalline solids, XRD can be used to probe the crystal structure of solid matters. When incident X-rays are scattered by atoms of a particular set of crystal lattice planes, this can result in either constructive or destructive interference depending on the incident angle. In a destructive interference the scattered waves cancel each other. In a constructive interference, the scattered waves add together to form a wave with a larger amplitude and intensity. XRD analysis is based on constructive interference, as seen in Figure 9b. The diffracted X-rays are collected by the detector through a set of slits. The crystal lattice information is extracted from the XRD plot using Bragg's Law. The detector is swept through a wide range of angles to record the X-ray intensity as a function of the angle 2θ. X-ray peaks are detected where Bragg's conditions are fulfilled. Bragg's Law is expressed as follow:

$$n\lambda = 2d\sin(\theta) \qquad (10)$$

where n = integer, λ = wavelength of incident X-ray, d = lattice constant, θ = angle between incident X-ray and scattering plane = Bragg's angle.

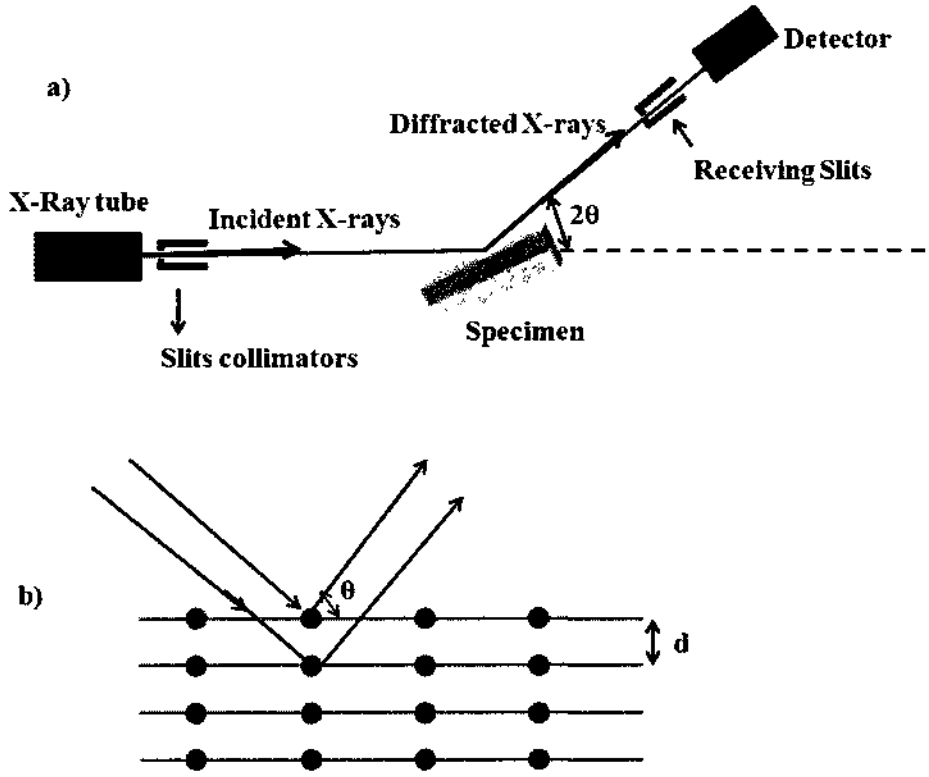

Figure 9. X-ray diffracttion. a) XRD diffractometer. b) Basics principles of XRD showing Bragg's law.

Thin films may be either amorphous, single crystal or polycrystalline which consist of randomly oriented grains. As a result, the diffraction pattern of thin polycrystalline ALD ZnO films will be constituted of a multitude of X-ray peaks from

any crystallites satisfying Bragg's conditions. For thin polycrystalline films, a preferred orientation is defined when a majority of crystallites have the same orientation.

3.2.3 X-ray Photoelectron Spectroscopy

For a deeper understanding of the novel as deposited and the annealing experiments in different ambient gases, the binding energy of the Zn and O elements is necessary. XPS is used to obtain this information. X-ray photoelectron spectroscopy (XPS) is a contactless and non-destructive technique. It is also called electron spectroscopy for chemical analysis (ESCA). XPS is used for composition analysis, valence band structure, elemental analysis, contamination analysis and chemical state. XPS can be used to analyze any element except hydrogen and helium due to their very small atoms. The technique consists of exposing the material to an X-ray beam. The incident X-rays are used to eject electrons from inner shells and measure the kinetic energy of the photoelectrons generated. Core electrons are used for the analysis due to the fact that they carry information about the chemical element. The binding energy is the required energy to free an electron from its atom. The binding energy of a photoelectron is characteristic of each chemical element. Therefore, using the following relation, one can calculate the binding energy and, hence, perform an elemental analysis.

$$K.E = h\nu - B.E \tag{11}$$

where $K.E$ is the kinetic energy, $h\nu$ = energy of the photon used, $B.E$ = electron binding energy.

XPS is surface sensitive. Therefore, an ultra high vacuum chamber is required to help eliminate contamination of the surface. Analysis is usually done on thin layers of a

few nanometers, ~1-10 nm, thickness. The XPS apparatus consists of an X-ray source, photoelectron analyzer, an electron detector, loading chamber, vacuum pumps and related assembly. The most common X-rays used in XPS are Al Kα (1486.6 *eV*), Mg Kα (1253.6 *eV*), Ti Kα (2040 *eV*). A schematic illustrating the principle behind the XPS experimental set-up is shown in Figure 10. Figure 10a shows the XPS apparatus, and Figure 10b shows the basic principle. When a photoelectron is emitted from an X-ray scattering event, it leaves a vacancy hole behind. The vacancy can be filled by an electron of higher energy while releasing energy that can excite and remove another electron called an Auger electron, as seen in Figure 10c. Auger electrons can also be used in XPS for chemical analysis and materials characterization.

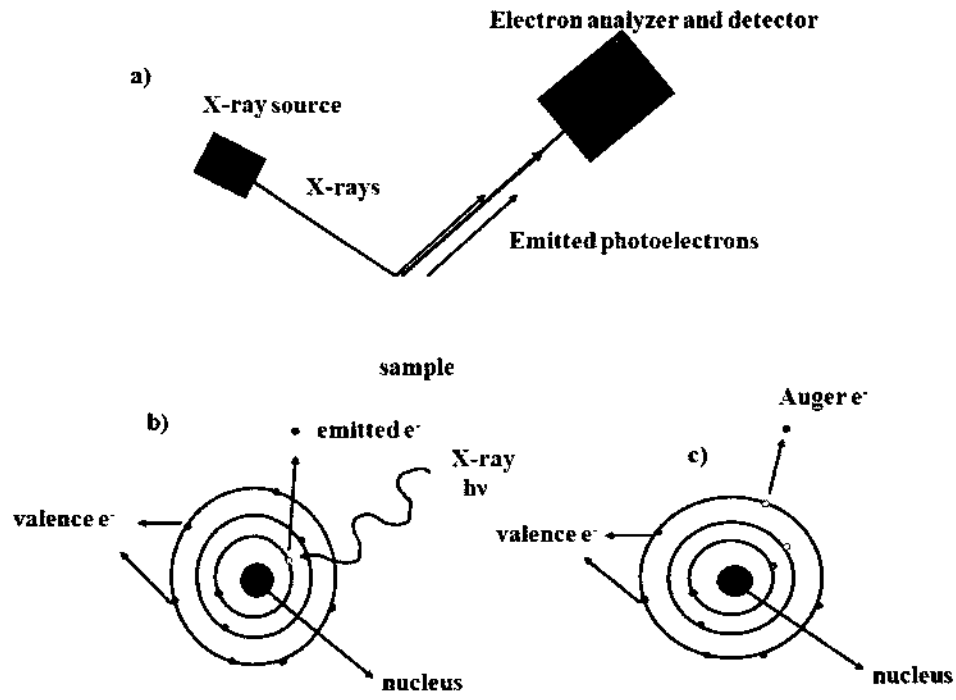

Figure 10. a) XPS apparatus. b) Basic principle. c) Auger electron from XPS

3.2.4 Atomic Force Microscopy

Understanding the surface morphology is critical in electronics and thin film processing at the nanotechnology node. Atomic force microscope (AFM) or scanning force microscope (SFM) is a characterization technique used to study surface topography, roughness, and grain size. Unlike the scanning tunneling microscope, AFM does not require conductive samples; hence, it can be used on any sample including insulators. AFM utilizes a sharp moving tip on the end of a cantilever to scan the sample. As the tip moves across the sample's surface, the deflection from the change in Van der Waals forces, attractive and repulsive forces, between the tip and the sample is measured. An image is then obtained by monitoring the distance with angstroms resolution. The image can be used to obtain information such as surface profile, surface roughness, grain size distribution, surface steps, etc. One of the advantages of AFM is that it can be used in all environments (air, vacuum, liquid).

3.2.5 Transmission Electron Microscopy

As mentioned at the beginning of this chapter, the interface of the films and the substrate affects the device performance. The interface of the as-deposited ALD ZnO and the underlying substrate was investigated by TEM. Transmission electron microscopy (TEM) is a structural characterization technique used to obtain information about the specimen's crystallinity, microstructure, and internal crystal lattice defects such as grain boundaries, twins dislocations and interface. One of the strongest features of TEM structural analysis is the high magnification and its high lateral resolution better than 0.2 *nm*.[36] Inside a TEM, a focused electron beam is incident on a thin film usually less than 200 *nm* to permit the transmission of electrons. As the high energy electron beam (>100

keV), the beam is scattered from crystal atoms of a specific set of crystal planes and unscattered from defects and grain boundaries. The scattered beam is used to obtain the diffraction patterns of the sample under study, while the unscattered beam is used to obtain information about defects such as dislocation in the sample. The diffracted and transmitted beams are delivered to a detector (a fluorescent screen, video camera or a film plate) by a series of lenses located below the specimen. The TEM image is then formed on the image plane. A schematic of a TEM is displayed in Figure 11. The TEM image can be obtained in bright-field or dark-field mode. In bright-field mode, only the direct transmitted beam is used for imaging. In dark-field mode, the diffracted beam is used while excluding the direct beam. TEM analysis is a destructive technique because samples either have to be thinned down considerably so that the electron beam can transmit through the specimen. The high lateral resolution allows the TEM image to provide information about defects within the material and the interface between layers. In diffracted mode, a selected area electron diffraction pattern is obtained. This mode is equivalent to an XRD pattern. The diffraction pattern corresponds to diffused halos for amorphous solids, rings for polycrystalline materials and spots pattern for single crystalline materials. In image mode, one can obtain an accurate measurement of the film thickness and information about grain boundaries and interface features.

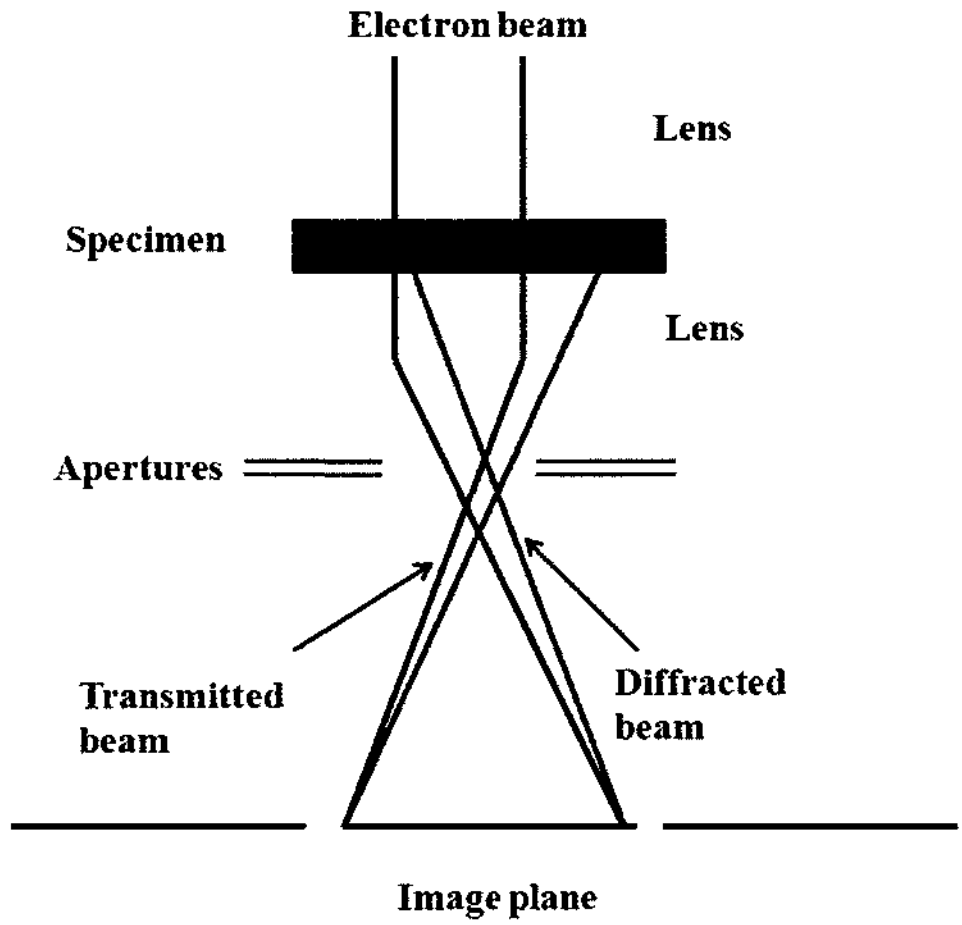

Figure 11. TEM schematic showing the electron optical path of the diffracted and the transmitted electron beam.

3.2.6 Rutherford Backscattering Spectroscopy

ZnO is a II-VI compound. It is necessary to investigate the film stoichiometry in order to verify the 1:1 ratio between Zn and O elements. Rutherford backscattering spectroscopy (RBS) offers the most accurate technique to determine a material's composition experimentally. RBS is a characterization technique capable of providing

film chemical stoichiometry, depth profile, thickness, atomic mass and crystal quality. The principle of RBS is based on the momentum transfer. It consists of colliding high energy ions with atoms in the solid specimen under study. High energy ions (1- 3 *MeV*), typically He, are used to bombard the sample. After the collision, the backscattered beam is collected and analyzed. The low mass He ions undergo elastic collisions with atoms in the ALD ZnO thin film sample. The collision is specific to atoms and varies from atom to atom. When the incident ions collide with light atoms, a significant portion of the energy is transferred, and the backscattered ions have energy significantly lower than the incident beam. In the same manner, the backscattered ions have slightly lower energy than the incident beam after colliding with heavy atoms. Using this property, the atomic mass, the elemental concentration, depth profile, crystal quality and doping impurities in the lattice can be determined. The main weakness of RBS is the difficulty in measuring lighter elements than the ions used. For example, H is difficult to measure using He ions.

3.3 Optical Characterizations

3.3.1 Raman Spectroscopy

Atoms in molecules and crystals are connected by chemical bonds such as ionic and covalent bonds. These systems can vibrate. The vibration frequencies are characteristics of atoms and their bond strengths. Raman spectroscopy is a non-destructive optical characterization technique that studies the vibrational and rotational properties of the molecules and atoms that form the sample material. It is very sensitive to the strength and the length of bonds, and defects can also be detected. In Raman spectroscopy, a monochromatic laser light excites and probes the sample surface. The E-field of the incident light distorts the electron cloud that makes up the chemical bond and

some energy is stored. When the excited electron cloud relaxes, the energy is re-radiated. When the radiation is at the same frequency and energy as the incident beam, the radiation is called elastic Raleigh scattering. Raleigh scattering are usually very strong intensity and are not useful for Raman characterization of materials. Often they are filtered out using filters and apertures. A small portion of the energy is transferred to the sample and excites the vibration modes which are detected by Raman scattering spectroscopy. These scattering are known as Raman scattering. Raman scattering events are inelastic and weak. There are two kinds of Raman scattering: Stokes and anti-Stokes scattering. Stokes scattering occurs when the emitted photons have less energy than the absorbed photons. Stokes scattering is observed on the red side of the spectrum. Anti-Stokes scattering occurs when the emitted photons have higher energy than the absorbed photons. On the spectrum, anti-Stokes scattering is observed on the blue side. An illustration of the principle behind Raman scattering is shown in Figure 12. These Raman shifts can be used to obtain information about the stress and strain in the ALD ZnO. For example, a blue shift in the Raman spectrum corresponds to compressive stress while a red shift corresponds to tensile stress. The amount of the shift is proportional to the strain.

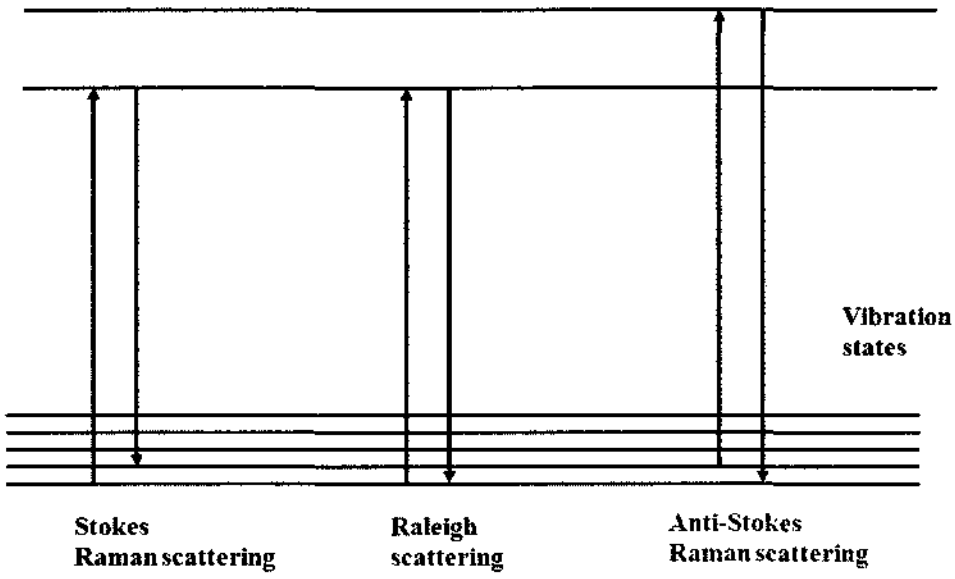

Figure 12. Principle of Raman scattering spectroscopy.

3.3.2 Photoluminescence

Stimulation radiation is due to photon absorption. Emission is the result of an optical excitation usually from a laser source. In photoluminescence spectroscopy (PL), an incident light with energy greater than the bandgap is absorbed by the specimen. The excited electron loses energy through relaxation and falls back down to the ground state energy level. When the radiative relaxation occurs, light is emitted at a specific wavelength and detected by the photodetector. In PL studies, spontaneous emission is achieved through optical excitation. The light involved in PL excitation and emission usually is in the range of 0.6-6 *eV* (roughly 200-2000 *nm*). A schematic of the PL principle is shown in Figure 13. PL measurements are non-destructive and require very little sample preparation. The PL spectrum provides information about the quality of

surface and allows the detection and identification of impurities in semiconductor materials such as ZnO. The radiative emission created from recombination of an electron-hole pair is proportional to the impurity density. Temperature dependence, time dependence and voltage dependence, and photoluminescence are used to further investigate electronic bands to calculate the lifetime, electronic states and trap levels. The highest resolution PL is obtained when very low temperature samples are cooled with liquid He. The main drawback of PL is the sample under study has to emit light which is perfect for direct bandgap semiconductors like ALD ZnO.

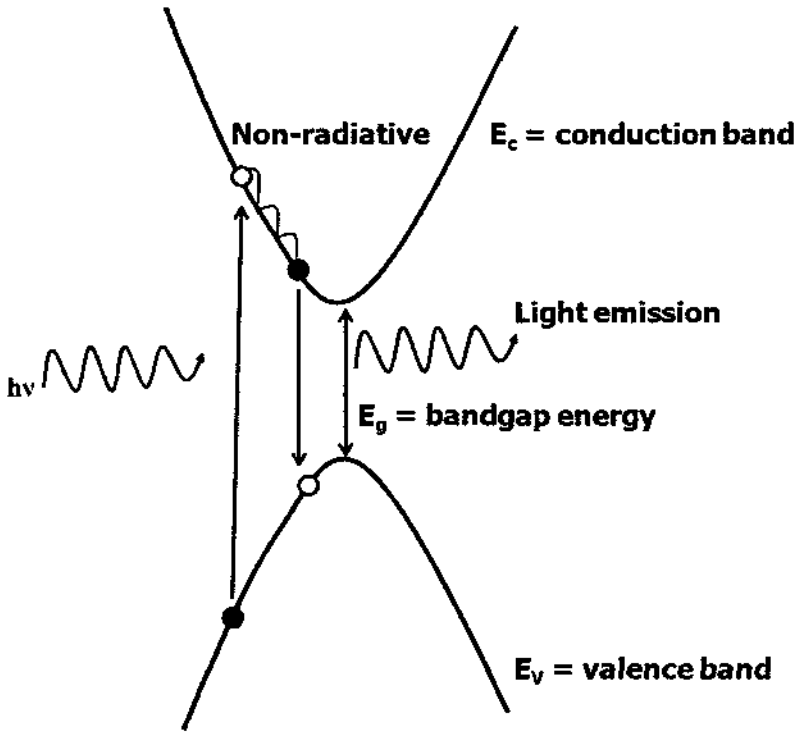

Figure 13. Photoluminescence schematic principle. Emission is achieved through optical excitation.

3.4 Elasto-mechanical Characterization

3.4.1 Introduction

Very little is known about the elasto-mechanical properties of nano-engineered ALD ZnO thin films. Nanoindentation is an excellent technique in investigating the mechanical properties of very thin films, which are difficult to test with conventional mechanical testers. The elasto-mechanical properties such modulus, hardness and poisson ratio of ALD ZnO thin films were accurately determined. These properties were used in the simulation software. A brief background and theory are given in the following section.

3.4.2 Background

Indentation testing is one of the most used material testing methods to determine the mechanical properties of the thin film specimens under study. It consists of touching the specimen under study whose mechanical properties are unknown with another material whose mechanical properties are well known. Diamond is a standard material used to test other materials due to its high hardness value. Nanoindentation, like its name implies, is the indentation testing of materials at the nanometer scale and is the method of choice for extremely thin solid films. Nanoindentation measurements provide information about the hardness, elastic modulus, cracking, phase transformation, creep, strain-hardening, fracture toughness and specimen strength;[37] however, elastic modulus and hardness are the most frequently measured mechanical properties by nanoindentation. Nanoindentation consists of applying known loads on the indenter shaft and measuring the indentation depth through a capacitive sensing or inductive sensing network. This plot

of load versus depth is then used to compute the modulus and hardness of the specimen under test. There are two operating modes for nanoindentation equipment. The first one is a load-control indentation mode, and the second is a depth-control indentation mode. In load-control, the user specifies the maximum load and the load increments. In contrast to load-control indentation, the user specifies the maximum depth of penetration in depth-control indentation mode. Most nanoindentation equipment operate in load-control mode.

3.4.3 Load-Depth curve

As the applied load on the indenter shaft increases, the displacement is recorded and plotted. As mentioned in the previous section, the load-depth curve is used to calculate the elastic modulus and hardness of materials. The nanoindentation tests can be divided into various cycles. A typical cycle consists of the loading phase followed by the unloading phase. The loading phase in a test conducted with a Berkovich tip is governed by elastic-plastic deformation. The unloading phase is purely governed by elastic deformation. The load-depth plot provides information about creep, pop-in events.

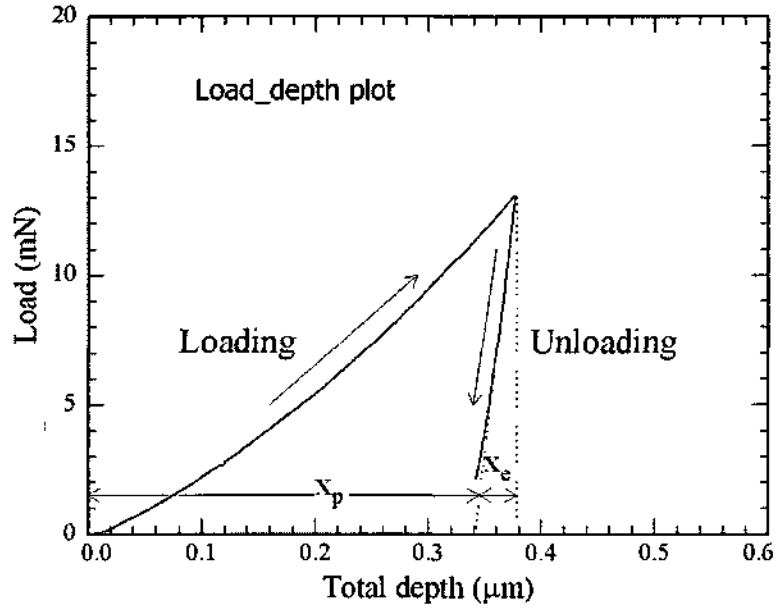

Figure 14. Load-depth curve from a Berkovich indentation test. X_p = plastic region, X_e = elastic region.

3.4.4 Berkovich Indenter

There exist different kinds of indenters which are customized for the specific material under study. The most commonly used indenters in indentation testing are spherical indenters, Vickers indenters, conical indenters, flat punch indenters and Berkovich indenters. Berkovich is the most frequently used indenter made of diamond. It is a three sided pyramidal tip. The tip radius of a typical Berkovich tip ranges from 50-100 *nm* and typically increases with use. After indentation, it gets difficult to accurately measure the contact area with an optical microscope. Therefore, the area is estimated from the exact penetration depth and the known geometry of the indenter. The face angle

of a Berkovich tip is 65.27°. Therefore, the ratio of A by the square of the penetration depth is 24.5.

$$A = 3\sqrt{3}h_p(\tan(\theta))^2 \quad (12)$$

where A= projected area, h_p = plastic penetration depth, θ= face angle.

Substituting the face angle by 65.27 °, we get:

$$A = 24.49h_p^{\ 2} \quad (13)$$

3.4.5 Hardness

Hardness is defined as the resistance to penetration or to permanent deformation due a load or force from a sharp object. The higher the hardness values of materials, the greater the resistance they have to be permanently deformed. In nanoindentation, the hardness or Meyer hardness is defined as the ratio of the full load at maximum depth over the projected contact area. By recording the depth as the load is applied to the indenter shaft, the maximum load can be determined. The contact area can be computed as well.

$$H = \frac{P_{\max}}{A} \quad (14)$$

where H = hardness, $P_{\max}$ = maximum load, A = area.

3.4.6 Modulus

The elastic modulus or Young's modulus is defined as the tendency of a material to deform elastically along the axis the forces are acting on. In nanoindentation, the elastic modulus is defined as the slope of the unloading curve over the square root of the projected area.

$$E_{eff} = \frac{1}{2}\frac{\sqrt{\pi}}{\sqrt{A}}\frac{dP}{dh} \tag{15}$$

where E_{eff} = is the effective modulus, $\frac{dp}{dh}$ = slope of the unloading curve from the load-depth curve, A = contact area.

The relationship described in the above equation can be rewritten in terms of the substrate and indenter properties.

$$E_{eff} = \frac{S}{\sqrt{A}} = \left(\beta\left[\frac{1-\nu_S^2}{E_S} + \frac{1-\nu_i^2}{E_i}\right]^{-1}\right) \tag{16}$$

for a monolithic specimen where β is an indenter dependant constant. For the ALD ZnO thin films, $\beta = 1.22$, ν_s =substrate Poisson's ratio, ν_i = indenter Poisson's ratio, E_s = substrate Young's modulus, E_i = indenter Young's modulus (in this case the Berkovich indenter tip is made of diamond).

The modulus obtained from the load-depth curve is often referred to as the indentation modulus, the elastic modulus, or the Young's modulus.

3.4.7 Factor affecting nanoindentation

Accuracy in the contact area measurement is critical in determining both the elastic modulus and the hardness of thin film materials. Factors that might affect the measurement of the area after the unloading of the tip are sink-in, pile-up, and indentation size effects. The indentation size effect is defined as the increase of the hardness with decreasing indentation size. The presence of friction between the indenter and specimen can lead to the indentation size effect. Another event that can affect nanoindentation tests is the notion of thermal drift. Thermal drift occurs due to thermal expansion of the

apparatus and the change of temperature within the specimen. Another factor that affects significantly the mechanical properties measured by indentation is the surface roughness of the specimen. Smooth samples are desirable. Rough samples give an inaccurate measure of the contact depth which in turn affects the contact area calculation and therefore affects the modulus and the hardness determination.

The principles discussed so far apply to homogenous and isotropic solid specimens. In the case of dissimilar materials such as thin hetero-epitaxial films on top of substrates resulting in multi-layer specimens, a different approach needs to be taken. To avoid the influence on the hardness and modulus measurement due to the substrate effect, a penetration depth of about 10 % of the film thickness is required. For example, for a 400 *nm* ALD ZnO film on Si, indentation depths greater than 40 *nm* will suffer from the substrate Si effect. Simulations like finite element analysis are performed to compensate for the effect of the substrate.

3.4.8 Nanoindentation Experiments

The Nano Indenter® XP in conjunction with a continuous stiffness measurement (CSM) unit made by MTS Nano Instruments was used as the indentation testing instrument. The CSM option adds capabilities not possible with conventional indentation testing methods. By introducing a small and well controlled oscillation into the normal loading sequence of the Nano Indenter®, the CSM allows monitoring of the contact depth and contact stiffness throughout the loading and unloading of the indenter shaft. Unlike conventional indentation testing methods, the use of the CSM provides the advantage of measuring material hardness and elastic-modulus as a continuous function of depth. The load is applied to the indenter shaft through a piezo-driven network. As the load is

increased, the depth of penetration is continuously recorded by a capacitance gauge and sensing network. A diagram of the instrument is shown in Figure 15.

The Nano Indenter® XP with the CSM mode was used in depth control mode meaning the user defined the maximum depth of penetration and the equipment set the necessary loads to reach the desired depth. A three-sided pyramidal Berkovich diamond tip was the indenter tip.

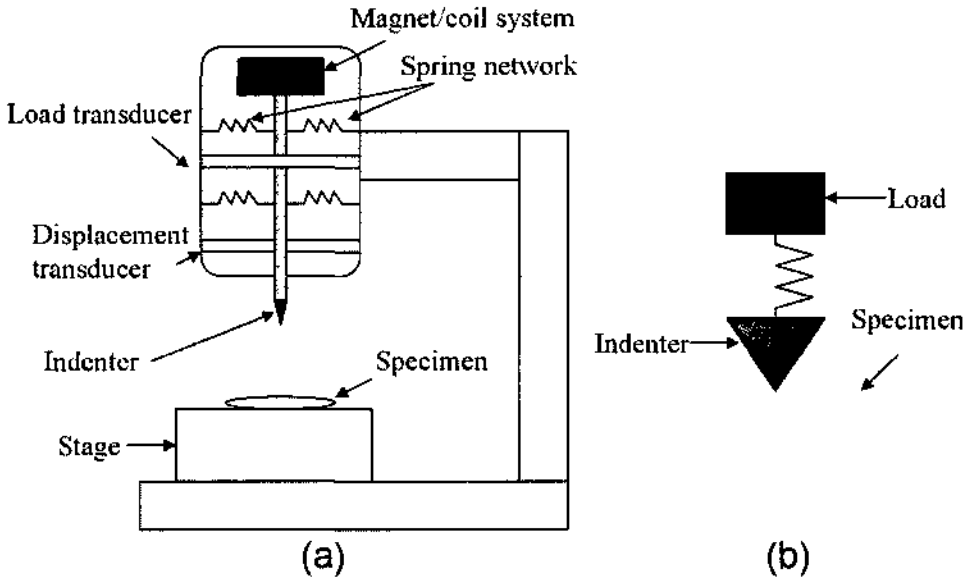

Figure 15. Nanoindentation experimental set-up. a) shows a schematic of a nanoindentation equipment. b) shows the specimen under test.

3.5 ELECTRICAL CHARACTERIZATION

The electrical and optical of ALD ZnO are dominated by intrinsic defects such as vacancies and interstitials forming various trap levels in the films. It is absolutely crucial to study these defect levels in ALD ZnO in order to advance the material of ALD ZnO thin films.

3.5.1 DLTS

Deep-level transient spectroscopy (DLTS) is an electrical technique designed to characterize the energy levels, concentrations and capture rate of electrically active traps in semiconducting materials like ZnO. The DLTS consists of s sensitive capacitance measurement set-up with good transient response. The traps in ZnO identified from the DLTS measurements are represented by either a positive or negative peak depending on the nature of the defects as a function of temperature. One of the key parameters for DLTS is the rate window. The measurement is only sensitive to the rate window, meaning an emission is seen only if a transient with a rate is seen within that window. For the same trap level, by changing the rate window one can change the location of the peak within that rate window. The rate windows are thermally activated.

3.5.2 Hall measurement

For a naturally n-type semiconductor material like ZnO, it is important to measure the carrier density accurately for the fabrication of junction devices in ZnO films. The Hall measurement is a technique used to determine the carrier density, carrier type, mobility and resistivity. A magnetic field perpendicular to the current flow direction in the device under test is applied. A voltage is applied between two contacts on the sample. An E-field is produced perpendicular to the magnetic field and current. The charge carriers in the semiconductor are subject to a force called the Lorentzian force. In steady state, the forces acting on the charge carriers are balanced resulting in a measurable voltage across the sample called Hall's voltage, V_H. This voltage is positive for holes and negative for electrons. The carrier density, type and mobility of the charge carrier are obtained from the Hall coefficient, which is dependent on the Hall's voltage.

3.5.3 Four-Point Probe

The resistivity ρ is a very important property for both metals and semiconductors. It affects electrical properties such as threshold voltage, capacitance, series resistance, charge carrier density and mobility. The resistivity is given by the following relationship:

$$\rho = \frac{1}{q(n\mu_n + p\mu_p)} \tag{17}$$

Four-point probe is an electrical test commonly used to measure the resistivity of the device under test. It consists of four collinear probes arranged with equal probe spacing s. The voltage drop is measured across a pair of probes after a current is applied through the other pair of probes. A schematic of the probe is shown in Figure 16. The resistivity from a four-point probe is given by:

$$\rho = 2\pi.s.F.\frac{V}{I}.t \tag{18}$$

where $s =$ probe spacing, $F =$ correction factor, $V =$ measured voltage, $I =$ applied current and $t =$ sample thickness. The probe spacing is usually 0.5-1.5 *mm*.

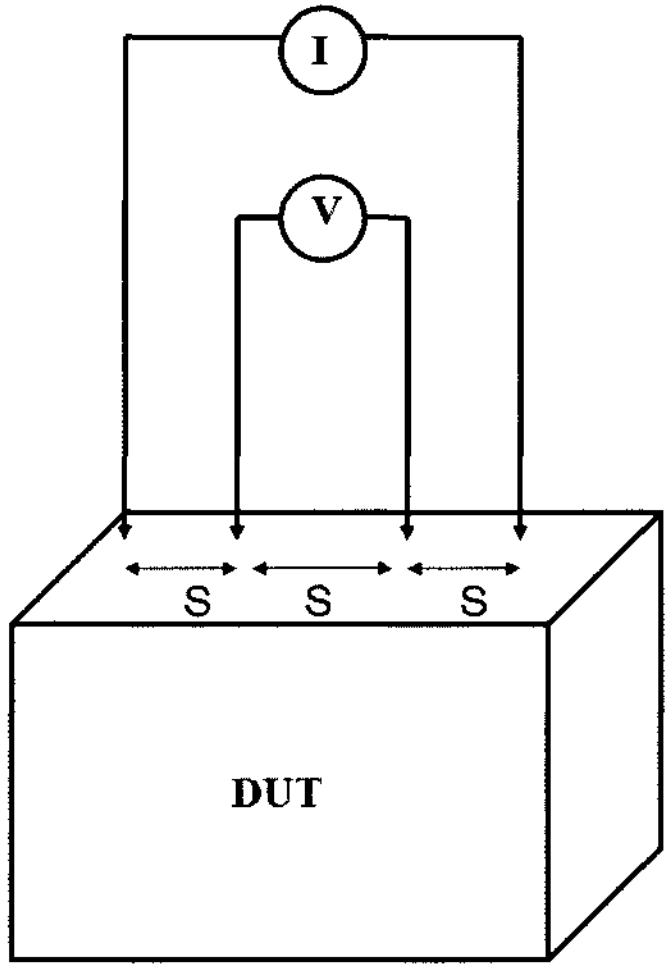

Figure 16. Four-point probe set-up

CHAPTER 4

ATOMIC LAYER DEPOSITION OF SEMICONDUCTOR ZnO

4.1 Introduction

As a wide bandgap direct semiconductor material Zinc oxide (ZnO) exhibits a variety of technologically important properties. It has a thermodynamically stable wurtzite structure. With a large binding energy of 60 *meV* and band energy around 3.39 *eV* at room temperature, ZnO is an ideal candidate for transparent electronics such as transparent thin film transistor (TFT), optoelectronics, piezoelectric, ferroelectric and ferromagnetic applications, solar cells, and sensors.[2,38] Various forms of ZnO such as single crystal, thin films, powders, and nanostructures such as nanotubes, nanosheets, needles, nanorods, shells, ribbons, and tetrapods can be synthesized by many different techniques. These techniques include sputtering,[12] pulsed laser deposition,[13] electrochemical decomposition,[14] thermal evaporation,[15] vapor liquid phase,[16] metal organic chemical vapor deposition, molecular beam epitaxy,[18] and most recently atomic layer deposition (ALD) as a novel thin film deposition technique.[19] Among the thin film growth techniques, Atomic Layer Deposition (ALD) provides unique features such as precise control of ZnO thin films with atomic resolution at the angstrom scale, high uniformity, good conformity and the capability of high aspect ratio. A novel thermal film deposition ALD process for ZnO was developed and optimized for optoelectronic device applications. The resulting ZnO growth structures were investigated using X-ray diffraction (XRD), atomic force microscope (AFM), energy dispersive spectroscopy

(EDS) and Rutherford backscattering (RBS) to gain in depth understanding of the new structural properties and how they relate to device applications.

4.2 ALD ZnO deposition

One of the main objectives of this work was to establish and investigate the novel ALD technique for the synthesis of nano-scaled ZnO films. Towards this end, a Savannah S100 ALD system was used to deposit the ZnO films. Figure 17 shows the schematic of the Savannah S100 ALD chamber. Diethyl zinc (DEZ) was chosen as the chemical precursor for zinc and H_2O vapor was used as the oxygen source. N_2 was used as the carrier gas. Neither of the two chemical precursors was heated for ALD ZnO deposition. The base pressure in the chamber prior to deposition is 9×10^{-2} Torr. The deposition parameters for ALD ZnO, which were determined experimentally to provide a uniform film coverage of ZnO are displayed in Table 4. The deposition pressure was measured to be 2×10^{-1} Torr with a 10 sccm N_2 flow. ZnO ALD films were deposited on p-type Si (100) substrate wafers. The native oxide on the Si wafers was etched prior to deposition by dipping them in 2% of diluted hydrofluoric acid for 4 min followed by a DI water rinse. The samples were dried with N_2. The cleaned silicon wafers were immediately loaded in the ALD deposition chamber and the deposition chamber was pumped to vacuum. To experimentally determine the ALD window, 80 ALD growth cycles were deposited at temperatures ranging from 60 ^oC to 240 ^oC. DEZ and H_2O vapor were pulsed for 0.1 seconds and 0.05 seconds respectively.

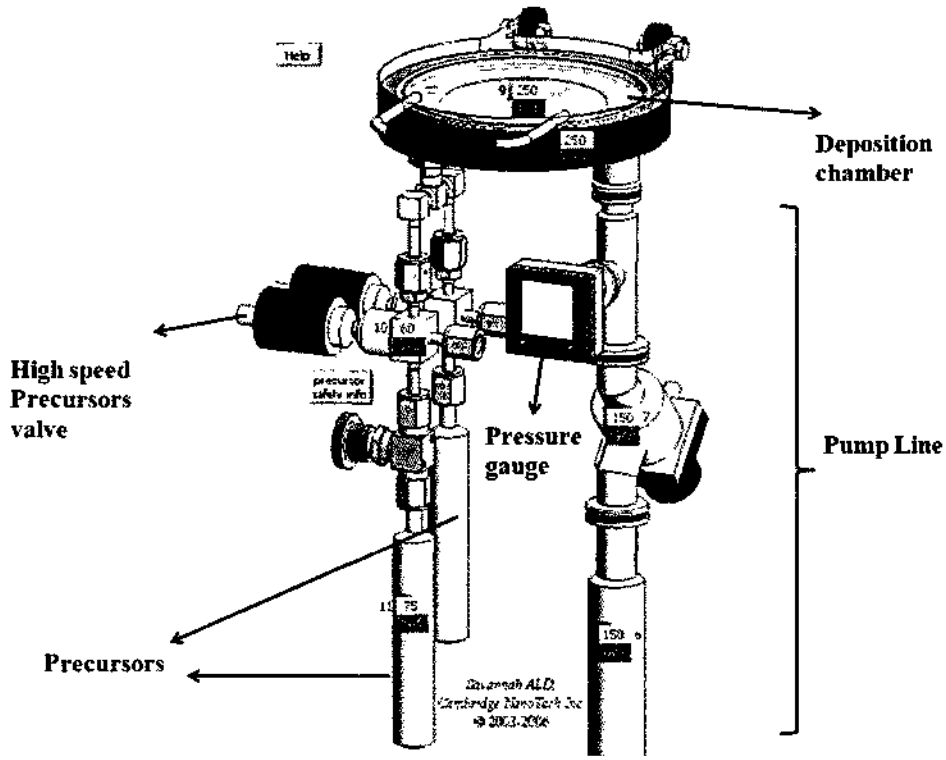

Figure 17. Schematic of Savannah S100 from the labview controlling software by Cambridge NanoTech Inc.

Table 4. ZnO deposition parameters

Valve	Pulse (*s*)	Pump (*s*)	Cycle	Flow (*sccm*)
0	0.05	5	80	10
1	0.1	5		

4.3 ALD process window

After ALD deposition, the ZnO film thickness on each wafer was measured using a variable angle spectroscopic ellipsometer (VASE M44 by J.A Woollam). A Xenon/mercury light was used to probe the surface. The refractive indices of ZnO and Si

are 2 and 3.88 respectively. The Brewster's angle discussed in the ellipsometry section was calculated to be 62.7° for the multilayered sample of ZnO on Si. The measurements were performed at incident angle of 62°, 63° and 75°. The polarizer was set to 30°. The Ψ and Δ values of the complex reflection coefficient were measured to obtain refractive indices which in turn were used to measure the film thickness. The Cauchy dispersion model was used to extract the optical properties. The structure model used to fit the data is shown in Figure 18. For the Cauchy dispersion model the complex refractive index N is defined as:

$$N = n + jk \tag{19}$$

$$n = A_n + \frac{B_n}{\lambda^2} + \frac{C_n}{\lambda^4} \tag{20}$$

$$k = De^{F(\frac{1240}{\lambda} - E_g)} \tag{21}$$

where n and k are defined as the refractive index and the extinction coefficient. λ = wavelength, A,B,C, D, F are fitting parameters.[39]

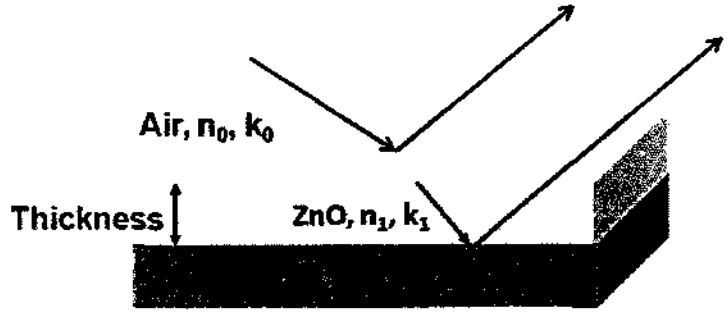

Figure 18. Model for measuring ZnO thickness on Si by ellipsometry.

For the ALD ZnO thin films deposited in this research, the best fitting parameters were determined to be A_n= 1.8701, B_n =0.039346 nm^2 and C_n = 0.0004 nm^4. The extinction coefficient was 0, and the refractive index n goes from 2.1 to 1.9 in the visible region. The thickness was measured on 5 points on the wafer as shown in Figure 19 to investigate the uniformity of the ALD deposited ZnO film.

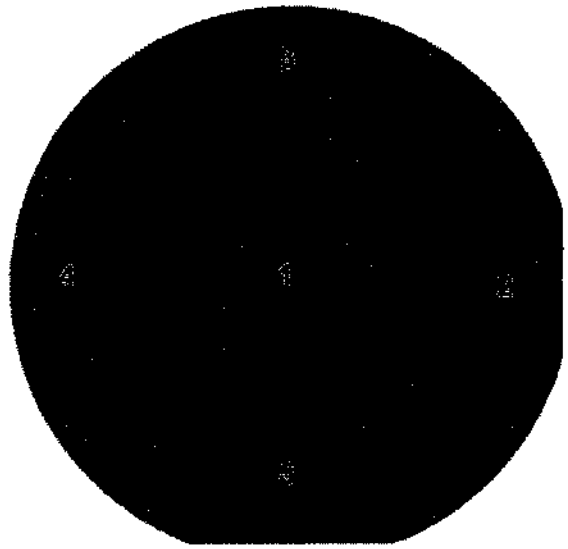

Figure 19. Ellipsometry measurement points

The ALD process window for ZnO was unknown and had to be determined experimentally. The deposition temperatures were randomly generated from 80 ^oC to 240 ^oC to diminish the experimental errors. The thicknesses of different films deposited at different temperatures were measured by spectroscopic ellipsometry and subsequently plotted. The process window is shown in Figure 20. The ALD growth deposition rate

decreases as the temperature is increased beyond the ALD window. This might be due to precursor decomposition. The ALD growth rate increases for deposition temperatures less than the process window due to activation energy requirement. The thermal ALD process window for ZnO was established to lie in the temperature range of 100 ^{o}C – 160 ^{o}C. Within this process window, the deposition is only dependent on the number of ALD growth cycles used as long as the precursor dose is sufficient to saturate the surface. The activation energy, enthalpy and entropy in the ALD process window were calculated from the Arrhenius plot to be -561.639 *J/mol*, -4.078.67 *kJ/mol*, and -59.9566 *J/mol* respectively. The spectroscopic ellipsometry measurements are plotted in Figure 21 as a function of the deposition cycle to determine the ALD deposition rate of ZnO. From Figure 21, one can see the deposition rate of ALD ZnO is linear and the deposition rate was calculated to be about 2 Å per ALD cycle. The root mean squared error on the thickness measurements is 0.3 *nm*. Using Figure 20 and Figure 21, one can customize ALD ZnO for temperature dependent processes and thicknesses using the ALD number of cycle with excellent reproducibility. Optical micrographs of various ALD ZnO films deposited with different thicknesses on 4" Si (100) wafers are shown in Figure 22 .

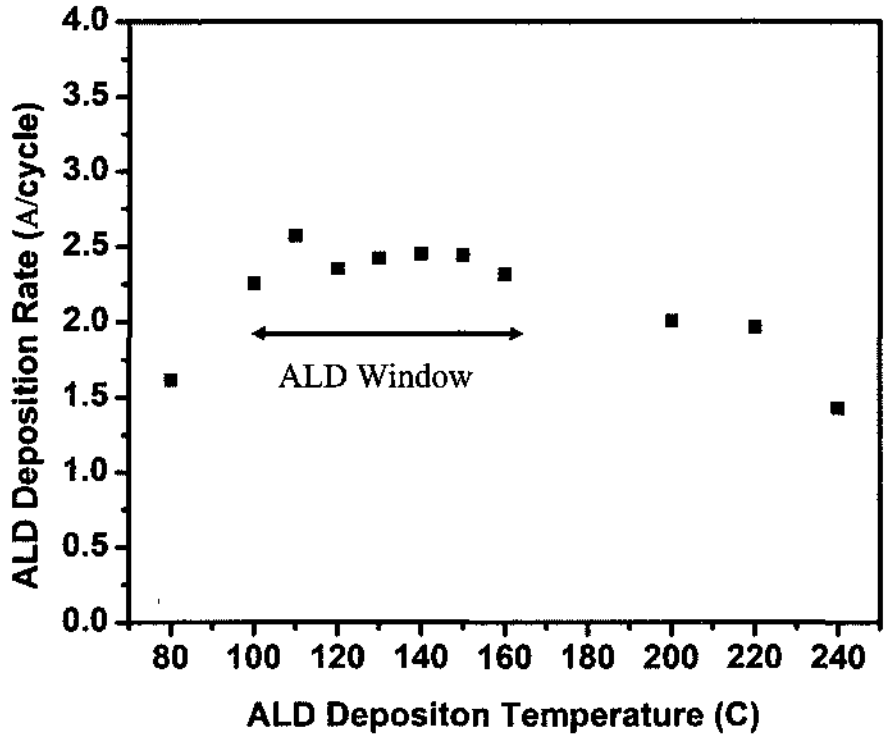

Figure 20. ALD ZnO process window

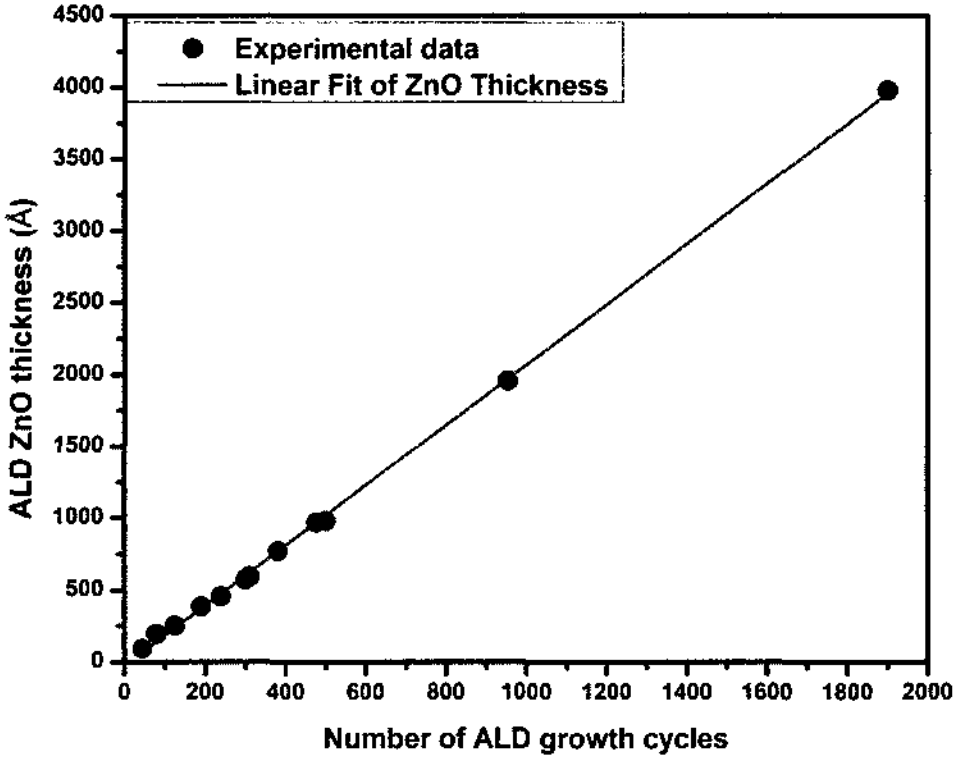

Figure 21. Thickness (Å) vs ALD cycle. ALD deposition rate for ZnO was found to be 2 Å/cycle at 150 ^{o}C.

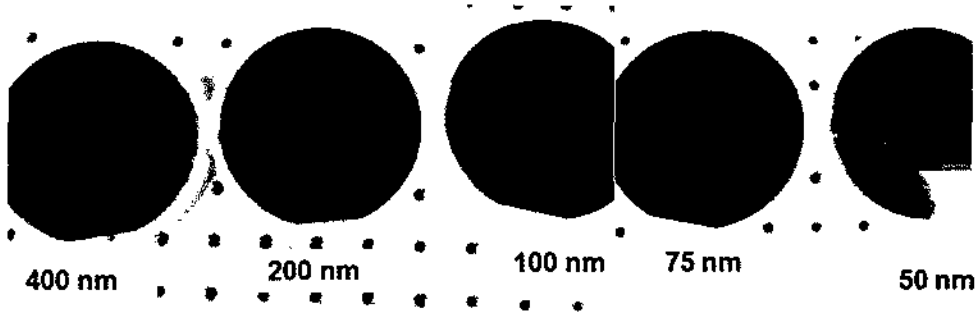

Figure 22. Various ALD ZnO films with different thickness deposited on Si at 150 ^{o}C deposition temperature.

4.4 ALD ZnO Growth and Structural Characterization

In order to optimize the quality and the properties of the as deposited ALD ZnO, the structural, growth mechanism, mechanical, optical and electrical properties need to be understood. The growth mechanism and structural properties of the thin film ALD ZnO was investigated by atomic force microscopy (AFM), X-ray diffraction (XRD), energy dispersive X-ray spectroscopy (EDS), transmission electron microscopy (TEM), X-ray photoelectron spectroscopy (XPS) and Rutherford backscattering (RBS). The fractal dimensions of ALD ZnO thin films at different thicknesses, substrates and temperatures were investigated to provide a figure of merit for the dominant crystal nucleation and growth model.

4.4.1 ALD ZnO Growth Mechanism

Thin film growth can be classified in three main growth modes: the Frank Van der Merwe, the Volmer-Weber, and the Stranski-Krastanov growth models. The Frank Van der Merwe growth model consists of layer-by-layer growth because the atoms of the material are more attracted to the substrate than to themselves. In this manner, incoming atoms are deposited on the substrate forming the film. Epitaxial growth is usually achieved in this growth mode. On the other hand, when atoms of the deposited film are attracted to themselves more than to the substrate, Volmer-Weber growth occurs. This type of growth mode results in island growths. Incoming atoms are drawn to themselves resulting in island formation at the early nucleation stage of film growth. These islands grow larger with increasing deposited atoms and finally coalesce to cover the substrate surface. Stranski-Krastanov is a mixture of layer and island growth. More details on thin

film growth modes can be found in Ref. (40). The ALD ZnO deposition on various substrates has been characterized to fall into one those growth modes. The growth mode was studied by AFM based fractal dimension analysis. One well accepted way of characterizing the surface morphology of thin films is by AFM. The AFM renders it possible to achieve a detailed surface topography with atomic resolution. Using AFM analysis, one can describe thin film surfaces in terms of their fractal dimensions. Fractal geometry has been used to describe thin film growth mechanism.[41,42,43]

The fractal geometry, pioneered by Benoit Mandelbrot, characterizes the scaling structure of a surface by a number D_f, the fractal dimension, that varies from 2 to 3.[41,42,43] A D_f =2 corresponds to a smooth and flat surface. The fractal analysis reveals objects that are similar at all levels of magnification.[44] In this way ALD ZnO thin films growth mode can be obtained at the early growth stage. Using the slit island analysis of Mandelbrot et al., [41] for islands characterized by a fractal dimension D_f, the coastlines obtained by sectioning with a plane are of fractal dimension $D_f' = D_f - 1$. The resulting D_f' varies from 1 to 2. One can obtain the thin film fractal dimension D_f' through the perimeter and the area of the islands using the following relationship:

$$P = \mu A^{\alpha_f} . \tag{22}$$

The above equation can be re-written as follows:

$$\log(P) = \log(\mu) + \alpha_f \log(A) \quad . \tag{23}$$

P = Perimeter of the island, A = area of the island, μ = proportionality factor and $\alpha_f = \frac{D'_f}{2}$.

The plot of the log (perimeter) versus the log (area) should be linear and the slope of the line is α_f; hence, the fractal dimension D'_f can be determined. The fractal dimensions can be used to determine the type of growth model for a particular thin film. Table 5 shows the criteria of different thin film growth models based on the fractal dimension D_f. In this study, the as-deposited ALD ZnO film fractal dimensions are calculated from the WSxM software.[45,46]

Table 5. Growth mode and Fractal dimension by Guisbiers et al.[43]

Growth Mode	Criteria
Volmer-Weber	$D_f' < 1.5$
Stranski-Krastanov	$D_f' \approx 1.5$
Frank-Van Der Merwe	$D_f' > 1.5$

The growth of nano-scaled ALD ZnO films was investigated on different substrates. The ALD ZnO films were deposited on p-type Si (100), quartz and glass wafers. The deposition parameters are the same as discussed in section 4.2. ALD ZnO thin film samples grown at different temperatures on various substrates and at different thicknesses were used for fractal analysis. A typical log (perimeter) versus the log (area) of the ALD ZnO films is shown in Figure 23. As can be seen from Figure 23, the plot is rectilinear. As mentioned above, the fractal dimensions were extracted utilizing the WSxM software. The effect of temperature on the fractal dimensions, hence the surface structures, during the growth of ALD ZnO was investigated using a constant film

thickness which is equivalent to a constant number of cycles at three different deposition temperatures of 100 ^{o}C, 125 ^{o}C, 150 ^{o}C on silicon substrates. The number of ALD growth cycles used was 239 cycles that correspond to a ZnO film thickness of about 50 *nm*. In order to account for any potential effect of substrate material on fractal dimension, the ZnO films were deposited on silicon, quartz and glass substrates.

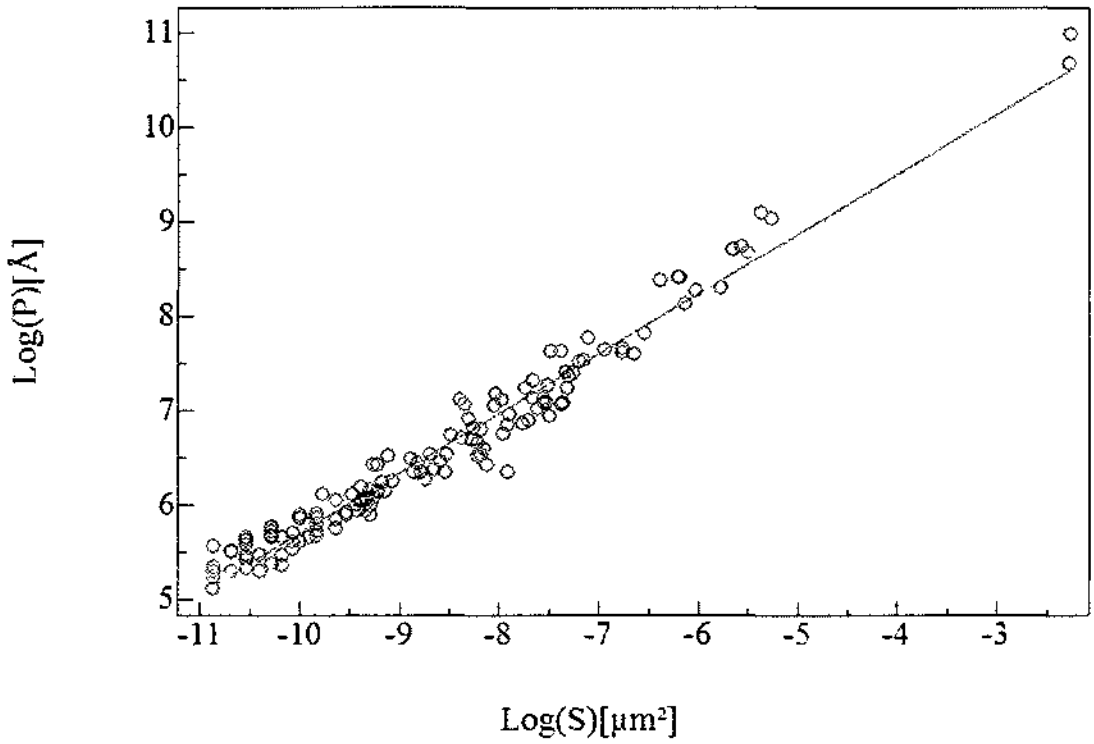

Figure 23. Log of perimeter P versus log of area S of a 310 cycles ALD ZnO deposited at 150 ^{o}C. Fractal dimension $D_f' = 1.314$. The circles represent the experiment data.

During the course of this experiment, all the deposition parameters were maintained constant; only the substrate material was changed. The resulting fractal dimension D_f' is shown in Table 6 as a function of the deposition temperature and in Table 7 showing the dependence on substrate influence. From Table 6, it is evident that the ALD ZnO deposition at 100 ^oC offers the smallest D_f'. As the ALD temperature is increased from 125 ^oC to 150 ^oC, no significant change is observed; however, as seen from the extracted D_f' values in Table 7, there is no significant effect of the substrate material on the fractal dimension D_f'. Figure 24 displays the fractal dimension versus the number of ALD deposition cycles. D_f' is ~1.3 with increasing ALD ZnO thickness. From the growth mode criteria in Table 5 established by Guisbiers et al.,[43] the as-deposited ALD ZnO film is of Volmer-Weber type growth. This thin film growth mode is consistent with temperature variation and with different substrate materials. A schematic model of the Volmer-Weber growth is shown in Figure 25 with distinct island growth features at the earliest nucleation stage. This is collaborated by the ellipsometry thickness measurement in Figure 21 showing a different deposition rate for very shallow films (ALD growth cycles less than 50 cycles). The slightly higher deposition rate indicates a nucleation stage. As thicker films are grown the deposition rate remains constant at 2 Å/ALD growth cycles.

Table 6. ALD growth temperature and fractal dimension D_f'. 239 ALD cycles were deposited on Si for all ZnO depositions.

Temperature(^oC)	Fractal Dimension (D_f')
100	1.263
125	1.353
150	1.307

Table 7. Substrate effect on fractal dimension D_f'. 1900 ALD cycles were deposited at 150 ^oC for all deposition ZnO depositions.

Substrate	Fractal Dimension (D_f')
Silicon	1.263
Quartz	1.221
Glass	1.268

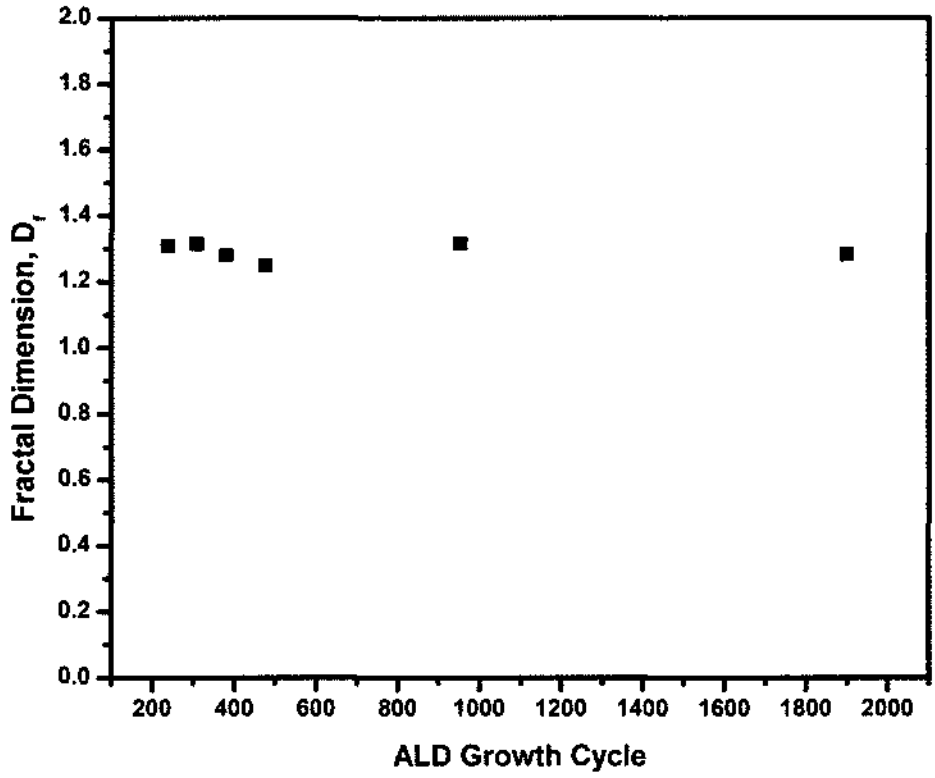

Figure 24. Fractal dimension versus ALD growth cycle. The films were deposited at 150 ^{o}C on Si.

Figure 25. Volmer-Weber growth model for ALD ZnO.

4.4.2 ALD ZnO Structural Characterization

Knowing the growth mode of the ALD ZnO films, it is necessary to understand the structural properties of the deposited films in order to further improve the quality of the ZnO films. Film contamination and defects in the film will further reduce the device performance of the ALD ZnO films for optoelectronic applications such photodetectors. The morphology will be studied by AFM and the cross-section analysis will be done by TEM. Energy dispersive X-ray spectroscopy (EDS) and Rutherford Backscattering (RBS) analysis were performed on the as-deposited ALD ZnO films in order to characterize the contamination level and the film stoichiometry. EDS analysis was performed using an SEM (JSM-6060LV) by JEOL. Figure 26 shows the EDS analysis results of ALD ZnO films deposited on Si. The elemental EDS analysis revealed the presence of only the expected Zn, O, and Si elements with no other detectable contaminants. The RBS study revealed a Zn to O ratio of 1:1. The error on the Zn measurements was ±0.1 and that of O was ±0.02. The combination of both the EDS study and the RBS analysis assured very good quality contamination free and stoichiometric ALD ZnO thin films.

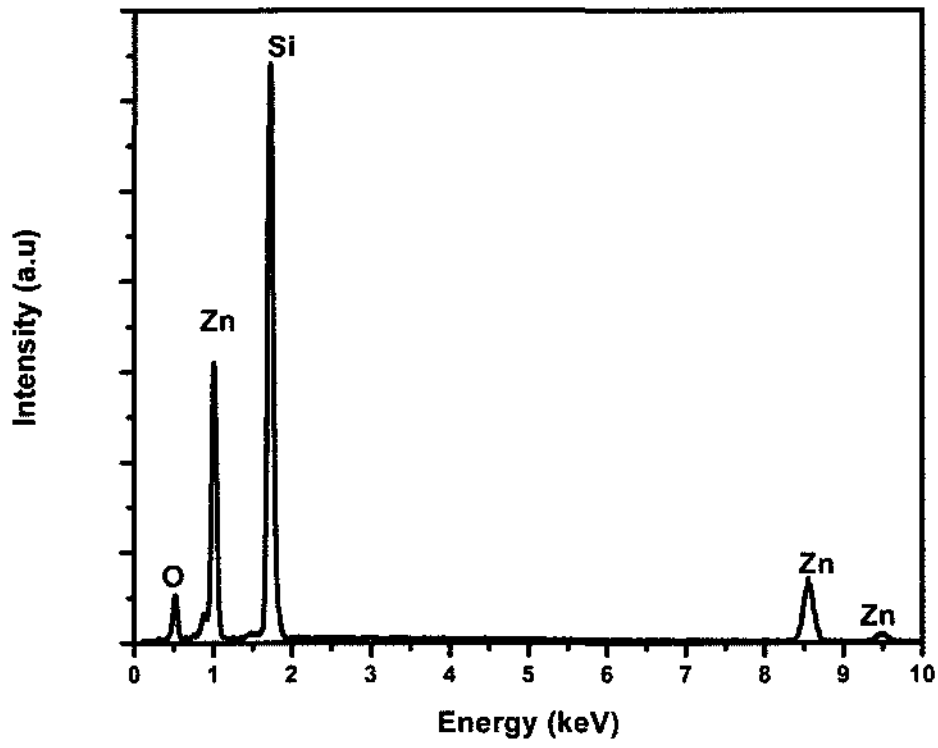

Figure 26. Energy dispersive X-ray spectroscopy (EDS) spectrum. The EDS analysis on ALD ZnO samples revealed the presence of only Zn, O, Si elements.

The ZnO films surface morphology was investigated by a Nanoscope Dimension™ 3100 AFM by Veeco. The AFM analysis of the surface roughness revealed an increase in roughness as a function of the ZnO film thickness. The RMS roughness value of the films increases from ~ 1 *nm* for the thinnest ALD ZnO film (250 ALD cycles which is equivalent to film thickness of 50 *nm*) to ~ 7 *nm* (1900 ALD cycles which is equivalent to film thickness of 400 *nm*) for the thickest ALD ZnO film investigated for this study. Figure 27 shows the plot of the RMS of the as-deposited ALD ZnO samples and an AFM image of a 954 ALD cycles or 200 *nm* thick ALD ZnO thin films.

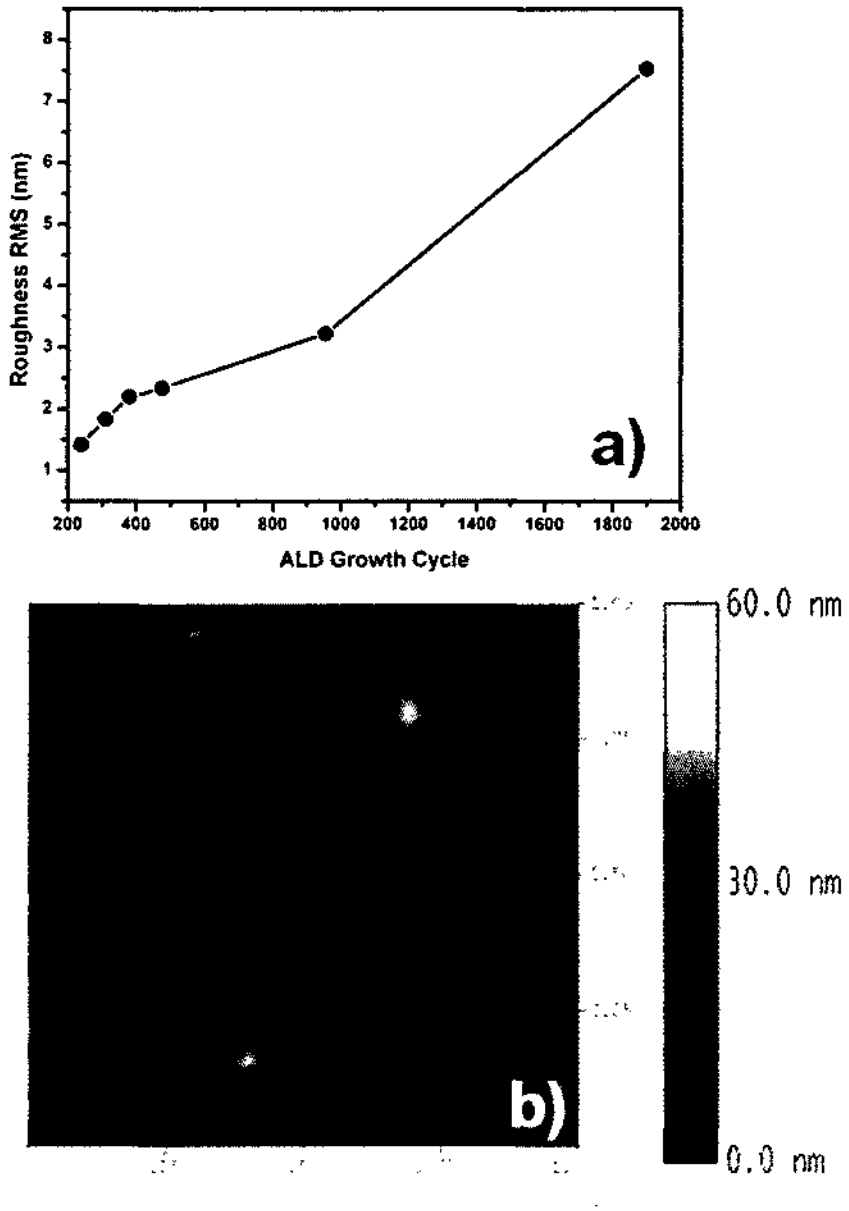

Figure 27. a) AFM measurement of ALD ZnO film roughness vs deposition cycles. b) AFM image of a 954 ALD cycles of ZnO on Si.

The film crystallinity was investigated by a Rigaku Miniflex X-ray diffractometer (XRD) with Cu K_α radiation (λ=1.54 Å). The goniometer diameter was 150 *mm*. The

sensitivity on the 2θ measurements is 0.05°. The XRD plot of the as-deposited samples is displayed in Figure 28a. As the ZnO film thickness is increased, a stronger peak of (002) is observed. The ALD ZnO films exhibit a preferential growth in the (002) plane or c-plane of the hexagonal wurtzite phase of ZnO. The wurtzite structures have a hexagonal unit cell with two lattice parameters c and a with the ratio c/a=$\sqrt{\frac{8}{3}}$. The lattice parameters of the as grown ALD ZnO were calculated using the following relationship:

$$\frac{1}{d^2_{(hkl)}} = [\frac{4}{3}(h^2 + k^2 + hk) + l^2(\frac{a}{c})^2]\frac{1}{a^2} \qquad (24)$$

where h,k and l are the miller indices; d is obtained from Bragg's law.

For the (002) direction, the following lattice parameters were calculated and tabulated in Table 8. From Table 8, it can be seen that the percentage difference to bulk ZnO is reduced as a function of both temperature and growth cycle. As a function of deposition temperature, the lattice constants of ALD ZnO films converge towards those of the bulk ZnO. Similarly, as a function of increasing thickness the lattice constants converge towards the bulk values with the closest ones obtained from the 400 *nm* thick ZnO film.

Table 8. Lattice parameters of the ALD ZnO as a function of ALD growth cycle and temperature.

ALD Growth Cycle	c (Å)	a(Å)	c % from bulk	a % from bulk
239 at 100 °C	5.3458	3.273621	2.803846	2.300643
239 at 125 °C	5.355	3.279254	2.980769	2.4767
239 at 150 °C	5.1616	3.160822	0.738462	1.22433
310 at 150 °C	5.169	3.165353	0.596154	1.08271
381 at 150 °C	5.1614	3.160699	0.742308	1.22815
477 at 150 °C	5.1554	3.157025	0.857692	1.34297
954 at 150 °C	5.1862	3.175886	0.265385	0.75356
1900 at 150 °C	5.2012	3.185072	0.023077	0.46652

The presence of small grains and crystallites in the films for very low ALD cycles is predicted by the Volmer-Weber island nucleation model and explains the increase of roughness from the AFM measurements with increasing film thickness. Once a nucleation site island has formed, subsequent ALD cycles contribute to the growth of the crystallites into larger grains. Each grain can have a different crystallographic orientation and each crystal orientation grows at a different rate; hence, this contributes to the increase of ZnO film surface roughness. As the film thickness increases from 239 cycles to 1900 cycles, the intensity of the (002) peak also increases, as seen in Figure 28b.

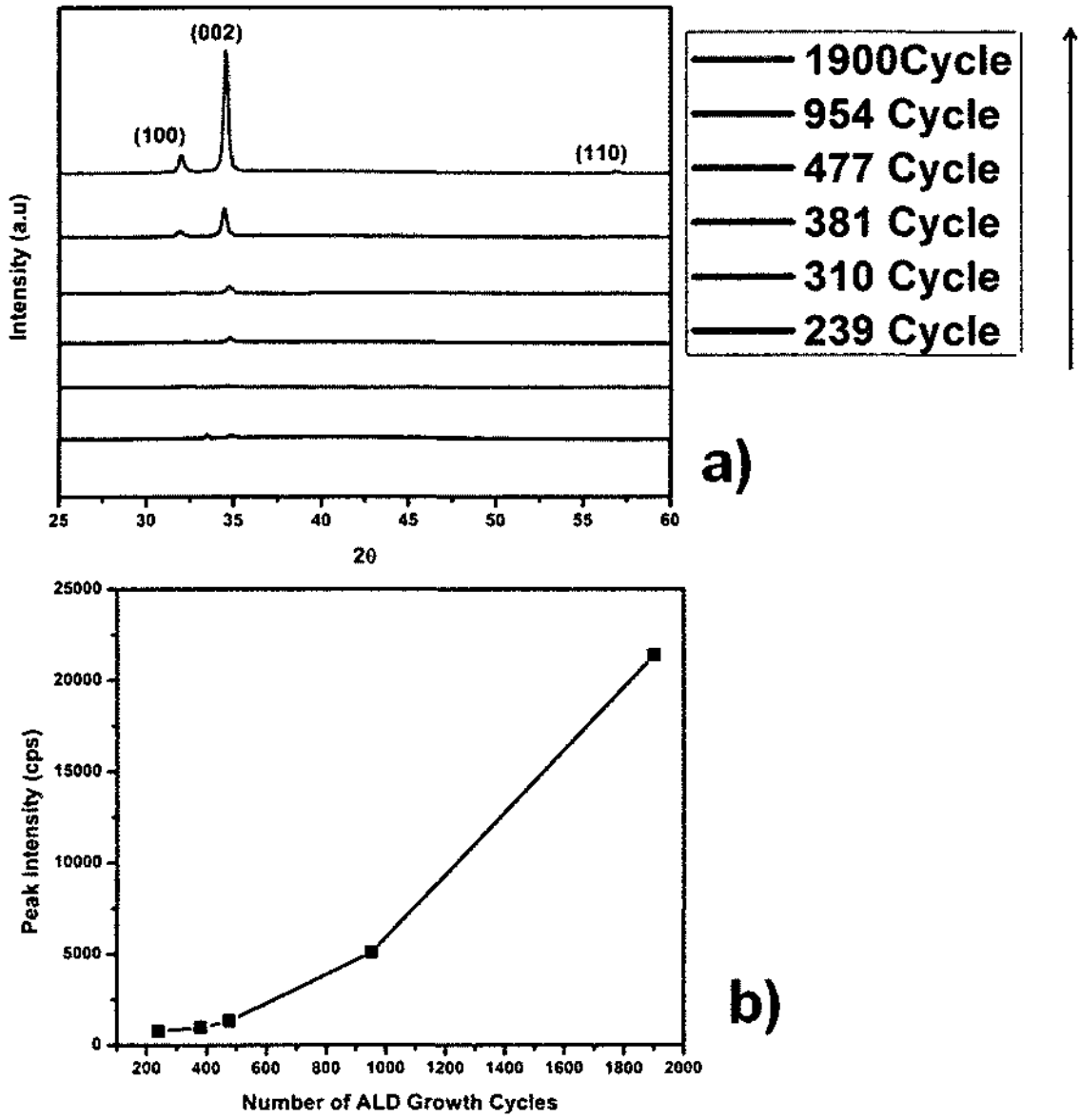

Figure 28. a) XRD pattern of as-deposited ALD ZnO films as a function of film thickness. The as-deposited samples grow along the (002) plane. b) (002) peak intensity as a function of the film thickness. The patterns were recorded using CuK_{α} radiation (λ=1.54 Å).

This result provides experimental evidence that ALD ZnO is deposited as polycrystalline material independent of the number of ALD growth cycles in accordance with the Volmer-Weber island growth model. The full width at half maximum (FWHM) and the peak position of the (002) plane were plotted in Figure 29. The (002) peak position shift is shown in Figure 29a. From Figure 29a, a shift in the (002) peak position from the bulk ZnO value can be observed. This shift is higher for the thinnest film, which is attributed to a built-in stress in the as-deposited ZnO film and further evidence of Volmer-Weber crystallization because impinging growing crystallite islands will ultimately generate strain. The peak position converges quickly after the initial nucleation phase for the thicker films. This result corroborates the data obtained in Table 8. The peak identification was carried out using the JCPDS PDF# 98-000-0111 reference file for powder ZnO. The ALD ZnO film crystallinity is improved with increasing film thickness. This is confirmed as the FWHM gets smaller for thicker films and the intensity of (002) plane gets stronger. This can be seen in Figure 29b.

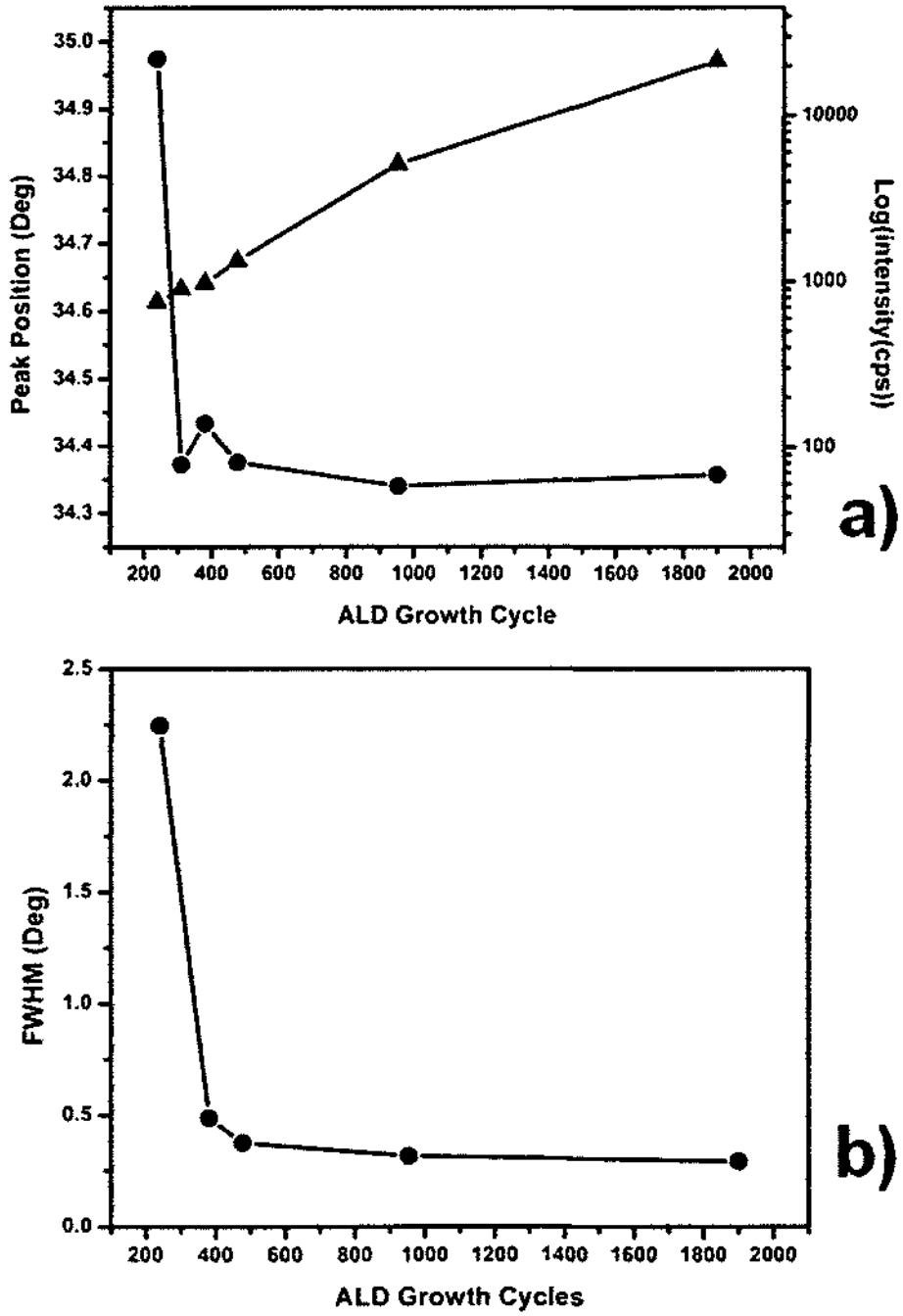

Figure 29. a) Plot of the peak position in the (002) plane vs. number of ALD deposition cycle (circle) and log of the peak intensity (up triangle). b) Full-width at half maximum vs. deposition cycle at the (002) XRD peak of the as-deposited samples.

Detailed cross-sectional transmission electron microscopy (TEM) analysis was performed on ALD ZnO films in order to investigate the nanostructure of the films. The cross-sectional analysis was performed by a JEOL JEM2100F HRTEM. The TEM cross-sectional micrograph of a 50 *nm* ALD ZnO film on Si is shown in Figure 30. It can be seen that the film is very uniform in Figure 30a. In this case, the native oxide on the Si was not removed before the ALD ZnO deposition as seen in Figure 30b. High resolution TEM cross-sectional analysis confirmed the XRD measurements revealing the polycrystalline nature of the ALD ZnO films corroborating the Volmer-Weber growth model. It can be seen that no columnar grains are present in the film. Instead, we find randomly oriented grains demonstrating that the films deposited by ALD are polycrystalline ZnO films as seen in Figure 31.

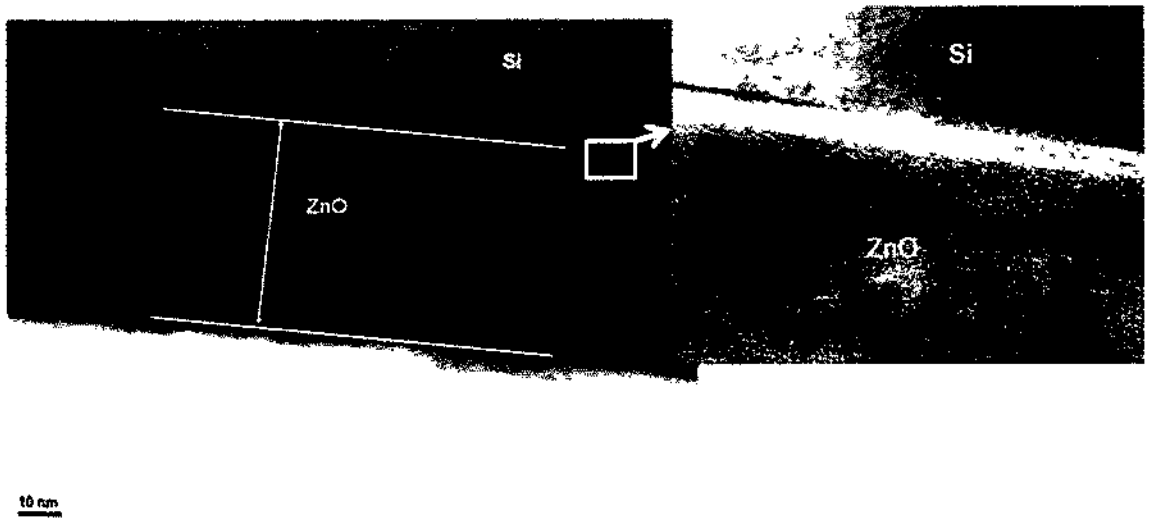

Figure 30. TEM micrograph of 50 nm ZnO films deposited at 160 °C. In the inset a high magnification of the interface of ZnO and Si. A thin layer of native oxide is also observed.

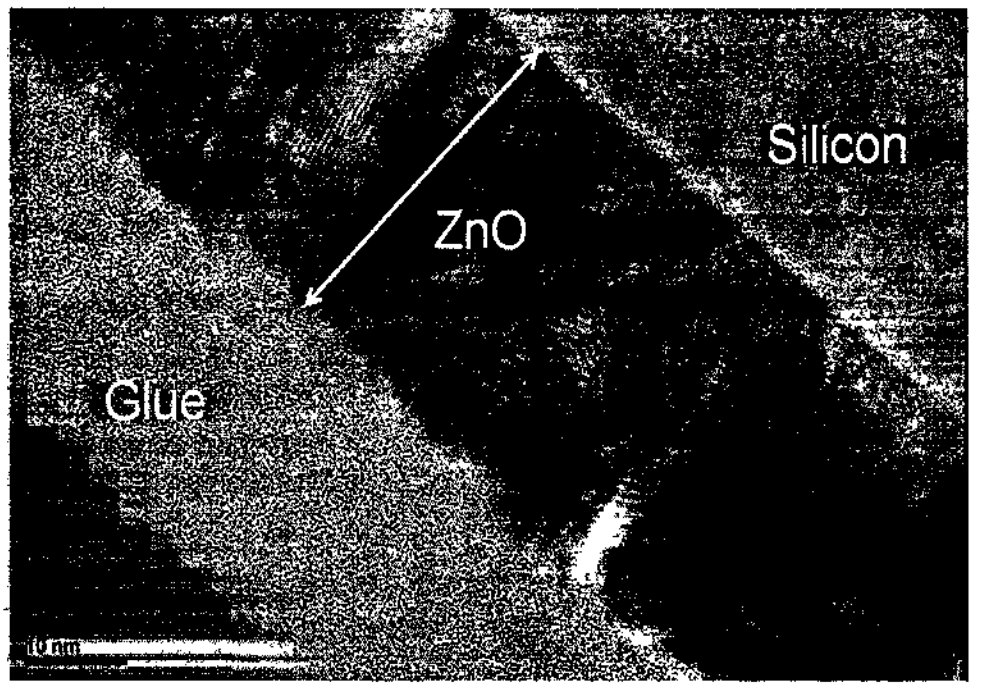

Figure 31. HRTEM micrograph of 30 *nm* of ALD ZnO. Randomly oriented grains can be seen.

4.4.3 Effect of Rapid Thermal Annealing on ALD ZnO

A portion of a 400 nm thick ALD ZnO on Si sample was subdivided into smaller pieces by cleaving and annealed in oxygen, nitrogen and room ambient. The annealing was performed in a rapid thermal annealing (RTA) Solaris 150 furnace by Surface Science Integration. The annealing temperatures were varied from 400 ^{o}C to 600 ^{o}C with 50 ^{o}C increment for 1 h time. A plot of the RTA experiment for a ZnO sample annealed at 400 ^{o}C for 1h is displaying the furnace recipe in Figure 32. The chamber was filled with N_2 for the N_2 annealed samples and O_2 for the O_2 annealed samples. In the case of

room ambient annealing, no gas was used. The annealing chamber was directly connected to the room air. The samples were cooled down in the chamber before opening the RTA chamber.

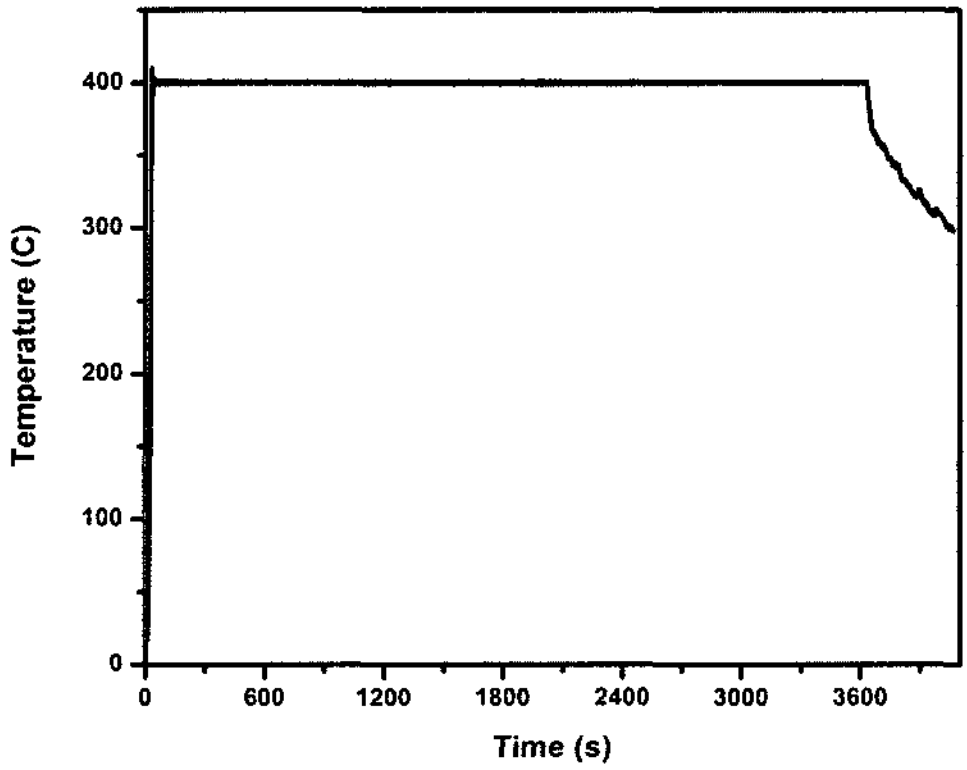

Figure 32. Actual RTA experiment at 400 ^{o}C for 1h for a 400 *nm* thick ALD ZnO film.

After annealing, the crystal structure of the ZnO films was again investigated by XRD. No new crystallographic phases were observed after annealing as compared to the as-deposited non-annealed ZnO samples. This observation was consistent with the annealing environment and the annealing time; however, the intensity of the (002) peak

increased significantly with increasing annealing temperature compared to the as-deposited samples. The same trend was observed in oxygen, nitrogen and room ambient annealing. Figure 33 shows an XRD plot of ALD ZnO samples annealed at various temperatures in N_2 and the FWHM plot as a function of different annealing atmospheres. The individual grain size of the ZnO thin film grew with temperature and this effect is independent of the annealing ambient gas as seen in the AFM surface morphology analysis; see Figure 34.

The grain size of the ZnO thin film grew with temperature as documented in Figure 34. Using Scherrer's formula, the grain size of the ALD ZnO thin films was estimated. [47] Table 9 summarizes the resulting grain size following the different thermal annealing experiments. The data in Table 9 provide a rough figure of merit to investigate the grain growth as a function of annealing temperature.

$$D = \frac{k\lambda}{B\cos\theta} \tag{25}$$

where D is the Crystallite size, k is the Scherrer's constant, $k = 0.9$, λ is the X-ray wavelength, B is the full width at half maximum in radian and θ is the diffraction angle.

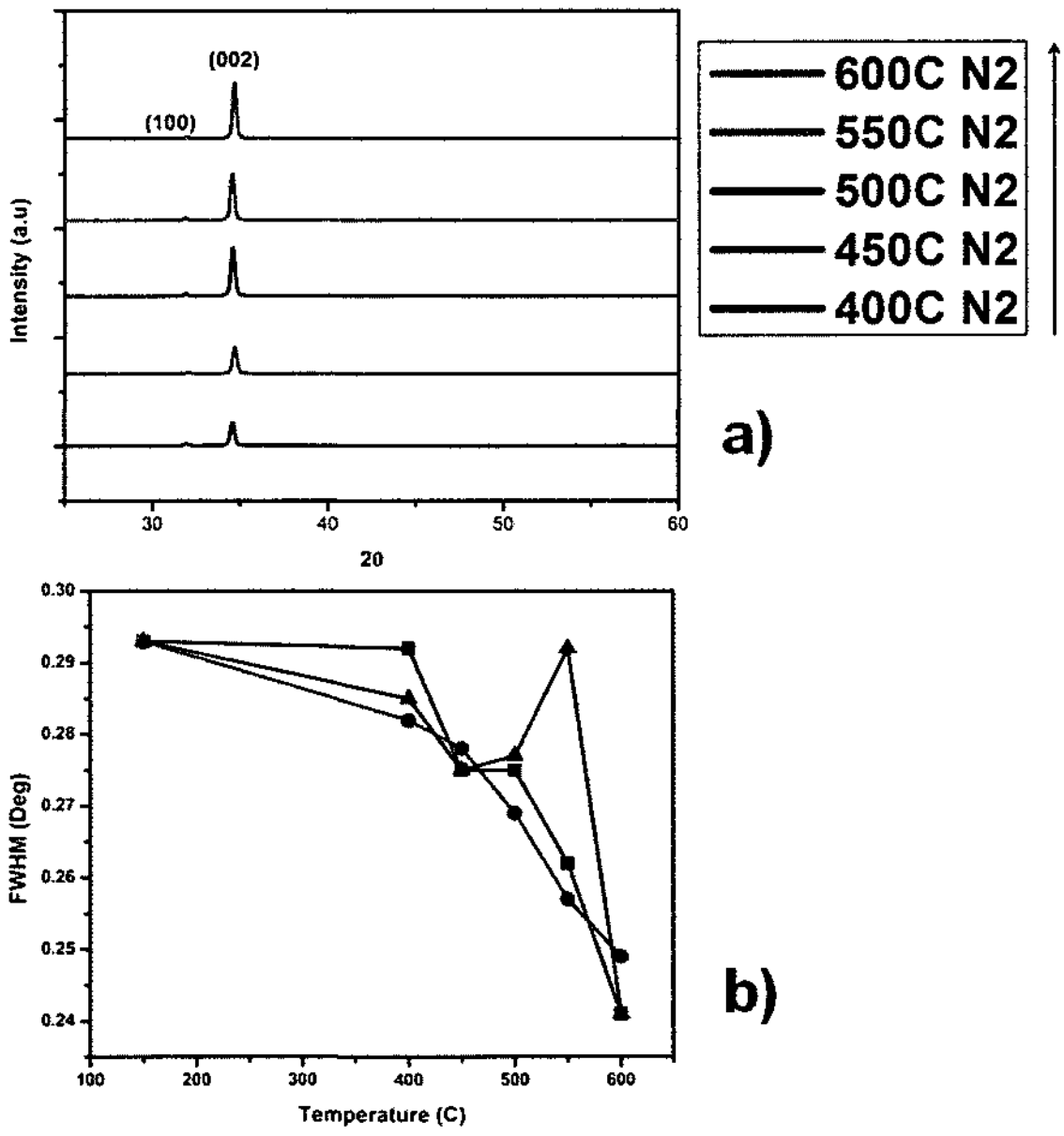

Figure 33. a) XRD plot as a function of different annealing temperatures in N_2 b) FWHM in the (002) plane for post deposition annealing in N_2 (red circle), O_2 (blue up triangle) and room ambient (black square).

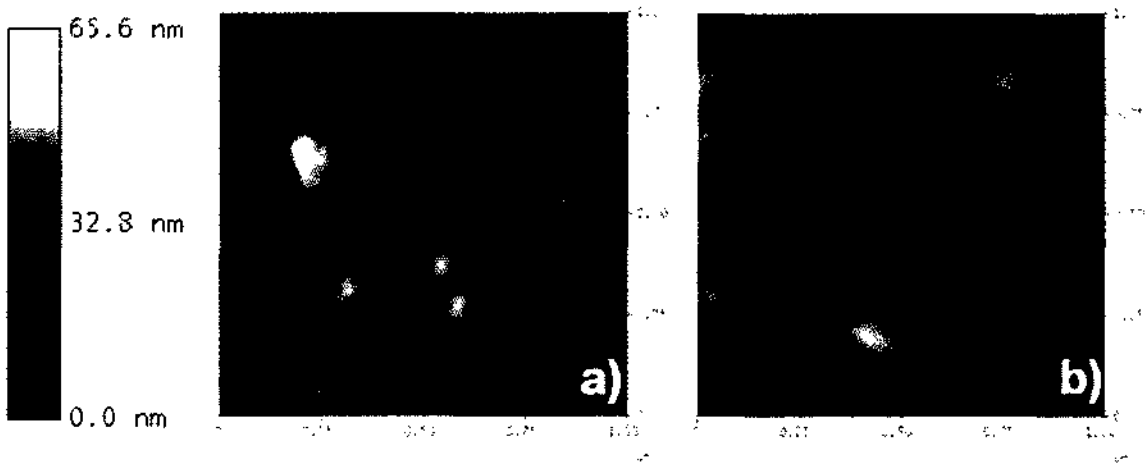

Figure 34. a) AFM analysis of ALD ZnO film (400 *nm*) annealed at 400 *°C* compared to b) ALD ZnO film (400 *nm*) annealed at 600 *°C*. The annealing environment is N_2

Table 9. Crystallite size calculated from Scherrer's formula for the annealed samples. Repeat the calculation.

Annealing Temperature (°C)	Crystallite size (*nm*) PDA Air	Crystallite Size (*nm*) PDA N_2	Crystallite Size (*nm*) PDA O_2
400	28.50	29.49	29.19
450	30.24	29.92	30.25
500	30.24	30.92	30.03
550	31.75	32.36	28.51
600	34.51	33.40	34.52

The thermal expansion coefficients of hexagonal ZnO at room temperature are respectively 4.75×10^{-6} $/^{o}K$ and 2.9×10^{-6} $/^{o}K$ along the c and a axis while Si has a thermal expansion coefficient of 2.61×10^{-6} $/^{o}K$.[48,49] Due to the difference of thermal properties between Si and ZnO, a built-in stress is expected as the samples undergo different thermal anneal cycles. This built-in stress in the films causes a shift in the XRD peak position from the bulk ZnO (002) peak value. The biaxial film stress (σ) was characterized using the relationship described in detail by Hong et al. [50] and is described as follow:

$$\sigma_{ZnO} = \frac{2C_{13}^{\ 2} - C_{33}(C_{11} + C_{12})}{2C_{13}} \times \frac{C_{film} - C_{bulk}}{C_{bulk}} \qquad (26)$$

where C_{11}= 208.8 GPa, C_{12}= 119.7 GPa, C_{13}= 104.2 GPa, and C_{33}= 213.8 GPa are the elastic contants of single crystal bulk ZnO from ref (22). C_{film}, and C_{bulk} are the lattice constants of the ALD ZnO films and bulk ZnO respectively.

The biaxial stress was characterized for the 400 *nm* thick ALD ZnO films on Si annealed at temperatures ranging from 400 ^{o}C to 600 ^{o}C. The annealing environment was also varied using N_2, O_2, and room ambient. The results are displayed in Figure 35. The stress in Figure 35 is a combination of both the stress from the thermal mismatch and the internal built-in stress from the film. Our results reveal that RTA annealing in N_2 ambient produced the lowest overall film stress. This result can be understood by invoking the intrinsic defect model for ZnO. The as-deposited ZnO films exhibit different intrinsic defects such as oxygen and zinc vacancies and interstitials responsible for the electrical and optical properties of ZnO. Annealing in O_2 environment reduces those native defect concentrations. Effect of O_2 ambient gas can be interpreted by the following reactions:

$Zn_{Zn} + V_o + O_2 \rightarrow ZnO + O_i$ (27)

$Zn_i + O_2 \rightarrow ZnO + O_i$ (28)

$2Zn(OH)_2 + O_2 \rightarrow 2ZnO + 2H_2O\uparrow$ (29)

During annealing in O_2 ambient gas, one of the above reactions can happen. The concentration of the intrinsic defects responsible for the electrical properties such as oxygen vacancy and zinc interstitials is reduced; hence, an increase in resistivity is observed. Similarly, the effect of N_2 on the intrinsic defects can be explained by the above equations. By replacing O_2 by N_2 no reduction of the vacancies is achieved; however, a slight increase of the vacancies concentration is achieved. This effect is well corroborated by the high resolution XPS scans of the O_{1s} peak (especially the oxygen deficient region denoted by O_b).

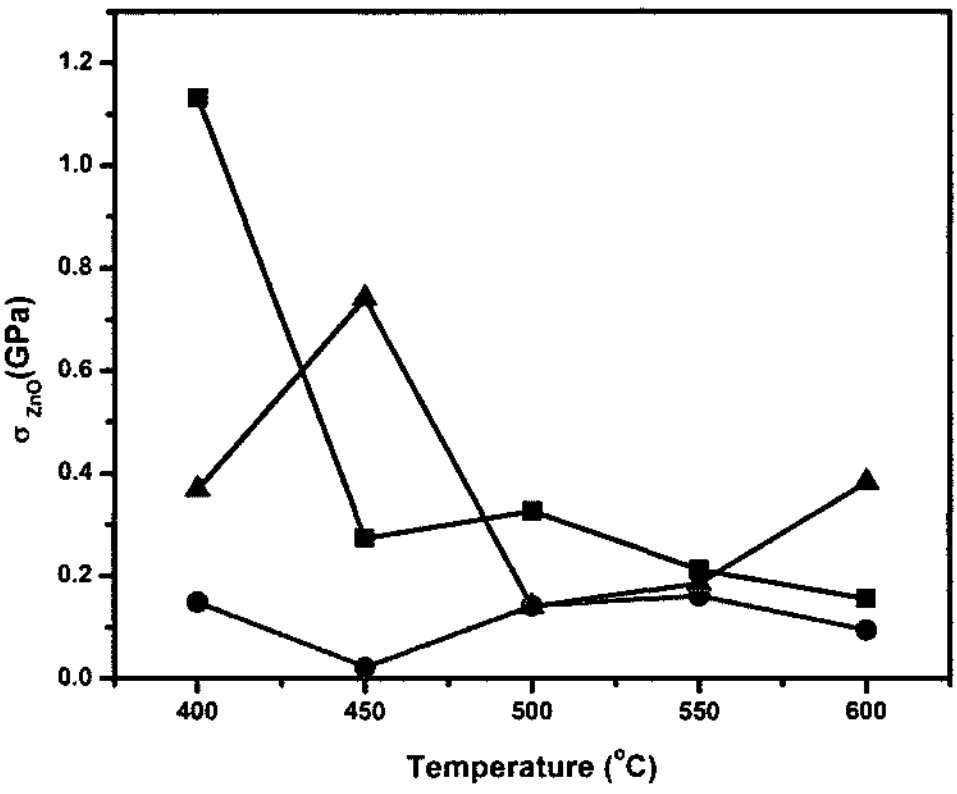

Figure 35. Built-in stress in the ZnO films vs. annealing temperature in N_2, O_2 and room air. (red circle) Annealing in N_2 ambient. (blue up triangle) Annealing in O_2 ambient. (black square) Annealing at room ambient.

Next, X-ray photoelectron spectroscopy was performed to investigate the chemical state of the ALD ZnO films. The XPS measurements were carried out using a Phi Quantera SXM X-ray photoelectron spectrometer with a monochromatic AlK_α radiation source (hv=1486.6 *eV*). Before measurement, the samples were sputtered clean in the vacuum chamber to remove any surface contamination. For accuracy, the XPS measurements of the ALD ZnO films were calibrated using the binding energy of C 1s. The C 1s peak was observed at 285.53 *eV* for the as-deposited ZnO films. A survey scan

of an as-deposited 400nm thick ALD ZnO sample is shown in Figure 36. The main peaks observed from the XPS spectra are Zn, O, Auger Zn LMN and OKLL. The chemical state of Zn in ZnO is investigated by analyzing the Zn2p peak and that of O in ZnO is analyzed by O1s peak. The as-deposited ZnO films show an O 1s peak at 530.53 *eV*. The Zn2p shows a doublet, the Zn2p3 and Zn2p1. The Zn2p3 peak was observed at 1022.53 *eV* while the Zn2p1 was observed at 1045.53 *eV*. The measured peaks of the O 1s and Zn2p are in agreement with the literature value of bulk ZnO confirming very good quality ZnO films; however, the binding energy of Zn2p in ZnO and in metallic Zn are very close making it difficult to investigate the chemical state of the Zn2p. Auger peak investigation of the ZnLMM is more sensitive to the analysis of the Zn state. The ZnLMM peak in metallic Zn can be observed at 992 *eV* and that of the as deposited ALD ZnO films was observed at 977.5325 *eV*.[51] The lower shift in ZnLMM peak shows most of the Zn elements exist in Zn^{2+} state.

A high resolution valence band spectrum was done on the as deposited ALD ZnO samples to investigate the energy bands. The valence band maximum (VBM) position was obtained by linear extrapolation. The intersection of the fitted line through the base line and the tangent to the peak is defined as the valence band maximum. Figure 37 shows the spectrum of the valence band of ALD ZnO. The VBM is the energy difference between the valence band and Fermi level E_F. For the as-deposited ALD ZnO, the VBM is found to be 3.25 *eV* below the Fermi level.

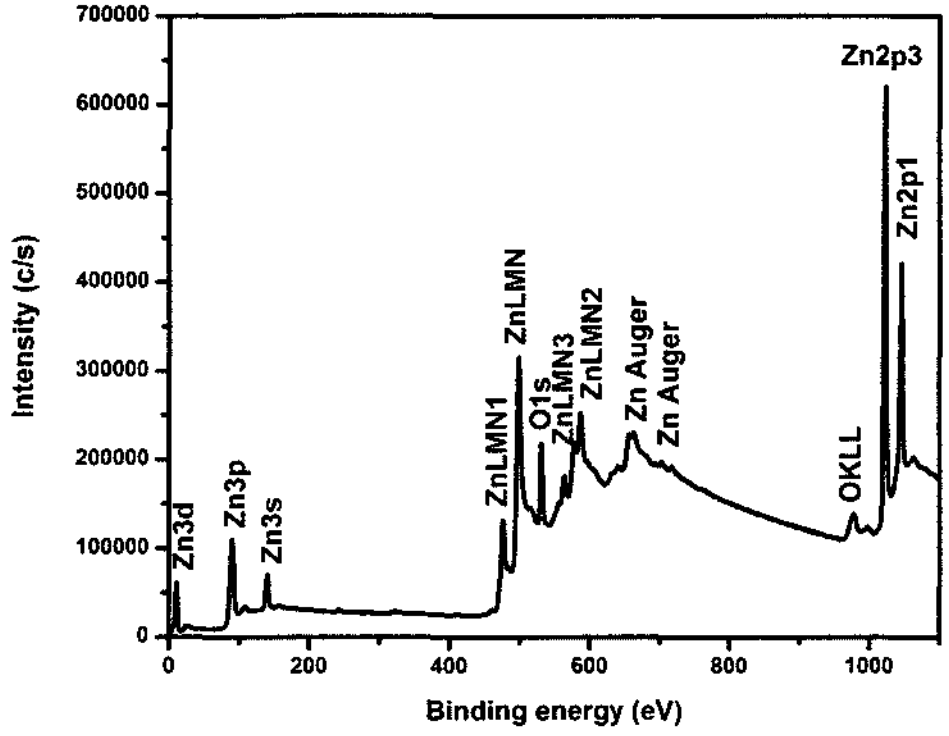

Figure 36. XPS analysis of as-deposited ALD ZnO films of 400 *nm* thickness.

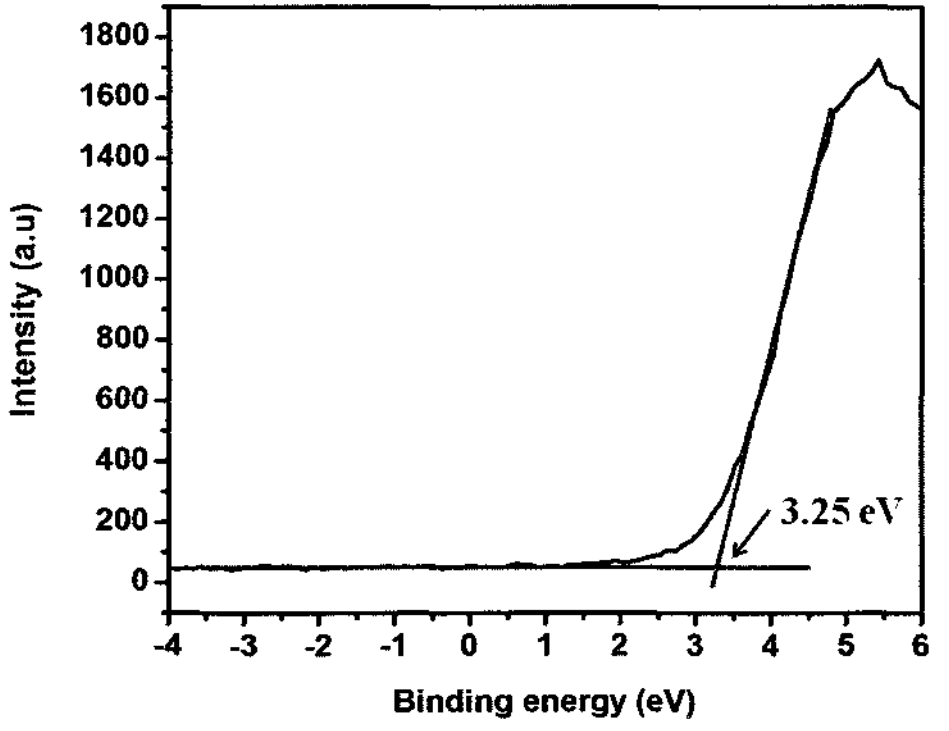

Figure 37. Valence band spectrum of the as-deposited ALD ZnO

The position of the Fermi level with respect to the conduction band minimum can be estimated by the following mathematical model:

$$E_F - E_C = \frac{KT}{q}\ln(\frac{N_D}{N_C}) \quad (30)$$

where E_C= conduction band minimum, E_F = Fermi level, N_D = n-type carrier density, N_c = effective density of states in the conduction band, $\frac{KT}{q} = 0.026\,eV$.

$$N_C = 2\frac{(2\pi \times m_e^* \times KT)^{3/2}}{h^2} \quad (31)$$

where h = Bolztmann's constant and m_e^* = effective mass of an electron=0.25.[52,53,54] Using the effective mass listed above, the electron effective density of states is calculated to be ~ $3\times10^{18}\ cm^{-3}$. This result is consistent with the literature values. [52,53,54,55] Therefore, the position of the Fermi level with respect to the conduction band is estimated to be ~ 0.05 *eV*. This implies the Fermi level lies above the conduction band by 0.05 *eV*. Hence, it can be considered as a degenerate semiconductor n++. The experimental XPS analysis combined with the theoretically calculated position of the Fermi level provide the following energy band diagram for ALD synthesized ZnO in Figure 38.

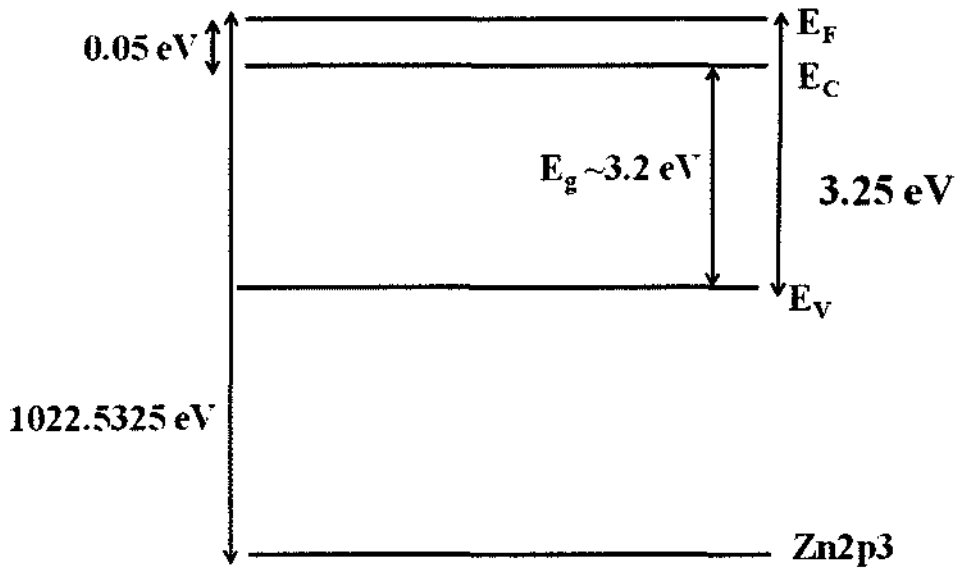

Figure 38. Energy band diagram of as-deposited ALD ZnO thin films

4.4.4 Conclusions

Good quality ZnO thin films were synthesized by atomic layer deposition. Our analysis reveals that ALD ZnO follows a Volmer-Weber type film growth. This growth mode can consistently explain the experimental results for varying temperature and different substrate materials. Once a nucleation site has formed, subsequent ALD cycles contribute to the growth of the crystallites resulting in appreciable grain growth. The ALD ZnO films exhibit a preferential growth direction in the (002) for the hexagonal wurtzite crystallographic phase. As the film thickness increases from 239 ALD cycles to 1900 ALD cycles, the intensity of the (002) peak increases. The as-deposited (002) peak intensity increased with temperatures. This observation was consistent regardless of annealing ambient gas. In summary, the ALD ZnO crystal quality was improved by

annealing. The built-in stress was characterized for the samples annealed in N_2, O_2 and room ambient. Annealing in N_2 ambient produced the lowest overall stress. During annealing in O_2 ambient gas, the concentration of the intrinsic defects responsible for the electrical properties such as oxygen vacancy and zinc interstitials is reduced; hence, an increase in resistivity is observed.

4.5 Raman Spectroscopy and Photoluminescence of ALD ZnO Thin Films

Zinc oxide (ZnO) is a direct wide bandgap semiconductor material with a variety of technologically interesting properties. The optical properties of ALD ZnO were investigated by Raman spectroscopy and photoluminescence. Raman spectroscopy is a non destructive optical characterization technique based on inelastic light scattering that provides information about the phonon vibrational and rotational mode properties of the ALD ZnO material under test. The interaction of the probing laser beam with the solid target produces a shift in the energy of the detected photons. Stokes shift defines a down shift to lower frequencies of the emitted photons, while the Anti Stokes shift designates an up shift. Experimental characterization of the vibrational properties is essential in accurately determining the transport properties which are important in order to design good quality optoelectronic devices and to characterize the ALD ZnO material by its characteristic phonon modes. Crystalline ZnO films are dominated by intrinsic point defects such as oxygen or zinc vacancies and interstitials or defect complexes which are largely responsible for the electrical and optical properties.[56] The issues and technical challenges surrounding these intrinsic point defects are a major reason why the fabrication of good, reliable p-n junctions in ZnO has eluded researchers for a long time. Those point defects and intrinsic defect complexes affect the transport properties. Raman

spectroscopy is sensitive to distortion in crystal lattice, crystal defects, and phase transformation.

Like most wurtzite crystal structure materials, ZnO belongs to the hexagonal system with space group C_{6v}^4 ($P6_3mc$) with two formula units per primitive cell, where all atoms occupy C_{3v} sites.[57] According to the group theory, the Raman active phonons are A_1 (z direction), E_1 (xy direction), and two E_2. The Raman non-active phonons are B_1. Both A_1 and E_1 are polarized phonons having each longitudinal optical (LO) and transverse optical (TO) components. E_2 corresponds to the non polarized phonon having two frequencies $E_{2(high)}$ and $E_{2(low)}$. Table 10 summarizes the literature values of the Raman active phonons in single crystal bulk ZnO.

Table 10. Optical modes of bulk single crystal ZnO.[57]

Optical Mode	Frequency (cm^{-1})
$E_{2(low)}$	101
$E_{2(high)}$	444
A_1 (TO)	380
A_1 (LO)	579
E_1 (TO)	413
E_1 (LO)	591

The vibrational phonon modes of polycrystalline ALD synthesized ZnO films on Si substrates were characterized with a Raman spectrometer (Inspector, DeltaNu) with a probing laser excitation wavelength at ~785 *nm* with ~40 *W* pump power. The signal was integrated for 2 sec and averaged 5 times for each measurement.

4.5.1 Results and Discussion

The Raman spectrum of the ALD thin films on Si (100) is displayed in Figure 39. From Figure 39, for 100 nm thick ALD ZnO and above, one can detect the Raman signal of optical phonons. For the highest ALD ZnO film thickness of 400 *nm*, there is the appearance of the E_2 (high) optical phonon at a frequency of 446.33 cm^{-1}. From Figure 39, the peak at 384.75 cm^{-1} corresponds to the A_1(TO) mode for the 400 *nm* ALD ZnO sample. The A_1 (TO) mode for the 200 *nm* ALD ZnO sample is located at 388.3 cm^{-1}. This corresponds to a red shift of the A_1 (TO) mode from the 200 *nm* to the thicker 400 *nm* ALD ZnO sample. The Stokes shift to lower frequencies is attributed to the presence of impurity defects.[58] The red shift is indicative of tensile stress in the as-deposited ALD ZnO thin films. The ALD ZnO films grown in this study showed no external impurity contamination in the films. Therefore, the only defects present are intrinsic defects inherent to ALD ZnO films. Based on the experimental evidence explained in the following sections the most probable intrinsic defects are oxygen vacancies. In a separate study, annealing of ALD ZnO in pure O_2 atmosphere revealed higher sheet resistivity values compared to annealing in pure N_2 atmosphere. In depth analysis about the nature of the intrinsic defects in ALD ZnO thin films will be performed in the near future.

From the XRD measurements, the ALD ZnO thin films have a preferential c-axis growth; however, during the initial nucleation phase the growth in the c-axis does not

dominate until a thickness ~ 100 *nm* ZnO is reached. [59] This might explain why the Raman modes are not distinguishable from the signal to noise ratio. The shift in the Raman frequencies is indicative of built-in stress. The E_2 optical mode is used to characterize the built-in inherent stress in the ALD ZnO films. From Figure 39a, the E_2 mode is shifted to higher frequencies or blue shifts. This is indicative of a compressive built-in stress in the film. No LO phonon was detected; however, a peak was observed at 280.93 cm^{-1}, and secondary phonons between 1200 cm^{-1} and 1500 cm^{-1}.

For benchmarking, single crystal bulk ZnO samples from Cermet were measured. Figure 39b displays the Raman spectra of bulk single crystal ZnO compared to the spectra obtained from a 400 *nm* polycrystalline ZnO film grown by ALD. Raman modes are very dependent on the selection rule. The observed phonons are dependent on the crystal orientation and the direction of propagation and polarization of the incident excitation light beam and the scattered light. The bulk single crystal ZnO sample was measured under the same conditions as the ALD polycrystalline ZnO thin films. The bulk single ZnO crystal exhibits a sharp and higher intensity E_2 (high) optical phonon mode at 442 cm^{-1}. The increase in signal intensity of the E_2 mode for the bulk ZnO compared with the ALD ZnO thin film is due to the high single crystal quality of bulk ZnO. Polycrystalline films tend to result in broader peaks compared to single crystal materials. The broader peak can be attributed to formation of the misfit and twin dislocation.

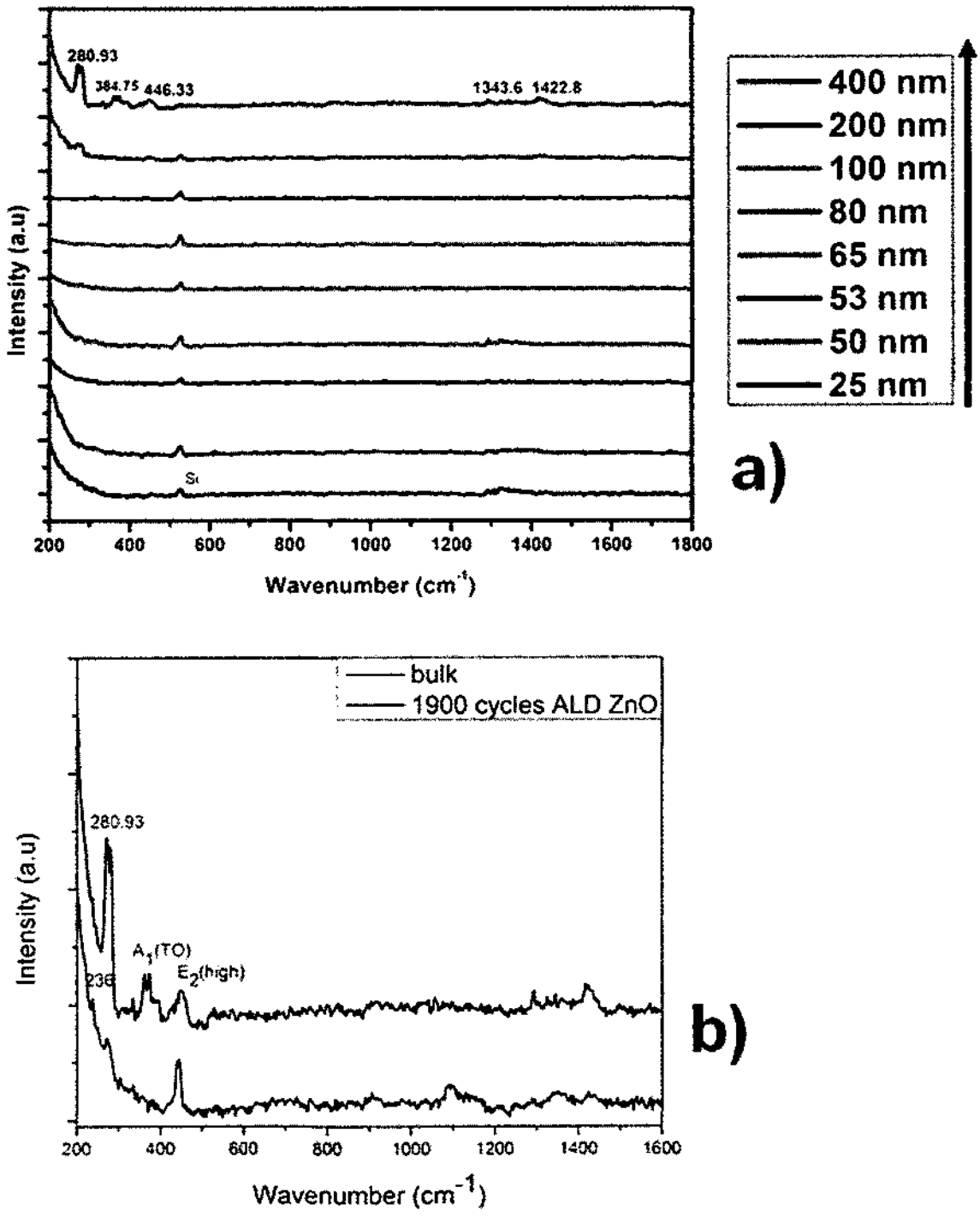

Figure 39. a) Raman spectra of as deposited ALD ZnO as a function of increasing film thickness. b) Raman spectra of as deposited polycrystalline 400 *nm* (1900 cycle) ALD ZnO (Black) and bulk single crystal ZnO (red).

When growing a dissimilar material on a substrate (such as hetero-epitaxy of ALD ZnO on Si) the lattice mismatch between the two materials imposes a stress on the growing film. The stress increases with increasing ALD ZnO thickness up to a critical thickness and then begins to decrease. The critical thickness is dependent not only on the lattice parameters but also on the Poisson ratio. The decrease of stress in the ALD ZnO films is due to the relaxation of the ZnO film on Si. The relaxation in the film is achieved through the formation of dislocation such as misfit dislocations. Both materials bulk ZnO, and the polycrystalline ALD ZnO thin films exhibit Raman peaks at 270 and 280 cm^{-1} respectively. We attribute those peaks to activation of the B_2 modes. It has been observed that the silent B_2 mode can be activated due to the electric field.[60] Macguire et al. have reported the appearance of a Raman peak at 276 cm^{-1} in ZnO nanobelts.[61] We observed a peak broadening in the frequency range of 1055-1173 cm^{-1} in the Raman spectrum of the bulk ZnO sample. E_1 optical phonon mode was detected for neither bulk single crystal nor the ALD ZnO sample. The peak at 236 cm^{-1} for both bulk single crystal ZnO and ALD ZnO thin films might be due to intrinsic defects.

The photoluminescence (PL) of ALD ZnO films was recorded using a 355 *nm* UV laser at room temperature. The PL spectrum of as-deposited ALD ZnO is shown in Figure 40. A strong UV band-edge emission can be observed at a wavelength of about 386 *nm* or 3.22 *eV*. The samples were benchmarked against bulk single crystal ZnO. The bulk single crystal ZnO exhibited a very close UV emission to the ALD ZnO thin films at 380 *nm* or 3.26 *eV*. A defect emission around 544 *nm* or 2.3 *eV* is also visible on the ALD ZnO films. This defect emission is due to the presence of oxygen vacancies in the as-deposited films. Absorption measurements are the most accurate optical measurement

techniques to calculate the optical bandgap. The standard procedure to experimentally determine the optical bandgap of semiconductors is to use optical absorption/transmission measurements. However, due to the move of an optical lab, the equipment for the optical absorption was not available. PL measurements of optical bandgaps are not 100% accurate because of the effect of shallow donor level near the conduction band edge on the emission spectrum. However, PL was the only optical equipment available. Therefore, PL provided a means to experimentally measure a near approximate value of the optical bandgap of ALD ZnO thin films. The optical bandgap of the as-deposited ALD ZnO is ~ 3.22 *eV* from PL measurements, which is comparable to the bulk single crystalline value of 3.3 *eV*. The measured band gap is in good agreement with the previously calculated bandgap value of 3.2 *eV*.

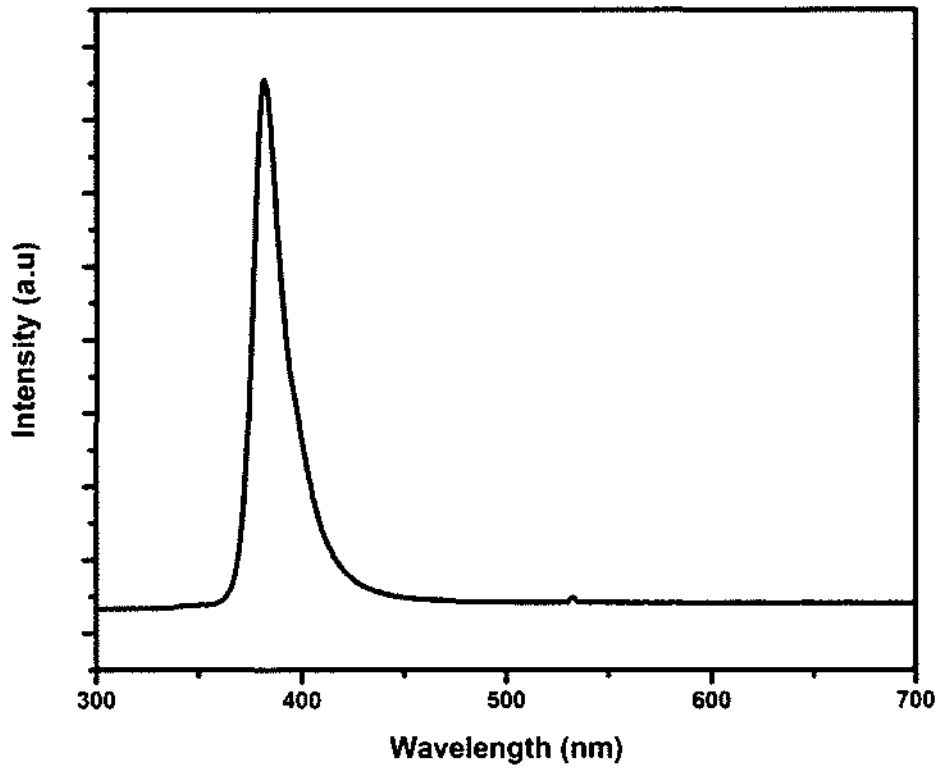

Figure 40. Photoluminescence of ALD ZnO thin films showing a strong band edge UV emission and slight defect emission.

4.5.2 Conclusion

Polycrystalline ZnO thin films were synthesized by atomic layer deposition (ALD). The X-ray diffraction (XRD) spectra showed a c-axis preferential growth in the (002) plane. The Raman spectroscopy study revealed a red shift in the Raman peak, which is indicative of built-in tensile stress. Our measurements show the appearance of the E_2 (high) optical phonon at frequency of 446.33 cm^{-1} for the thickest ZnO films. The peak at 384.75 cm^{-1} corresponds to the A_1 (TO) mode. There was no indication of any LO phonons; however, several phonon peaks at 280.93, 1343.6 and 1422.8 cm^{-1} were

observed. The bulk single crystal ZnO sample exhibits a sharp E_2 (high) optical phonon mode at 442 cm^{-1}. In contrast to the polycrystalline ALD ZnO thin films, the ZnO single crystal did not display the A_1(TO) optical phonon. E_1 optical phonon mode was detected for neither bulk single crystal nor the ALD ZnO sample. The peak at 236 cm^{-1} for both bulk single crystal ZnO and ALD ZnO thin films might be due to intrinsic defects. The ALD ZnO showed broader peaks of the A_1(TO) than the single crystal bulk ZnO. Polycrystalline films tend to result in broader peaks compared to single crystal materials. The broader peak can be attributed to formation of the misfit and twin dislocation. The stress increases with increasing ALD ZnO thickness up to a critical thickness and then begins to decrease. The critical thickness is dependent not only on the lattice parameters but also on the Poisson ratio. The elasto-mechanical properties of the novel ALD ZnO will be discussed in the following section.

4.6 Elasto-Mechanical Characterization of ALD ZnO by Nanoindentation

The Nanoindenter XP was used in conjunction with the continuous stiffness measurement in depth control mode to analyze the elasto-mechanical properties of ALD ZnO thin films samples. For comparison, we benchmarked the mechanical properties of single crystal bulk ZnO samples against our polycrystalline ALD ZnO thin films.

Among the novel thin film growth techniques, Atomic Layer Deposition (ALD) provides unique features such as precise control of ZnO thin films with atomic resolution, high uniformity, good conformity and high aspect ratio depositions; however, there exists a lack of systematic studies regarding the structural and mechanical properties of ALD grown ZnO thin films. The mechanical properties of single crystal bulk ZnO have been studied by various techniques such as X-ray diffraction (XRD),[62] and Vickers

microhardness tests.[63] Nanoindentation is a testing mechanism that is capable of accurately investigating the mechanical properties of thin film materials needed at the nanotechnology node. The mechanical properties of polycrystalline films exhibit a greater variation due to the grain sizes and defect content, the deposition methods and deposition parameters. Polycrystalline ZnO films have hardness and modulus values ranging from 1.5-12 *GPa* and 40-160 *GPa* respectively. Yoon et al. [64] have tested the mechanical properties of ZnO films deposited by PLD. PLD ZnO films were found to have a hardness of 10 *GPa* and a modulus of 150 *GPa*.

For this study, an MTS Nano Indenter XP equipped with a continuous stiffness measurement attachment was used to measure the mechanical properties. Nanoindentation testing is one of the most useful material testing methods in order to determine the mechanical properties of very thin film specimens. It consists of testing the specimen under study whose mechanical properties are unknown with another very hard indenter material whose mechanical properties are well known. Nanoindentation consists of applying known loads on the indenter shaft and measuring the indenter penetration depth through a capacitive sensing or inductive sensing network. The experimental set-up is shown in Figure 15. By plotting the load versus penetration depth, one can experimentally determine the modulus and hardness of the specimen tested. The CSM option adds experimental capabilities which were not previously available with conventional indentation testing methods. By introducing a small and well controlled oscillation into the normal loading sequence of the Nano Indenter®, the CSM allows the monitoring of the contact depth and the contact stiffness throughout the loading and unloading of the indenter shaft. Unlike conventional indentation testing methods, the use

of the CSM provides the advantage of measuring material hardness and elastic-modulus as a continuous function of depth. A three-sided pyramidal Berkovich diamond tip with a tip radius less than 20 *nm* was used. For validation, we indented deep into the bulk Si to obtain well documented bulk Si properties and for simulation purposes. A depth of 1 μm was used as the maximum depth of penetration of all four samples. A series of 10 indents were placed on each sample. The impression of the indents was scanned by the attached NanoVision unit. The ALD ZnO films were characterized for surface roughness and film quality. Atomic force microscopy (AFM) was used to determine the surface morphology. The AFM was used in contact mode. The AFM scan of a 1×1 *um* area is shown in Figure 41. The ALD ZnO samples are very smooth. The AFM analysis revealed a roughness RMS value of ~4 *nm* for a 400 *nm* thick ALD deposited ZnO thin film. From the TEM cross-sectional analysis, it was found that no columnar grains are present in the film. Instead, randomly oriented grains are observed demonstrating that the ZnO films deposited by ALD are polycrystalline films. This was confirmed by XRD analysis on 400 *nm* ALD ZnO films. Our as-deposited ALD ZnO thin films show a preferential growth in the c-axis. Figure 42 shows the XRD data of a 400 *nm* thick ALD ZnO thin film. The crystallite size was calculated to be 28 *nm* using Scherrer's formula.[47]

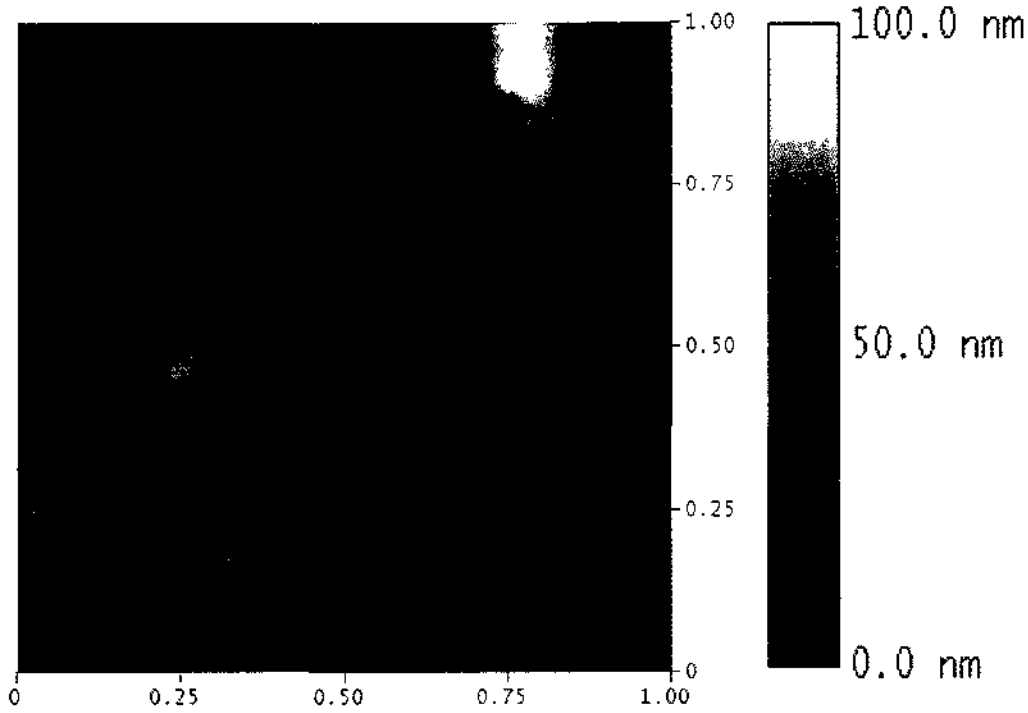

Figure 41. AFM micrographs of 400 *nm* ALD ZnO deposited at 150 *°C*. An RMS roughness value ~4 *nm* was obtained.

For this study, the elasto-mechanical properties of the polycrystalline ALD ZnO thin films were investigated using the Nano Indenter XP. Commerically available c-axis single crystal ZnO sample was also used as a reference. The equipment was used in depth control mode. Prior to the measurements, the tip was calibrated using a standard fused silica sample. The calibration was also conducted in between measurements and after the measurements.

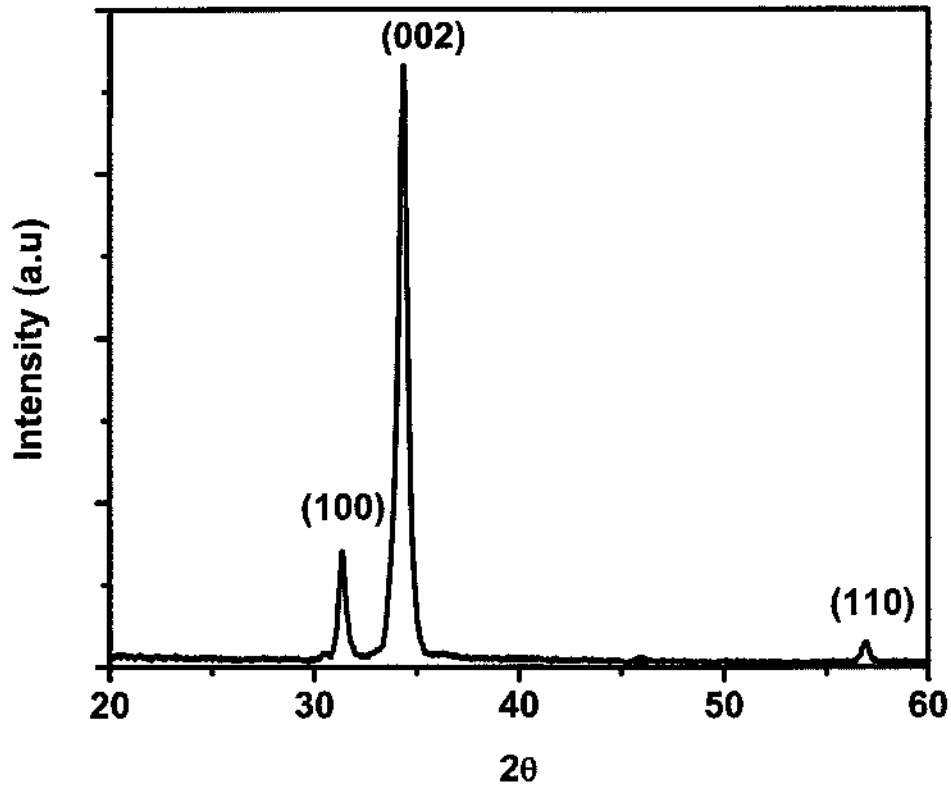

Figure 42. XRD pattern of as-deposited ALD ZnO films. The as-deposited samples shows the preferential growth in the (002) plane. The patterns were recorded using CuKα radiation (λ=1.54 Å).

To verify that the areas of indentation were accurately measured and that the indenter tip was appropriately calibrated, the contact depth versus the square root of the contact area $\sqrt{A}$ for fused silica, bulk single crystal ZnO, and ALD ZnO thin films was plotted in Figure 43. From Figure 43, it can be seen that the calibration for the three materials correlates well. Therefore, one can conclude that the areas of indentation measurements are accurate because both the modulus and hardness properties are very dependent on the accuracy of area measurements. Material deformations such as cracks,

pile-ups and sink-ins render it a challenge to measure the exact contact area, hence hardness and modulus. The contact areas were verified by an AFM around the Berkovich impression. Most of the discrepancy in the hardness measurements in the scientific literature is due to errors in the indentation area. The Poisson's ration and modulus values of the diamond tip used in the experiment are ν_d=0.07 E_d=1137 GPa respectively.

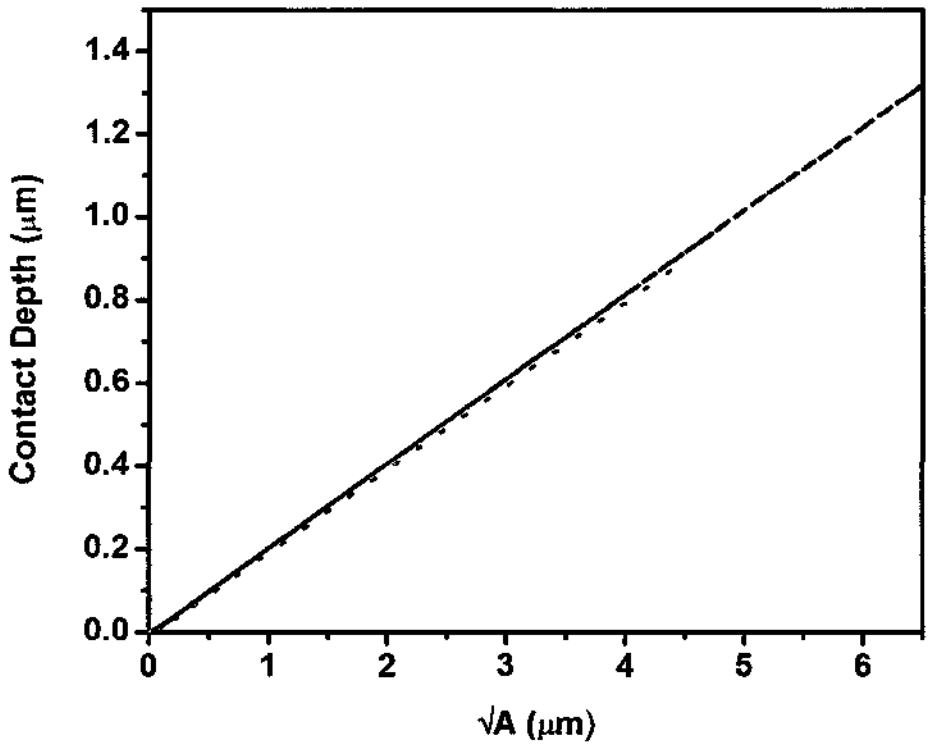

Figure 43. Contact depth as a function of square root of the contact area. (black dash line) Fused silica calibration. (red dotted line) Bulk single crystal calibration. (blue solid line) ALD ZnO film.

Indentation depths of 250 *nm*, 500 *nm*, and 1000 *nm* were performed on bulk single crystal ZnO. The loading curve overlaps for all three indention depths validating the accuracy of the measurement, see Figure 44a. For analysis of the data, the 1000 *nm* indents will be discussed for comparison to the ALD ZnO data. The modulus data and the hardness were calculated as a function of increasing depth. The Meyer hardness is the ratio of the maximum load (from the load-depth curve) over the projected indentation area.

The modulus is defined as the ratio of the slope of the unloading curve measured at the tangent to the data point at the maximum load and the projected area. The modulus and the hardness were recorded and plotted against the indenter contact depth. The modulus and hardness of bulk single crystalline ZnO are shown in Figure 45 as a function of the indentation depth. We measured a modulus value of 125 ± 1.6 *GPa* and a hardness value of 5.6 ± 0.09 *GPa* for our single crystal bulk ZnO reference sample. Our results are comparable to literature values of 111.2 ± 4.7 *GPa* and 5.0 ± 0.1 *GPa* obtained from bulk ZnO sample.[65]

The polycrystalline ALD ZnO thin films were also tested under the same conditions. The indentation depth was chosen to be 1000 *nm*. The load-depth curve of the ALD ZnO is shown in Figure 44b.

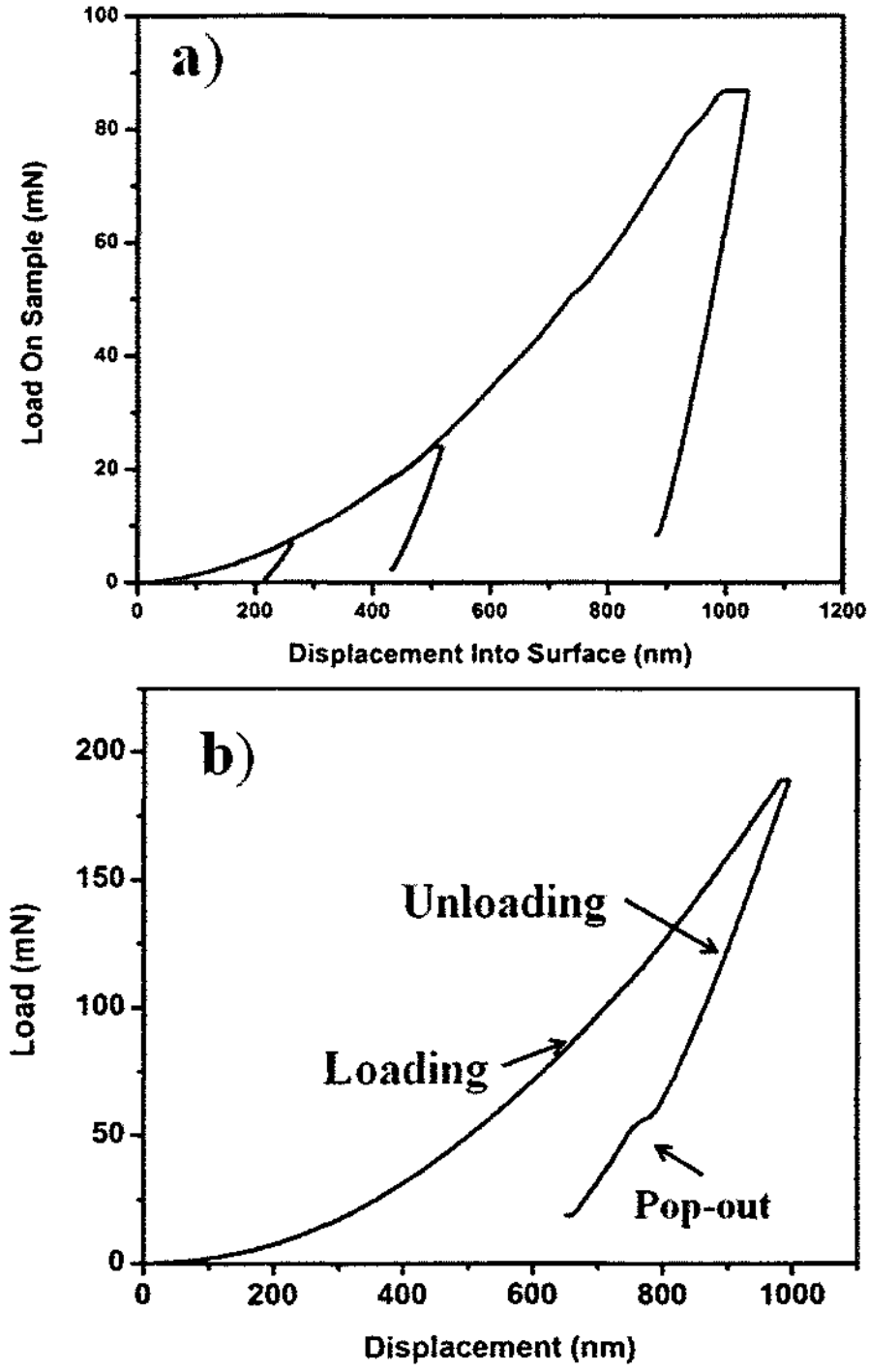

Figure 44. a) Load- depth curve of 250 *nm*, 500 *nm* and 1000 *nm* indentation depth on bulk ZnO. b) Load- depth curve of the ALD ZnO films.

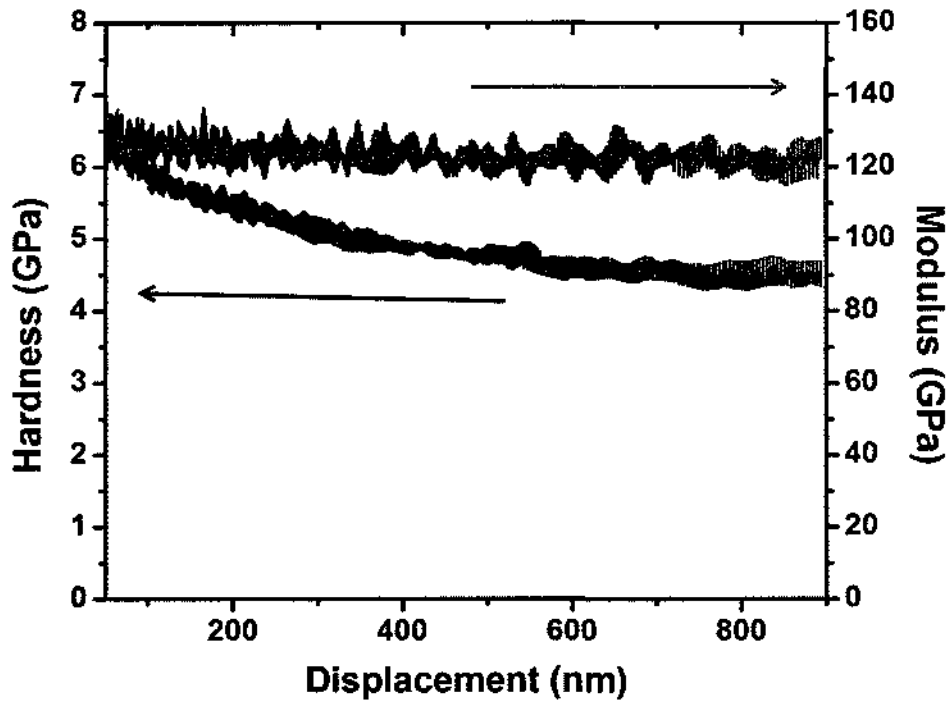

Figure 45. Modulus and hardness vs. displacement of bulk single crystalline ZnO. A set of 10 different indents were performed at 1000 *nm* depth using a diamond tip Berkovich indenter for bulk ZnO. The plot displays the average data of modulus and hardness.

In the case of multilayered dissimilar specimen data taken beyond 10% of the thin film thickness, the measurements are influenced by the substrate material.[66] For example, as the indentation depth gets closer to the interface between the thin film and the substrate, the effect of the substrates becomes more pronounced. Because we indented deep in the substrate, there is the influence of the underlining Si wafer. From Figure 44b), a pop-out event can be seen from the unloading curve of the ALD ZnO thin films. The pop-out behavior from the unloading curve is attributed to the underlying Si substrate.

Cubic Si is well known to undergo pressure induced phase transformation in nanoindentation. In the loading phase, the cubic Si transforms to metallic Si phase S-II. In unloading, the pressure releases cause further transformation into an amorphous Si or a mixture of bcc Si , rhombohedral Si depending on the unloading rate.[67,68,69] Yan et al have shown the critical load to cause a pop-out in cubic Si at ~ 30mN.[68] The indent penetration depth and loads are sufficient enough to cause phase transformations in the underlying Si substrate. Figure 46 shows 3-D AFM micrographs by the incorporated nanovision AFM equipment. Some pile-ups and radial cracks can be observed on the AFM images shown in Figure 46 due to the Si substrate material.

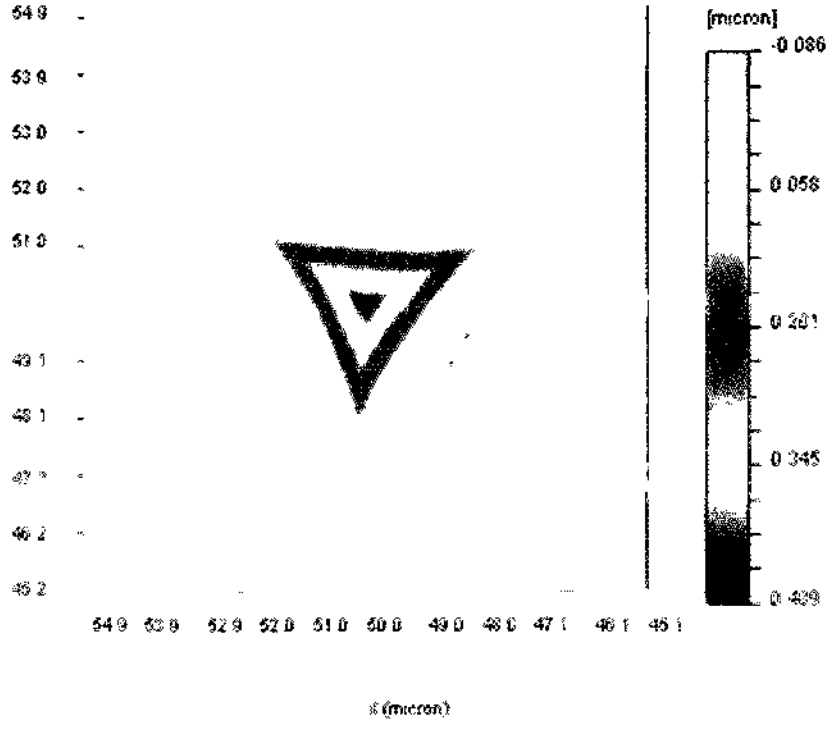

Figure 46. 3-D AFM plots by nanovision. Cracks are propagating radially and outward.

To take into account the substrate effect, simulations and modeling based on the contact area, the substrate properties, and the specimen compliance were calculated. The model employs linear elasticity theory to calculate the average elastic displacement beneath the uniformly loaded area. The unloading contact compliance is used to calculate the effective modulus and is given as follows:

$$C = \frac{1}{E_{eff}\sqrt{A}} = \frac{1}{\beta\sqrt{A}}\left[\frac{1}{E_r} + \frac{1-\nu_d^{\,2}}{E_d}\right] \qquad (3)$$

Where A = projected area, ν_d= poisson ratio of the diamond Berkovich indenter, E_d= modulus of the diamond Berkovich indenter, β= dimensionless constant related to geometry of the indenter, E_r= modulus of the specimen.

The Si substrate being harder confines plastic flow in the softer ALD thin film during testing resulting in an upward flow of the material which is then seen as pile-up around the indent. This phenomenon of enhanced pile-up of softer films on harder substrates was also observed by Tsui and Pharr[70] and also by Lee and Fong.[71]

The modulus data and the hardness data were simulated using elastic theory. More details about the simulation can be found in ref. (72). To estimate the elastic modulus (E_s) of the films, the effective modulus (E_{eff}) is plotted in Figure 47 with the simulation data. In this model the effect of the silicon substrate underneath the ZnO film is taken into account, and the E_{eff} of the elastic contact between the indenter and layered specimen is simulated for thin films with different E_s. The elastic properties of silicon used in the simulation were 161 *GPa* for E_s and 0.227 for Poisson's ratio (ν_s). The ν_s for the ZnO film was calculated to be 0.3. The data is normalized to the film thickness, allowing films of varying thicknesses to be directly compared to the same simulations.

Comparing the experimental data points to the simulated curves, the E_s for the as-deposited ALD ZnO thin film was calculated to be approximately 143±7 *GPa*. This modulus is higher than that of the bulk single crystal value.

The modulus and hardness of our polycrystalline ALD ZnO thin films were calculated to be 143± 7 *GPa* and 6.9± 0.6 *GPa* respectively.

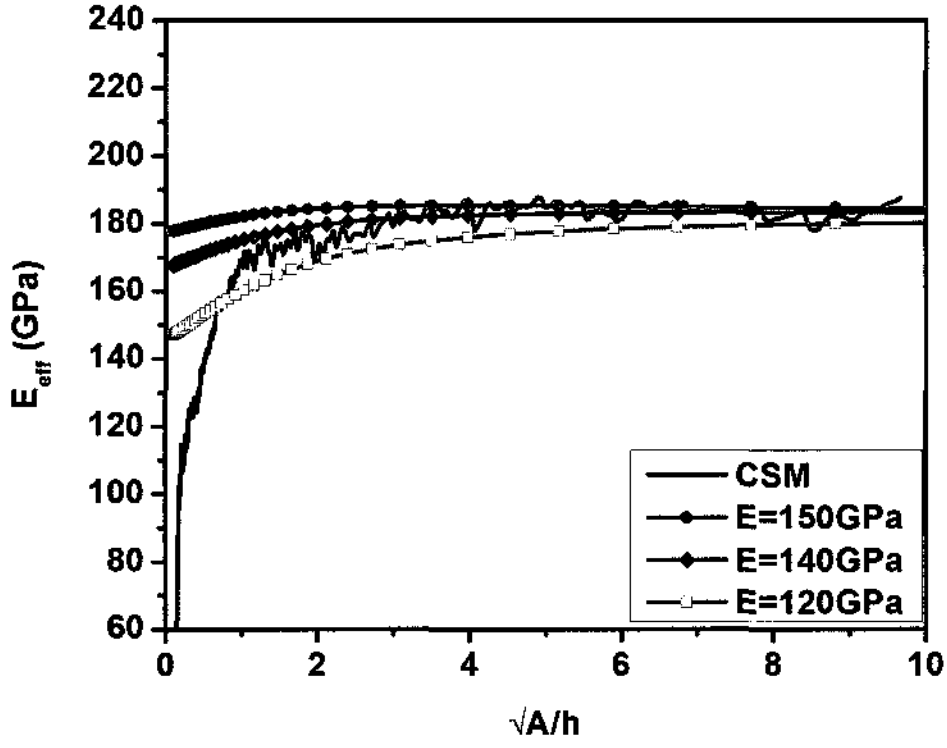

Figure 47. Effective modulus vs. square root of area normalized with the thickness. The solid line represent CSM experimental data and the symbols are the simulated results of Stone's model for films with different. E_{eff} = effective modulus, A= contact area, h= film thickness, A= contact area. The simulation curves are E = 120 *GPa*, 140 *GPa* and 150 *GPa*. CSM = experimental data. ν= poisson ratio

4.6.1 Conclusion

ZnO is a versatile material with numerous properties that make it suitable for renewable energy, white LEDs, spintronics, piezoelectric and ferromagnetic applications. We successfully deposited low temperature ZnO thin films by ALD. The physical properties of the ALD thin films were studied by TEM, AFM, XRD and nanoindentation. Based on the experimental results and modeling the film growth mode for ALD ZnO has been found to follow the Volmer-Weber island growth. Our as-deposited ALD ZnO thin films are polycrystalline. We have reported here the modulus and hardness of ALD ZnO and benchmarked it against crystalline bulk ZnO using nanoindentation techniques. Bulk single crystal ZnO was measured to have a modulus value of 125± 1.6 *GPa* and a hardness value 5.6± 0.09 *GPa*. Simulations based on Stone's model of elastic rebound between an indenter and a composite multi-layered specimen were used to accurately extract the modulus of our polycrystalline ALD ZnO thin films on Si (100). The modulus and hardness of our polycrystalline ALD ZnO thin films were calculated to be 143± 7 *GPa* and 6.9± 0.6 *GPa* respectively.

4.7 Investigation of Electrical Properties of ALD ZnO

After deposition, the ALD ZnO samples were subdivided into multiple pieces by cleavage and their electrical properties were investigated by four-point probe. To limit the effect of Si on the resistivity measurements, an insulating layer is present between the ZnO layer and the Si substrate. Figure 48 shows the sheet resistance measurements of the as-deposited samples. The resistivity for the ALD ZnO films below 200 ALD growth cycles is high and rapidly decreases as the ALD ZnO film thickness increases. The as-deposited ZnO thin films are very conductive. The initial high resistivity for very thin

ZnO films provides experimental evidence for incomplete ZnO films during the island nucleation phase. Once the islands grow into a continuous ZnO film the resistivity drops rapidly to its final value. The ALD ZnO thin films have a lower resistivity (~0.02 *Ω-cm* for 400 *nm* thick ALD ZnO) than that of the bulk single crystal ZnO (0.364 *Ω-cm*). The resistivity decreases as the film thickness is increased and saturates for the ALD growth cycles higher than 500 cycles or 100 *nm* thick films to a value of ~ 0.02 *Ω-cm*. In general, the decrease in resistivity with increasing film thickness can also be explained by the reduction of surface states, interface scattering and the incorporation of more defects (oxygen vacancies and interstitials, Zn interstitials).[73] The incorporation of more structural defects in the films during deposition reduces the electron mean free path; as a consequence, the electrical resistivity is enhanced. For the very thin films, the increase of the effect of scattering of the electrons at the interface influences the resistivity measurements. This effect is further annihilated in the thicker films. Surface scattering and grain boundaries scattering affect very thin films disproportionately more resulting in an increased resistivity values. [74]

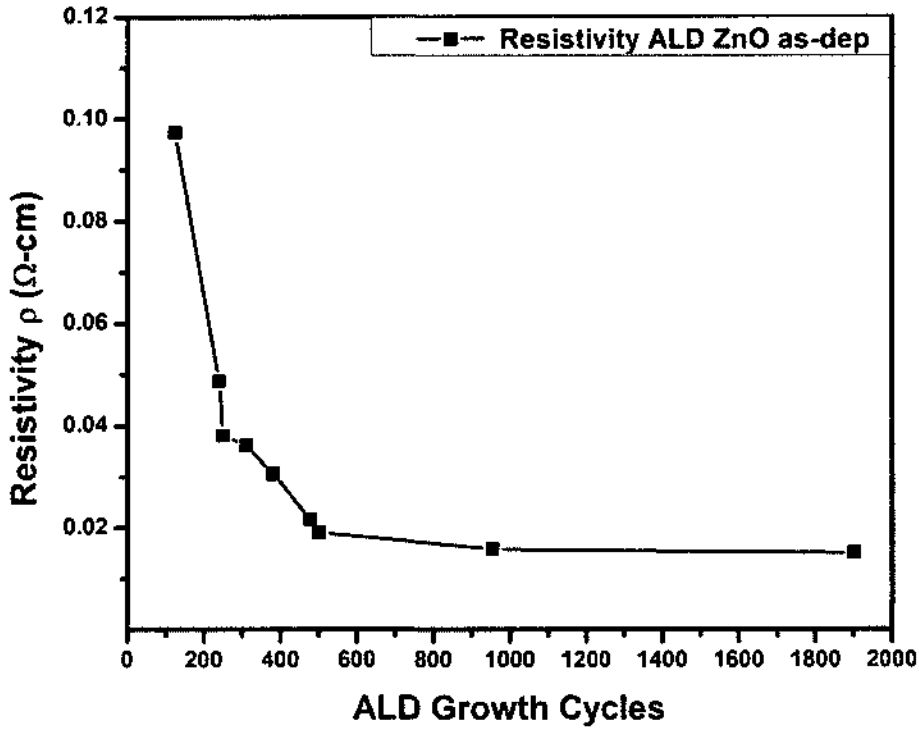

Figure 48. Sheet resistance as a function of ALD growth cycles.

The ALD ZnO films' conductivity was also investigated as a function of deposition temperature. For this experiment 50 *nm* thick ALD ZnO thin films were grown at deposition temperatures of 100 ^{o}C, 125 ^{o}C and 150 ^{o}C. All other deposition parameters and the sample cleaning procedure remained unchanged. After ALD ZnO film deposition, the surface conductivity was investigated employing the conductive AFM mode. A description of the apparatus is shown in Figure 49. An area of 1μm × 1μm was scanned. The ZnO samples were biased at a voltage of 2 *V*. The surface current intensity goes from light (lowest = 0 *fA*) to dark red (highest=1 *pA*). The dark red spots represent areas of high current density and the yellow spots are areas of low current density. The measurements show an increase of conductive areas with increasing deposition temperature. This can be explained by the fact that the defects responsible for the surface

conductivity in the as-deposited ALD ZnO are not activated at low temperatures. A minimum activation energy is required. For deposition temperature of 125 ^{o}C and beyond, the surface conductivity increases. A visual map of the surface conductivity is shown in Figure 50.

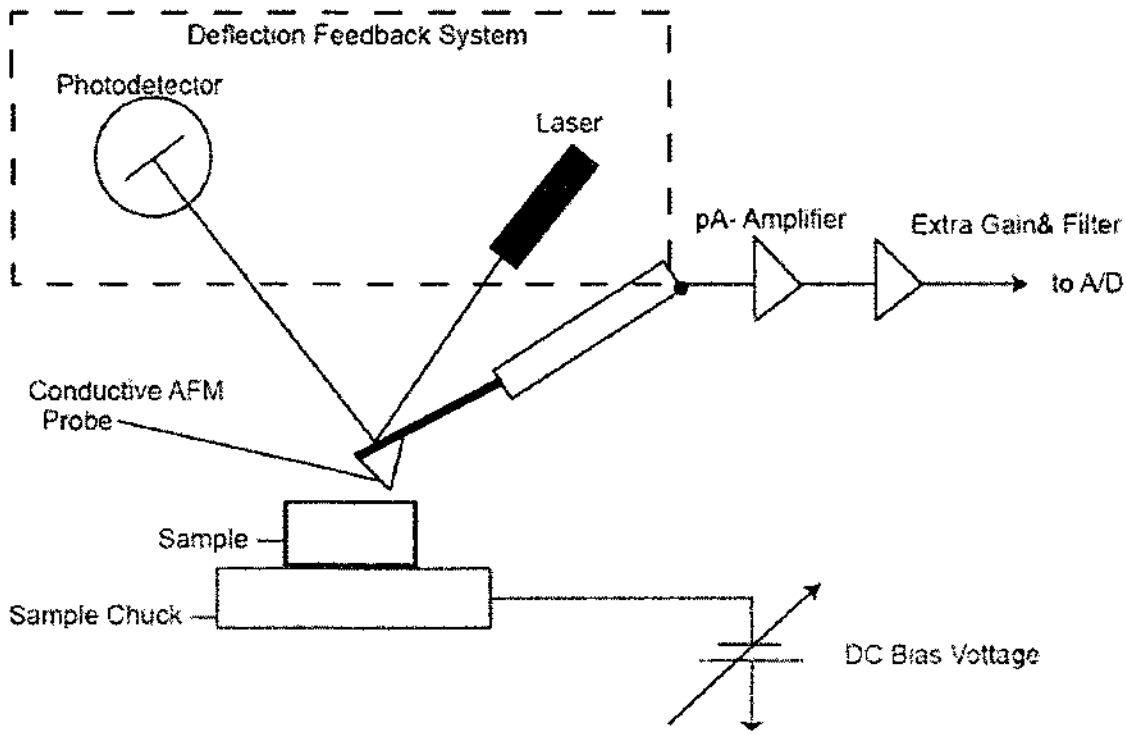

Figure 49. Schematic of the conductive AFM apparatus

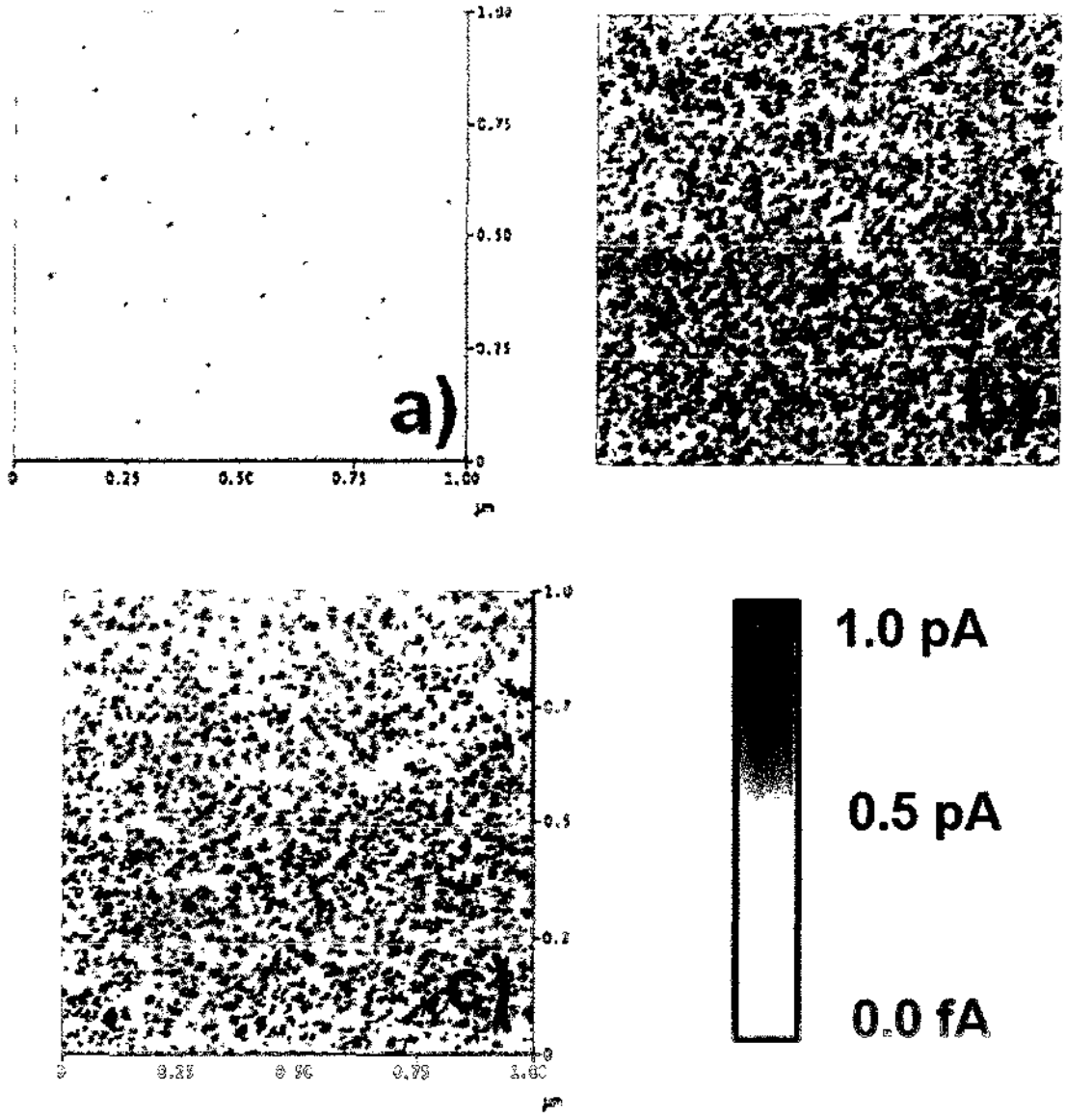

Figure 50. a) 50 *nm* ALD ZnO deposited at 100 *°C*. b) 50 *nm* ALD ZnO deposited at 125 *°C*. c) 50 *nm* ALD ZnO deposited at 150 *°C*.

A 400 *nm* thick ALD ZnO thin film was deposited on a 4 inch Si (100) wafer at 150 ^{o}C and subdivided by cleaving into different sample sets. One set was annealed in air for 10 minutes at 400 ^{o}C. Another set was annealed in forming gas (95% N_2 and 5% H_2) for 10 minutes at 400 ^{o}C. A third set was not annealed and used as a reference sample. The annealing experiment was carried out in a rapid thermal annealing system. The surface conductivity was also investigated using the same conductive AFM apparatus shown in Figure 49 to investigate the effect of annealing on the surface defects of the ALD ZnO films. The surface current intensity goes from light (lowest = 0 fA) to dark red (highest=5 pA). It can be seen from Figure 51 that the conductivity of ZnO film surface is only significantly changed when annealed in air. The surface conductivity of the as-deposited ZnO films and films annealed in forming gas does not change significantly. Annealing in forming gas is passivating the dangling bonds at the surface and in the grain boundaries; however, annealing in air reduced the surface defects present on the surface. Further investigation of the effect of annealing on the structural defects will be presented later on in another chapter in this dissertation.

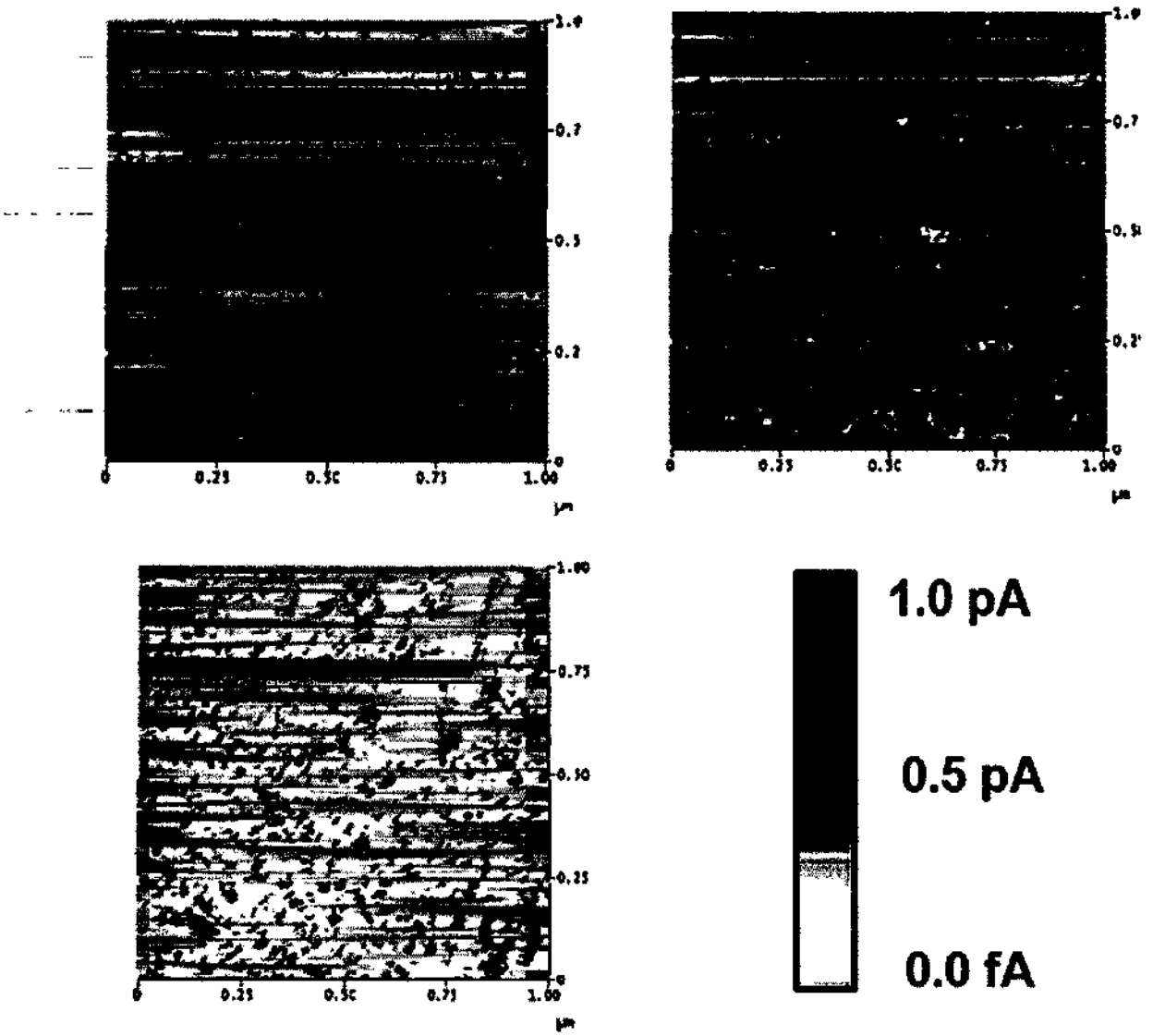

Figure 51. Conductive AFM mapping of ALD ZnO films. a) as-deposited 400 *nm*. b) Annealed in forming gas. c) Annealed in Air. The annealing time and temperature for all samples are 10 minutes and 400 ^{o}C respectively.

The effect of annealing on the film's structural defects and their identification was further investigated. After ALD ZnO film deposition a portion of the samples were divided by cleaving for post deposition anneal (PDA) in room ambient, nitrogen ambient, and oxygen ambient in a rapid thermal annealing system (Solaris 150 by Surface Science Inc). The annealing temperatures range from 400 ^{o}C to 600 ^{o}C for 1 hour. The resistivity of the samples annealed in room ambient, N_2, and O_2 atmospheres were measured using a four-point probe. The resistivity measurements of the annealed samples are displayed in Figure 52. The samples annealed in pure N_2 atmosphere reveal about 2 orders of magnitude lower resistivity values compared to annealing in pure O_2 atmosphere and about 3 orders of magnitude lower resistivity values compared to annealing in room ambient for annealing temperatures lower than 550 ^{o}C. At higher annealing temperature the values for all three ambient appear to converge. The as-deposited ZnO films exhibit different intrinsic defects such as oxygen and zinc vacancies and interstitials responsible for the electrical and optical properties of ZnO. Annealing in O_2 and air atmosphere reduces those structural defects only to some degree. As a result, thermal treatment in those environments was found to reduce the conductivity values of the samples. The most dramatic resistivity reduction is achieved for annealing in pure N_2 atmosphere.

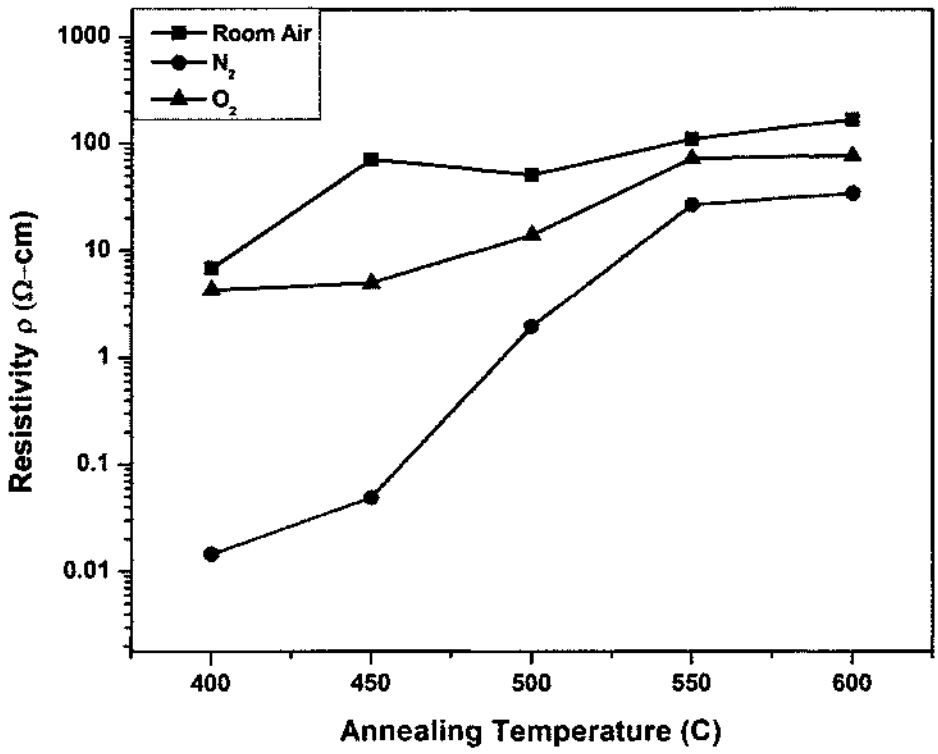

Figure 52. Resistivity of ALD ZnO films as a function of annealing temperature as a function of different annealing ambient in O_2, N_2, and room ambient.

For an in-depth study, high-resolution XPS scans of the O 1s peaks of the ALD ZnO samples annealed in air, O_2 and N_2 gas were performed. For the as-deposited ZnO sample, the O 1s peak shows an asymmetric feature and a shoulder in the HR XPS profile as seen in Figure 53. The spectra are fitted by three peaks centered at binding energy of 531.01 *eV*, 532.55 *eV* and 533.19 *eV*. The lower binding energy peak at 531.01 *eV* is due to O^{2-} ions on the wurtzite structure of the hexagonal Zn^{2+} ions. In this dissertation, the lowest peak will be referred to as O_a, the medium peak as O_b and the highest peak as O_c. This is attributed to the Zn-O bonds whereby each Zn atom is bonded to 4 O atoms or

vice versa. The intensity of the peak O_a with the lowest binding energy is the highest and contributes about 81% of the total area indicating a strong Zn-O bonding or wurtzite hexagonal formation in the ALD ZnO thin films. The shift of the lowest binding energy peak O_a to higher energy values from the published literature value indicates show an increase concentration of oxygen vacancies.[75] The medium and highest binding energies at 532.55 *eV* and 533.19 *eV* are thought to be due to OH^- groups and adsorbed water molecules forming $Zn(OH)_2$. These OH^- are adsorbed only at the ZnO surface. The component of the medium peak O_b is attributed to the oxygen deficient region in ZnO. Hydrogen forms a deep donor in ZnO. When H ions bond with O atoms in ZnO, oxygen vacancies are created in the ZnO crystal lattice. The more H ions get absorbed, the higher the concentration of oxygen vacancies. The same observation is consistent with samples annealed in different environments. The high resolution XPS scans of O 1s of the as-deposited sample and the different annealing environments are shown in Figure 53. Figure 54a shows the shift in O_a peak as a function of the annealing environment. Oxygen and air annealing have the greatest shift in O_a peak position resulting in a shift towards lower binding energies close to the literature values of 530.53 *eV* indicating better crystallization and bonding between Zn and O species.[75] This is a result of the reduction of the oxygen vacancies. To corroborate, the O_b were also analyzed as a function of annealing temperature and annealing ambient gas. Figure 54b shows the plot O_b peak as a function of temperature; however, in the oxygen deficient region a decrease in both binding energy and intensity of the peak O_b is observed for annealing in O_2 and air environment. This effect can be interpreted as a decreased concentration of oxygen vacancies in the ALD ZnO samples because O_2 annealing diffuses a large supply of O

atoms into the ZnO crystal lattice resulting in a decrease of oxygen vacancies. N_2 annealing does not change significantly the intensity of the O_a and O_b peaks indicating the amount of oxygen vacancies did not decrease. This observation corroborates the resistivity measurements as a function of annealing ambient.

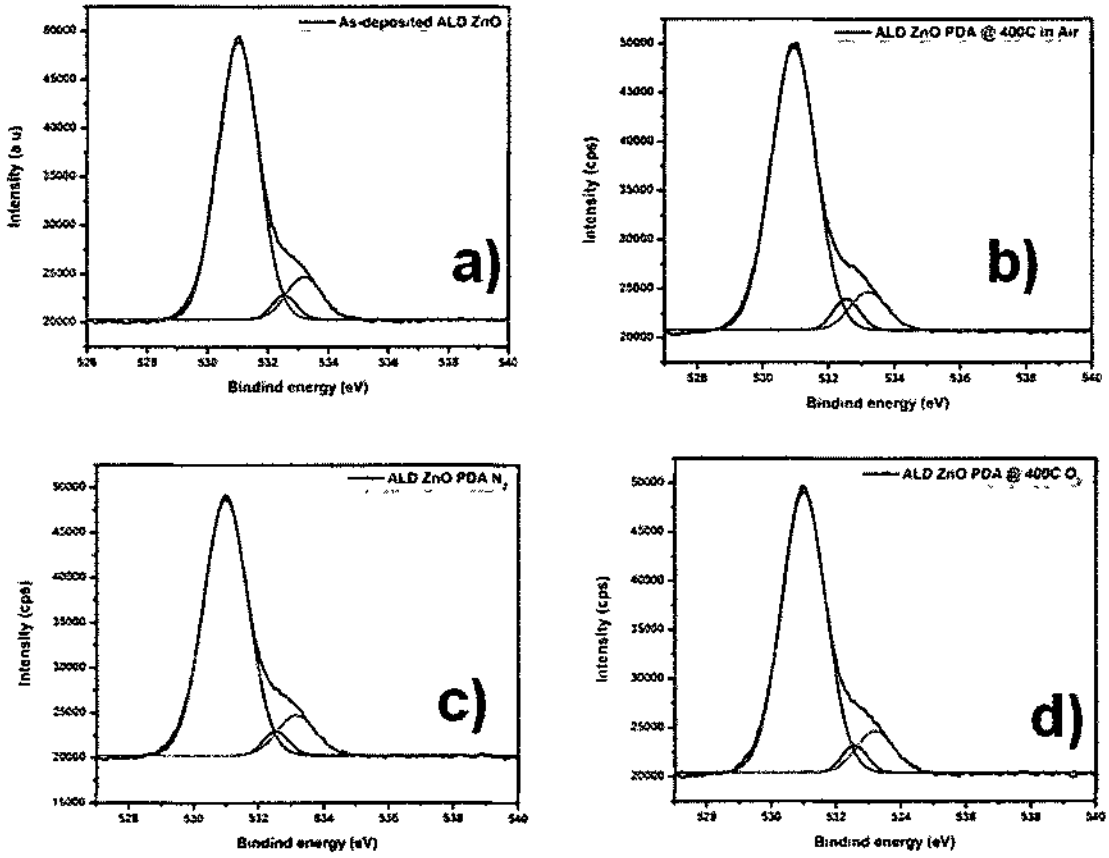

Figure 53. High-resolution scan of the O 1s peak. a) O 1s of the as-deposited ALD ZnO. b) ALD ZnO PDA at 400 ^{o}C in air. c) ALD ZnO PDA at 400C in N_2. d) ALD ZnO PDA at 400 ^{o}C in O_2. A shoulder is observed in all of the samples studied with high resolution XPS. The annealing time was maintained constant for 1 h.

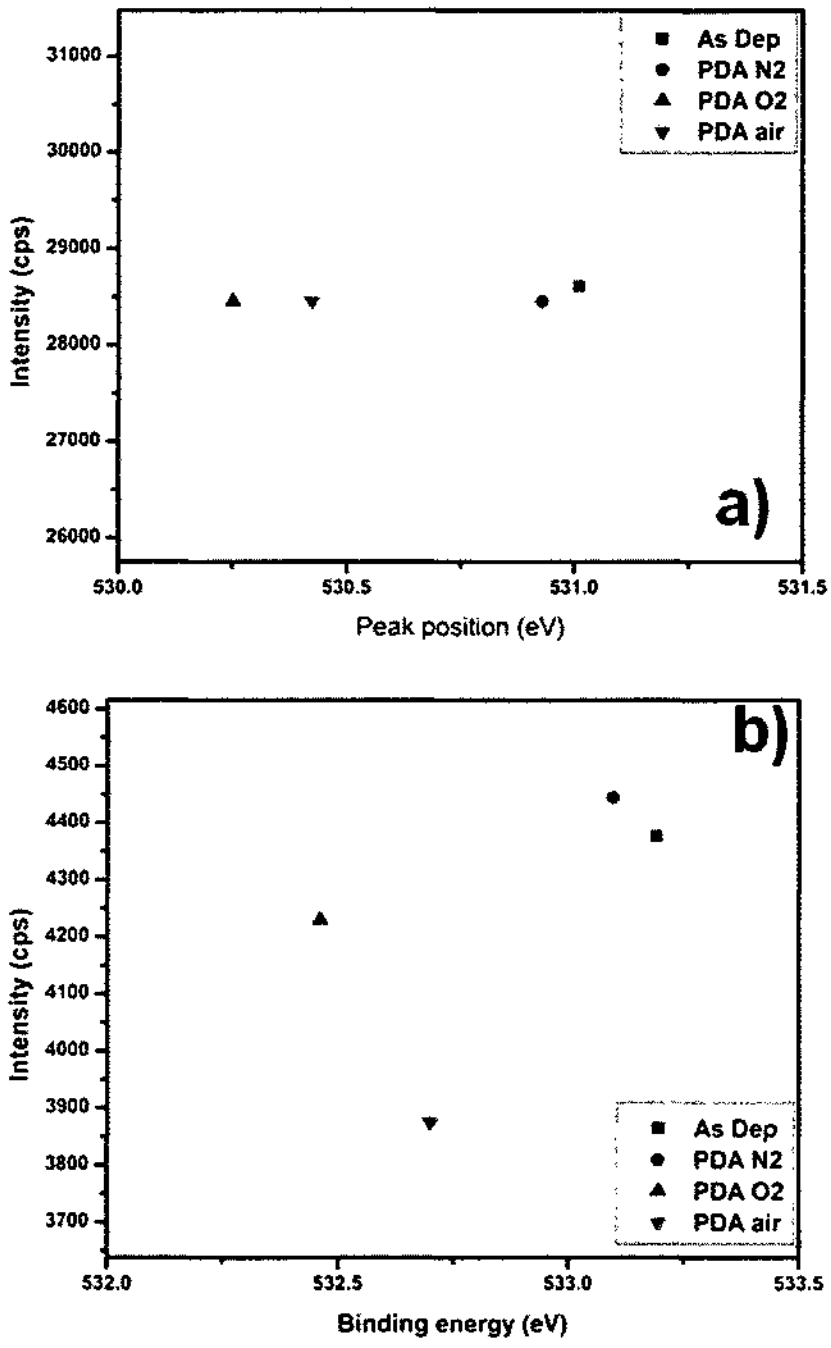

Figure 54. a) Shift in O1s peak position as a function of annealing environment. b) Shift of O peak in the oxygen deficient region.

Because the ALD synthesized ZnO thin films exhibit such a high electrical conductivity, the carrier type and density was further investigated. The as-deposited ALD ZnO thin film carrier concentration was measured by the Hall Effect. In order to suppress the effect of the Si substrate on the measurements, a thick electrically insulating oxide layer was grown and sandwiched between the ZnO layer and the Si substrate. Three sets of samples made of $ZnO/SiO_2/Si$, $ZnO/HfO_2/Si$ and ZnO/quarts were investigated. The $ZnO/SiO_2/Si$ set was made of an ALD ZnO layer on top of 150 *nm* PECVD SiO_2 grown on Si. Similarly, the $ZnO/HfO_2/Si$ was made of ALD ZnO on top of 150 *nm* of ALD grown on high-k insulating HfO_2 on Si. Finally, the third set was ALD ZnO on a quartz wafer. Hall measurements revealed an n-type carrier concentration in the order of $\sim 10^{19}$ cm^{-3} for all experiments compared to a concentration of 10^{15} cm^{-3} for bulk single crystal ZnO. These measurements reveal a significant difference in carrier concentration compound to bulk ZnO. The as-deposited ALD ZnO thin films, without any intentional doping, exhibit a native n-type high concentration. The carrier densities and mobility of the ALD ZnO films was measured as a function of thickness in Figure 55. A carrier concentration of 1.7×10^{19} cm^{-3} and a mobility of 24 $cm^2/V\text{-}s$ were observed for the 400nm as-deposited ALD ZnO; see Figure 55. Due to the high n-type concentration, the ALD ZnO shows relatively high electrical conductivity. The resistivity measurements from the Hall Effect agree well with the four-point probe measurements. An MOS structure was processed and fabricated to investigate the MOS behavior with ALD ZnO as the semiconducting layer. MOS capacitors with Au and Pt top metal electrodes were fabricated on the HfO_2/ALD ZnO structure. Figure 56 shows the C-V measurement of ALD 4 *nm* HfO_2 on ZnO with Au top electrodes at a frequency of 1 *MHz*.

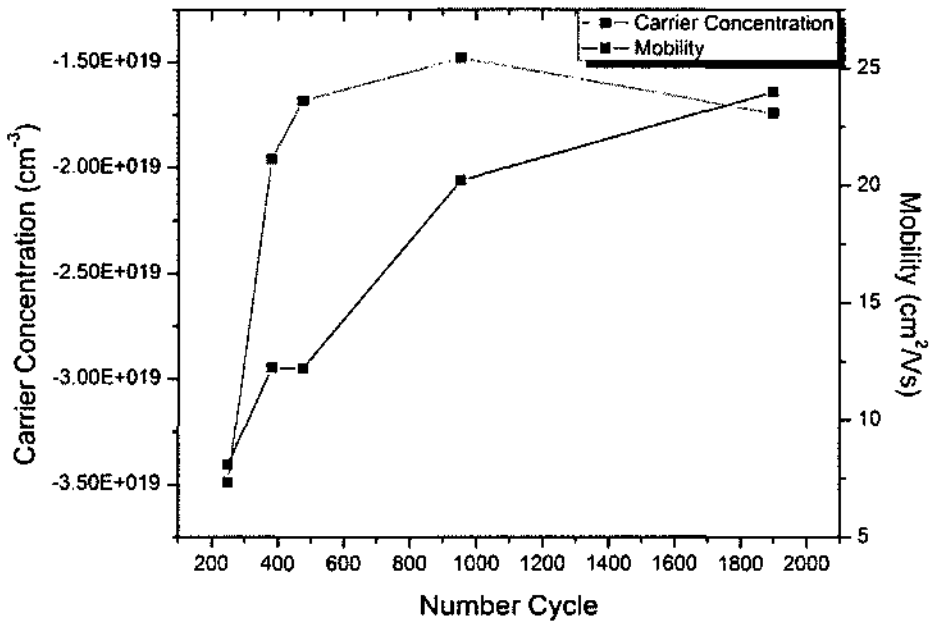

Figure 55. Carrier Density of ALD ZnO vs Number of ALD growth cycles.

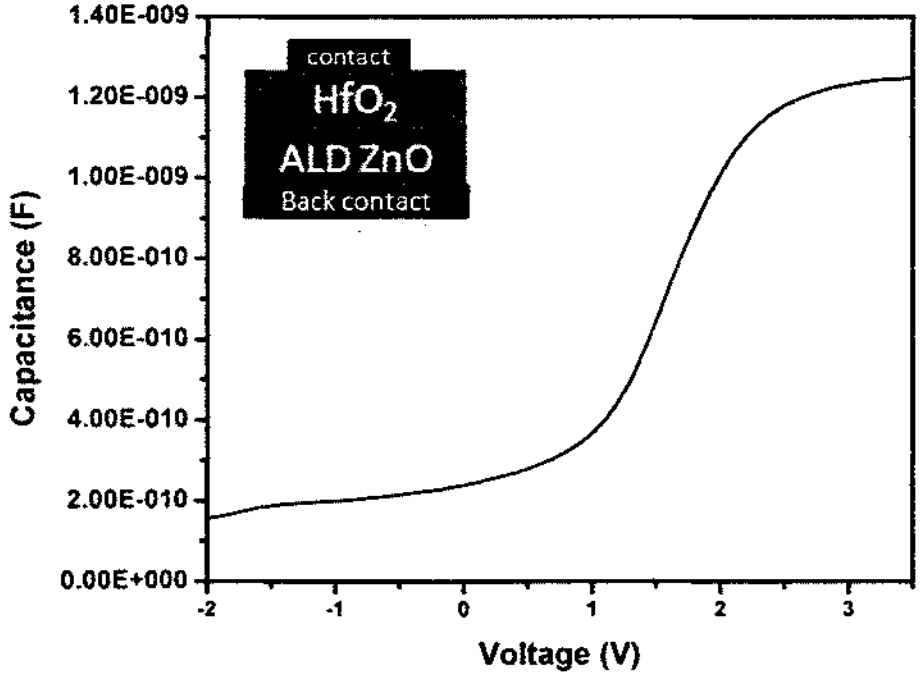

Figure 56. High frequency C-V measurements of ALD HfO_2 on bulk single crystal ZnO with Au electrodes capacitors.

The flat band voltage was calculated from the C-V curve in Figure 56 to be -0.5 *V*. The HfO_2 on ZnO dielectric constant was calculated using the following relation:

$$C = \frac{k\varepsilon_0 A}{d} \tag{32}$$

A dielectric constant of ~ 15 is obtained for the MOS structure using HfO_2 as the high-k layer and ZnO as the semiconductor layer. ZnO has potential applications in the electronics industry. Very good C-V plots can be obtained with ZnO in accumulation region with positive voltages and in inversion region with negative voltages, which is characteristic for n-type semiconductor materials; however, from the C-V plot, the deep inversion layer indicates the presence of trap levels in the ZnO film.

The charge trap levels in ZnO were investigated using deep level transient spectroscopy (DLTS). The DLTS measurements were taken using a Biorad DL4600 DLTS system. A sample of 400 nm ALD ZnO thin film was cleaned in acetone, isopropanol and rinsed in DI water. After cleaning, circular Au and Pt electrodes were deposited by e-beam evaporation. The thickness of the top metal electrodes deposited was ~100 nm, and the size of the electrodes ranged from 250 to 500 μm in diameter. A eutectic solution was used on the back of the samples as back contacts. The measurements were carried out using a rate window of 11.4 *Hz*. The time window is 204 ms. The bias voltage and the peak voltage were V_b = -1 *V* and V_p= 3 *V* respectively. The DLTS signal on the ALD ZnO was plotted as a function of temperature, as seen in Figure 57 a). The DLTS in the temperature range from 50K to 300K revealed one primary defect level. This defect level was found to have an activation energy of 0.23 *eV* below the conduction band. The capture cross-section σ and concentration were calculated to be equal to 4.43×10^{-21} cm^2 and 1.41×10^{15} cm^{-3} respectively. The Arrhenius plot of the

dominant defect is displayed in Figure 57. The capacitance of the diode under reverse bias of 3 *V* is equal to 35.53 *pF*. For comparison, the DLTS measurements on bulk ZnO in the literature indicate a common defect level with an activation energy between 0.2-03 *eV*. [76, 77] These defects are structural defects and are present in both single crystal and polycrystalline ZnO films, and they are generally thought to be due to oxygen vacancies (V_o) and Zn interstitials (Zn_i); however, Zn_i is believed to be a shallow donor in ZnO and V_o are deep donors. This is consistent with the local density approximation. The combined results of the XPS and the DLTS measurements of the ALD ZnO indicate that the presence of oxygen vacancies constitute the major defects level in the as deposited ZnO films.

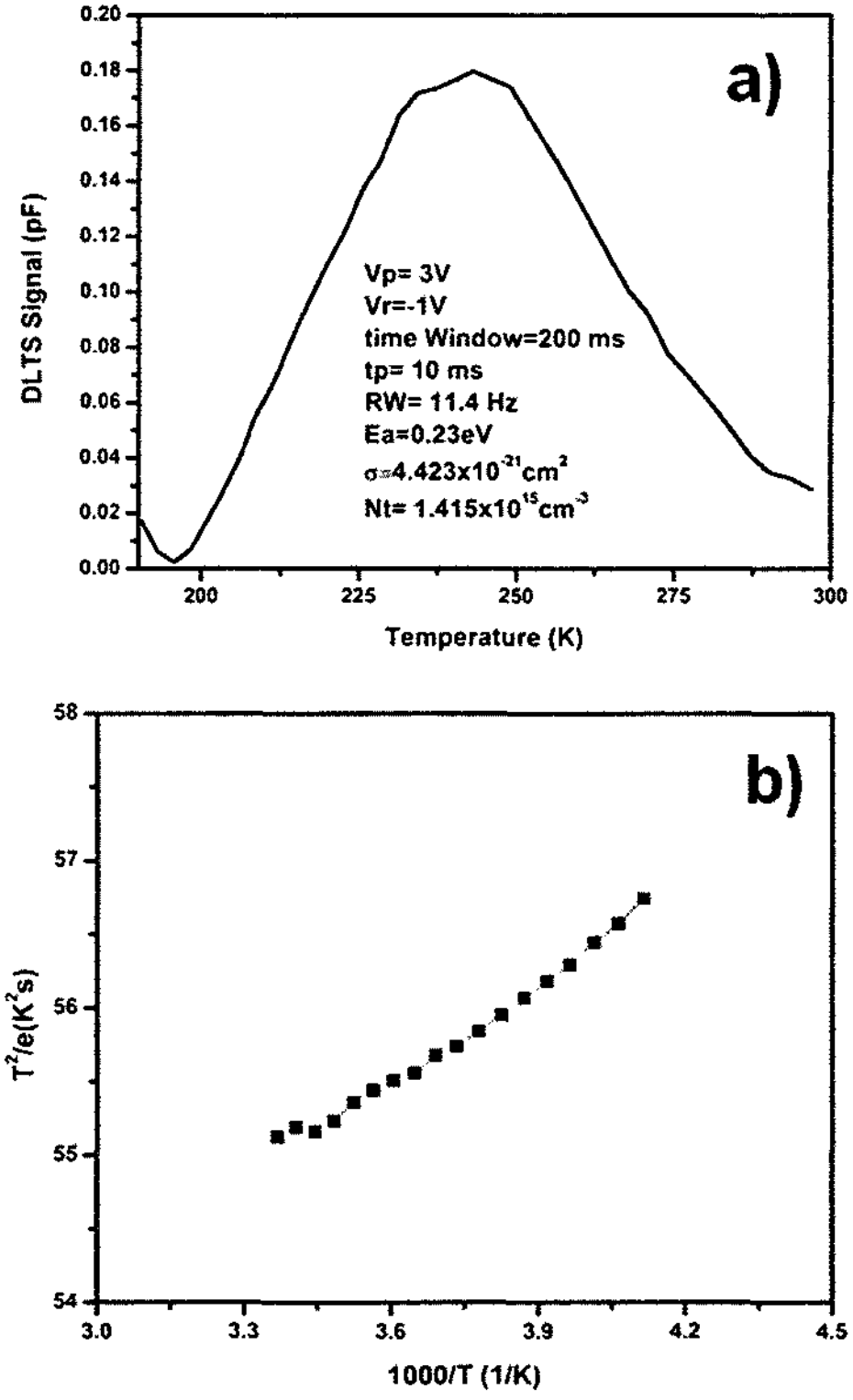

Figure 57. a) DLTS signal vs. temperature. b)Arrhenius plot of the primary defect in the 400 *nm* ALD ZnO thin films.

CHAPTER 5

ALD ZnO BASED PHOTODIODES

5.1 Introduction

Recently, ZnO photodiodes have attracted a lot of renewed interests. For photodiode device the ZnO layer is used as the photosensitive material. Among the semiconducting metal oxides that are being considered as candidates for the fabrication of photodiodes, ZnO offers specific advantages such as low deposition temperature, low cost and good electrical and optical properties. In addition, ZnO based photodetectors do not require anti reflection coatings.[78,79,80] Due to the lack of reproducible high quality p-type ZnO, because of the very high n-type background doping, good homojunction ZnO devices still remain an elusive goal. For the time being most heterojunction diodes have been fabricated as an alternative solution. The most common p-type semiconductors used are SiC, GaN, $ZnRh_2O_4$, NiO, Cu_2O and ZnMgO. Although the heterojunction devices based on these p-type materials exhibit good diode characteristics, they suffer from low spectral responsivity and hence low efficiency.[79] For example, n-ZnO/p-SiC samples have spectral responsivity around 0.045 *A/W* for energies greater than the bandgap $E_g \sim 3$ *eV*. [80] Heterojunction n-ZnO/p-Si devices have attracted significant attention. Those photodiodes can exhibit higher efficiencies and cover a wide spectral range. Quantum efficiency of ~50% or spectral responsivity of 0.28 *A/W* can be achieved with such photodiodes. [79] Si is the most studied element semiconductor and is relatively inexpensive.

In this chapter of the dissertation two terminal device applications for ZnO are explored, and heterojunction ALD n-ZnO/p-Si photodiodes are fabricated, characterized tested and optimized.

5.2 Experimental Set-up

ALD ZnO thin films were deposited on 4-inch diameter p-type Si (100) wafers at 150 ^{o}C to form a p-n heterojunction diode. DEZ was used as the precursor for zinc and H_2O vapor was used as the oxidation source. N_2 was used as the carrier gas. The ALD Chamber pressure reading was ~ $2.1x10^{-1}$ *Torr* in N_2 ambient. After the ALD deposition, the sample was subdivided by cleaving in multiple pieces. Surface cleaning can affect device performance particularly when depositing a thin film material. Therefore, one set of the samples was cleaned using O_2 plasma ashing for different times to investigate the effect of surface cleaning on the diode characteristics. Additionally, the choice of metal contact for the p-n heterojunction diode has a considerable impact on the device behavior. Moreover, the work function of the metal needs to be selected carefully while considering the doping concentration on the n-type material. Indeed, the work function of the metal contact with respect to the semiconductor work function and doping concentration determines whether the contact is Ohmic or a Schottky contact. Therefore, various metal contacts with different workfunctions were used to study both the contact resistance and the device performance. A Kurt Lesker PVD 250 electron-beam system was used to evaporate Ti, W, Al and Pt electrodes. These metals were used as top electrodes on the photodiode samples that were treated with O_2 plasma ashing and diode samples that did not receive O_2 plasma pre-treatment. The deposition parameters for the metals are summarized in Table 11.

Table 11. E-beam deposition parameters for metal contacts.

Metal	Starting Pressure (*Torr*)	Density (g/cm^3)	Z ratio	Deposition rate (*Å/s*)	Thickness (*nm*)
Ti	1.5×10^{-7}	4.5	0.628	4	100
W	5.3×10^{-6}	19.3	0.163	1	100
Pt	5.3×10^{-6}	21.4	0.245	2	100
Al	5.3×10^{-6}	2.73	1.08	1	100

The electrical properties of the ZnO/Si photodiodes were studied using different characterization techniques. The photodiodes I-V characteristics were measured using a semiconductor device analyzer B1500A by Agilent connected to a Micromanipulator probe station. The B1500A has a current resolution of 0.1 *fA* and a voltage resolution of 0.5 μV. Both the dark current and the photocurrent were collected using I-V measurements. The voltage was swept from -4 *V* to 4 *V* and 4 *V* to -4 *V* with 0.08 *V* step and 0.1 *V* compliance. The quantum efficiency (QE) experiments were performed on a PV-Measurements system (IVQE-8C), at 0 volt bias, under AM1.5G illumination, with a Xenon Arc lamp source as primary source and dual-grating monochromator. The incident power was 100 mW/cm^2. The QE measurements evaluate the current or e/h pairs collected by light absorption of the sample versus the known intensity of light irradiated on the photodiode sample. For optimum device performance, the design of the p and n regions is critical. The thickness and doping concentration of the n-type ZnO layer is thus very important. The thickness of the top layer affects both the absorption efficiency of the

photodiode, as well as the amplitude of the total current collected. The photoactive semiconductor film has to be thin enough to allow carrier collection at the contact side and therefore enable diffusion of carriers with minimum recombination. The films should also be thick enough to absorb a greater light intensity (more photons) under illumination. Thus, the ZnO layer thickness has to be optimized to increase the collected current and to optimize absorption efficiently. The recombination rate is inversely proportional to the carrier lifetime which is in turn proportional to the square of the carrier diffusion length. Thus, the n-type layer thickness needs to be designed with consideration of the carrier diffusion length. The calculation of the carrier diffusion length can be found in Appendix A. The carrier diffusion length in ZnO was calculated to ideally be 364 *nm*. A 400 *nm* ALD ZnO thin film was deposited on Si to take into account both the diffusion length and the absorption efficiency for diode characteristics optimization. Additionally, the full stoichiometry of ZnO deposited by ALD is ideally obtained at a film thickness of 400 *nm*.

5.3 Energy band diagram of ALD n-ZnO/p-Si structures

One of the most important properties of a p-n heterojunction diode is its current-voltage behavior or rectifying characteristic. Current flows in one direction under forward bias applied voltage and almost no current in the other direction. Under forward bias, the diode current flow increases exponentially with voltage. The voltage at which the current starts increasing is known as the turn-on voltage. Ideally, under reverse bias no current flows. However, as the reverse bias is increased the diode finally starts conducting after a certain voltage. The point at which current flow is detected under reverse bias is known as the breakdown voltage. The forward bias is defined as a positive voltage applied on the p-side of the p-n junction and a negative voltage applied on the n-side. On the other hand,

the reverse bias is defined as a negative voltage applied on the p-side and a positive voltage on the n-side. In order to optimize the ALD ZnO based heterojunction photodiodes, the energy band alignments have to be studied since the conduction and valence bands offsets affect the diode characteristics such as turn on voltage, breakdown voltage, depletion width, band offsets and carrier diffusion length and thus the current. The energy bands of the heterojunction were accurately determined by high resolution XPS analysis. Figure 58 shows the separated energy bands of both semiconductors with respect to the vacuum level prior to the formation of the p-n heterojunction. The Fermi level of ZnO and that of Si are also drawn. It is important to notice the misalignment of the two Fermi levels since that energy level difference is responsible for the bending of the conduction and valence bands, the diffusion of carriers, the depletion width, etc. The electron affinity of the semiconductors, which is defined as the separation between the vacuum level and the conduction energy level, and the difference between the conduction band and Fermi level determine the conduction band and valence bend shift that is required to align the Fermi levels of the two semiconductors at equilibrium. The Fermi level of n-type ZnO is above its conduction band, meaning that the semiconductor is degenerate. However, the Fermi level of p-type Si is above and closer to the valence band since the material is lightly p-doped with boron acceptor atoms. Moreover, it can be observed that the conduction band and valence band energy levels of the two materials are not aligned when separate.

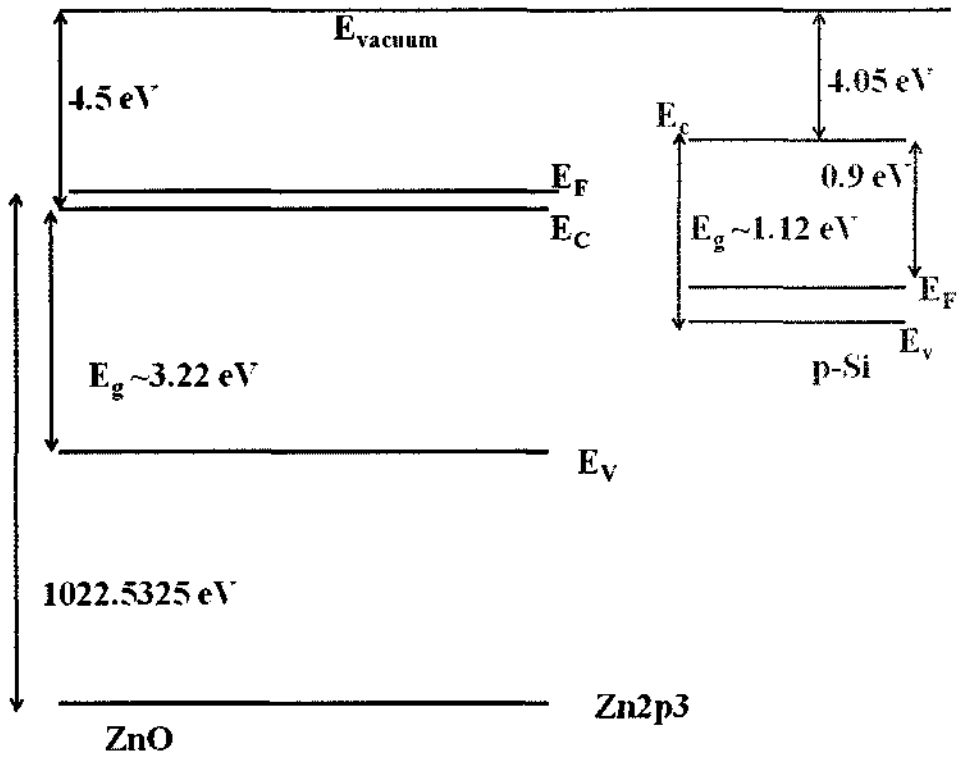

Figure 58. Energy bands of ALD ZnO and Si with respect of the vacuum level

Simulations using ADEPT semiconductor simulator were performed and compared with the calculated values. Theoretical detailed calculations were performed to verify the accuracy of the simulation results. Appendix A shows the calculations. The material properties used in the simulation and the simulation code are shown in Appendix B and C respectively. The simulated band diagram is shown in Figure 59 under different bias conditions. As expected, at equilibrium the Fermi levels of the ZnO, E_{FN}, and that of Si, E_{FP} align when the p-n heterojunction forms; thus, the conduction and valence bands will bend accordingly. At equilibrium, in order to maintain the condition of charge neutrality, the Fermi levels must be constant. The simulated band diagram under zero bias is shown in Figure 59a. The simulated valence and conduction band offsets are 0.45

eV and 2.6 eV respectively. These values are very comparable to the independently calculated values of 0.45 eV and 2.5 eV. The band offsets originate from the difference of workfunctions of both semiconductors. It is a measure of the energy required to reduce the barrier seen by carriers and for the current to flow. In other words, this energy barrier is known as the built-in voltage for a heterojunction. The higher the band offsets, the larger the built-in voltage and the higher the voltage required to turn the device on. The built-in voltage was calculated to be ~ 0.6 V.

After the formation of the heterojunction, carrier diffusion takes place to maintain equilibrium state. Because of the large concentration difference in carriers, the electrons from the n-side diffuse into the p-side and the holes from the p-side are drawn by diffusion to the n-side. This inter-diffusion leaves a depletion region near the junctions which becomes depleted of carriers. As a consequence, space charge region is developed with positively charge donor ions on the n-side and negatively charge acceptor ions on the p-side. This space charge creates an electric field in the depletion region which drives a drift current. The electric field drives the holes in the same direction as the field and the electrons in the opposite direction of the field which opposes the diffusion current until an equilibrium is established. The simulated and calculated depletion widths are 0.27 μm and 0.23 μm respectively. In an abrupt p-n junction, the depletion region extends asymmetrically further into the material with the lowest doping level. The total current is the sum of the drift current due to E-field and the diffusion current.

Figure 59b-d shows the band alignment of the heterojunction n-ZnO/p-Si under different biasing conditions. It can be seen that the conduction band offset is reduced by the action of the forward biasing voltage and the band offset is increased by applying a

reversed bias. The depletion region is reduced under forward bias and the band offsets is also reduced. This facilitates the current flow. Under the forward bias conditions, the diffusion current dominates over the drift current. Under reverse bias conditions, the depletion width and the energy barrier are both increased. Consequently, the drift current becomes greater than the diffusion current. The effect of the biasing conditions is depicted in Figure 59. The electric field and the total charge density were also simulated in Figure 60. The p-n junction behaves like an abrupt junction with most of the depletion region in the Si p-type layer since it is much more lightly doped compared to the ALD ZnO layer. Figure 60a shows the electron and hole densities in the quasi-neutral region. It can be seen that the carriers are depleted from a region at the metallurgical junction from ~0.4 μm to ~0.6 μm. Figure 60b-d show the total charge density in the depletion region, the electric field and recombination rate which mostly is dependent on the carrier lifetime. The discrepancy between the calculated depletion region and the simulated depletion region is attributed to how the simulator treats the presence of the abrupt junction difference in velocity and lifetime of the electrons and holes in ZnO and Si. This is not taken into account by the theoretical calculation. Overall, the simulation data agree well with theoretical values.

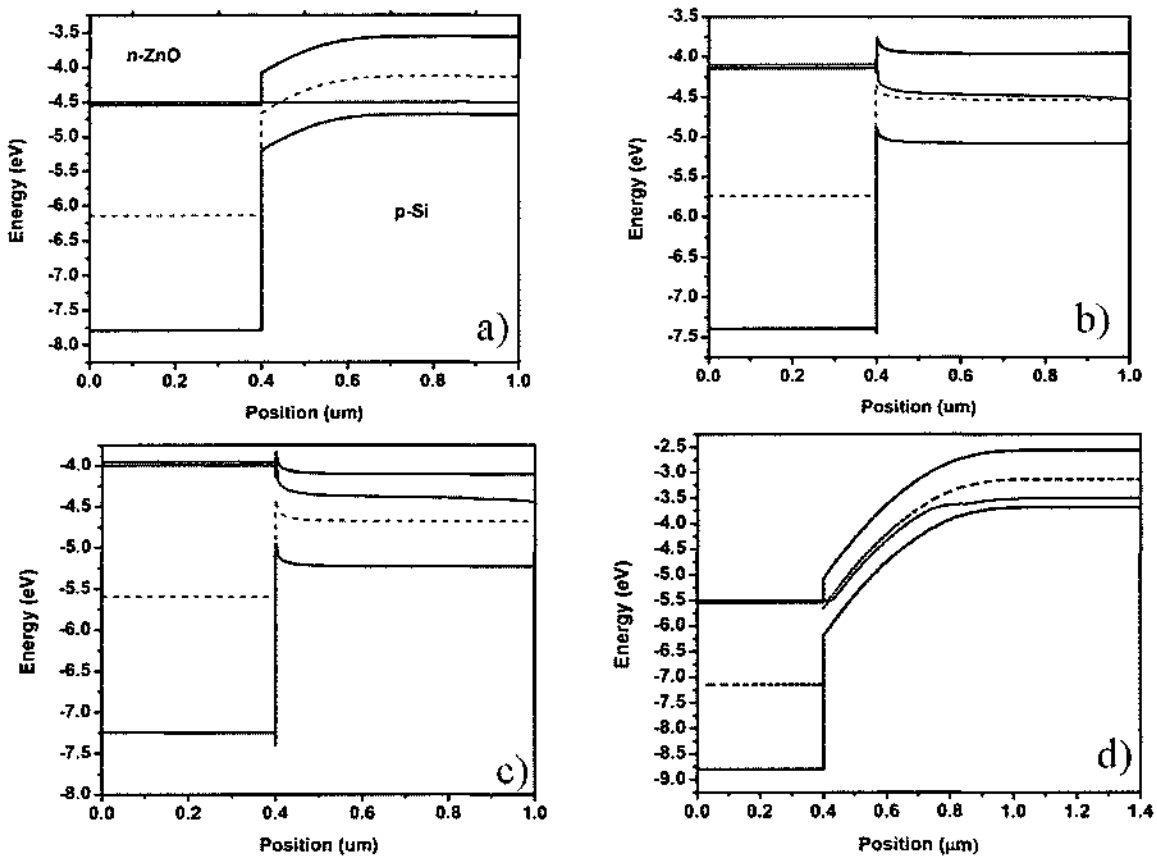

Figure 59. Simulated energy bands at n-ZnO/p-Si heterojunction. a)Energy bands V_{bias}=0 *V* b) V_{bias}=0.8 *V* c) V_{bias} =1.1 *V* d) V_{bias} = -2 *V*. (red) Fermi level, (dashed) intrinsic Fermi level, (black) conduction and valence bands.

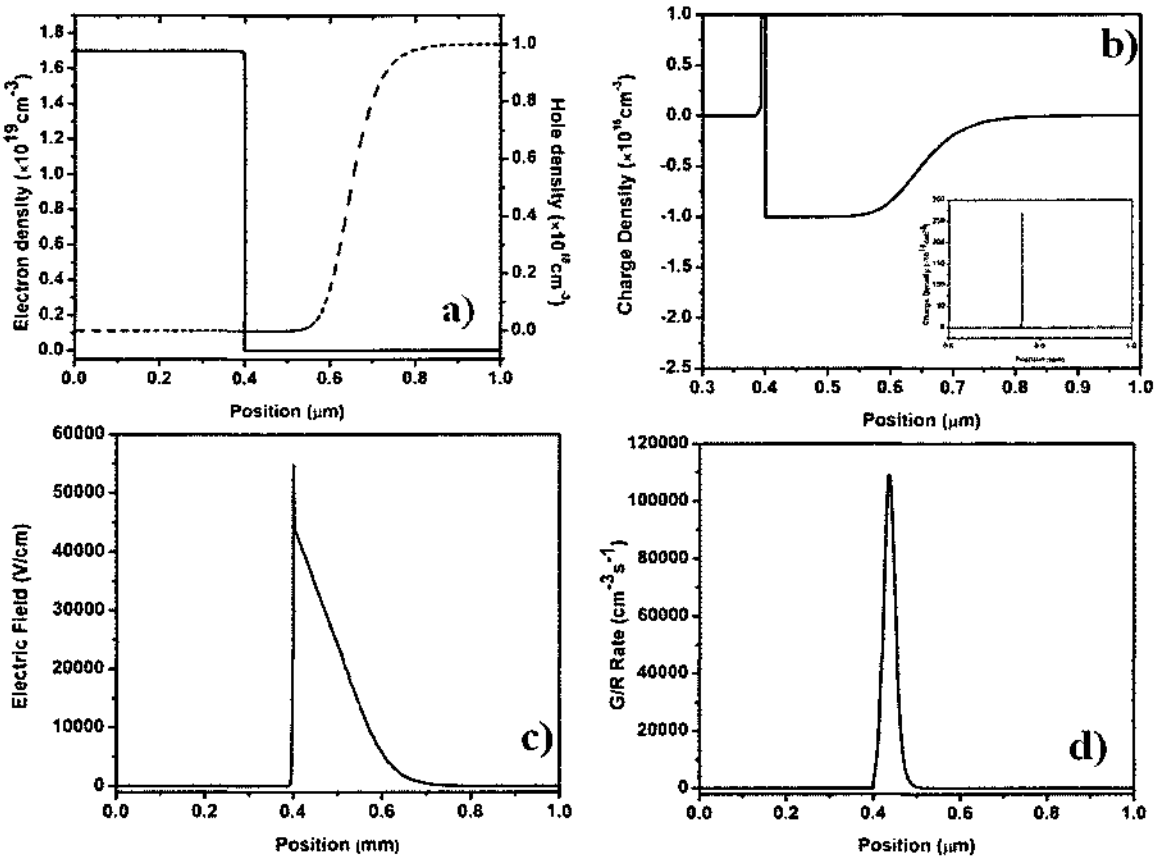

Figure 60. a) Electron and hole density of n-ZnO/p-Si heterojunction in the quasi-neutral region. b) Total charge density as a function of depth in the depletion region c) Electric field as a function of depth. d) Recombination and generation rate.

5.4 Quantum efficiency

Quantum efficiency (QE) is one of the most important properties for photosensitive devices such as photodiodes and solar cells. It measures the number of electron-hole pairs generated under incident light. The QE of a diode can be expressed as follows:

$$QE = \frac{Rhc}{q\lambda} \tag{33}$$

where h= Planck's constant, c=speed of light, q= electron charge, λ=wavelength of the incident light and R= responsivity is described in equation $R = \frac{I_p}{P}$ (A/W) **(3)**.

The quantum efficiency measurements of the fabricated ZnO/Si photodiodes cover a wide spectral range. For the ZnO/Si heterojunction photon energies covering the visible and near-infrared range are attributed to processes in the Si because those energies are smaller than the bandgap of ZnO. Therefore they cannot be absorbed by the ZnO material. That is the reason why knowledge of the band structures of the materials is critical in designing an efficient photodiode. The bandgap of ZnO is 3.2 *eV;* thus, the material will only absorb photon with energy greater than its energy band gap. Thus, shorter wavelengths, as seen in Figure 58 and Figure 59, will be absorbed by the ALD ZnO material. By depositing a ZnO layer on Si, the spectral responsivity of Si photodetectors is widened down to UV range. To achieve an efficient UV photodetector, the ZnO layer must be the active layer where the detection occurs. The photodiode device structure is shown in Figure 61. Each electrode was isolated from its neighbor to limit the effect from the surrounding electrodes. Therefore, the efficiency measurement is obtained from the ZnO region which is irradiated and where the light is absorbed. The measurements were conducted under 0 V bias and measuring the QE was measured when the sample is under radiation from UV (300 *nm*) to infrared (1300 *nm*).

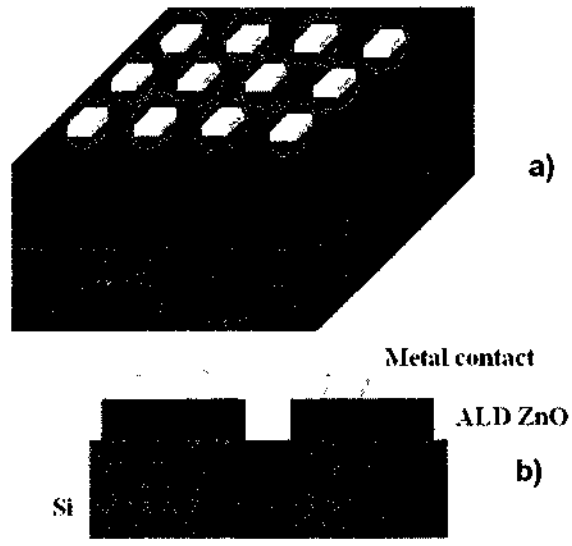

Figure 61. Schematic of photodiode device structure for QE measurement. a) Side view b) cross-sectional view

Figure 62 shows the QE measurements for Al/ZnO/Si and Pt/ZnO/Si heterojunctions with two different metal contacts. The simulation is shown in Figure 59. The bandgap of Si is 1.1 *eV*, thus Si will absorb photon energies large than 1.1 *eV*. Si absorption quantifies the QE response in the visible range (400 *nm* - 800 *nm*) and also in the near-infrared to infrared range since Si absorbs photons with wavelength smaller than 1.12 μm. The measurements revealed a QE of 38.48 % for Al/ZnO/Si photodiodes and 41.83 % for Pt/ZnO/Si photodiodes for the as-deposited ALD ZnO samples at a wavelength on 380 nm which matches exactly the band edge of our ALD ZnO films. This can also be seen in Figure 62. The peaks from Figure 62 around 470 *nm* and 630 *nm* are most likely due to interference fringes. Optical reflection, carrier recombination, fringes from interface layer and defects, all affect the quantum efficiency. For the case of ALD

ZnO/Si photodiodes, there is the presence of a thin layer of non-stoichiometric SiO_x. The thin layer of the oxide is originating from the deposition process due to H_2O precursor used as oxidation source. The native oxide can be detected by TEM analysis in Figure 63. In this case, the interference fringes add up constructively resulting in the spectra seen in the visible range. Additionally, the ZnO crystal structure is hexagonal and, thus, has two essential lattice constants 3.2 Å on the a-axis and 5.2 Å on the c-axis. In ALD grown ZnO, the c-axis is dominant; thus, the lattice constant is 5.2 Å, which represents a 4 % mismatch with Si lattice constant of 5.43 Å. Thus, the ZnO lattice is under tensile strain up to its critical thickness after which it relaxes by releasing defects. The critical thickness h_c of ALD ZnO on Si can be calculated as follows:

$$h_C = \frac{b(1-\nu\cos^2(\alpha))(\ln(h_c/b)+1)}{8\pi f(1+\upsilon)\cos(\lambda)} \qquad (34)$$

where ν = is the Poisson ratio of ALD ZnO obtained from the nanoindentation experiment and is depending on the Young's modulus, b= Burgers vector $=a_{Zno}/2$ <110>, f=misfit parameter= $f = \frac{a_{ZnO} - a_{Si}}{a_{Si}}$, α and λ are the angle between the Burgers vector and slip direction and the slip plane and the interface respectively.

After solving the equation, the critical thickness upon which the relaxation introduces dislocations near the interface was calculated to be ~ 1 *nm*. The grown ALD films are much thicker than the critical thickness therefore a dislocations are expected as seen in the TEM cross-section in Figure 63.

Despite the defects from the lattice relaxation, the efficiency of the device measured is significant and encouraging. Further device improvements can be achieved by dealing with the defect density levels. Because surface structures heavily impact the

QE measurements the samples were cleaned by an O_2 plasma treatment for 5, 10, 15 and 30 *min*. The plasma power was set at 20 *W* and a pressure of 50×10^{-3} Torr. The oxygen flow was set to 15 *sccm*. The QE was found to increase after O_2 plasma cleaning to approximately 49.05 % and 52 % for Pt and Al respectively.

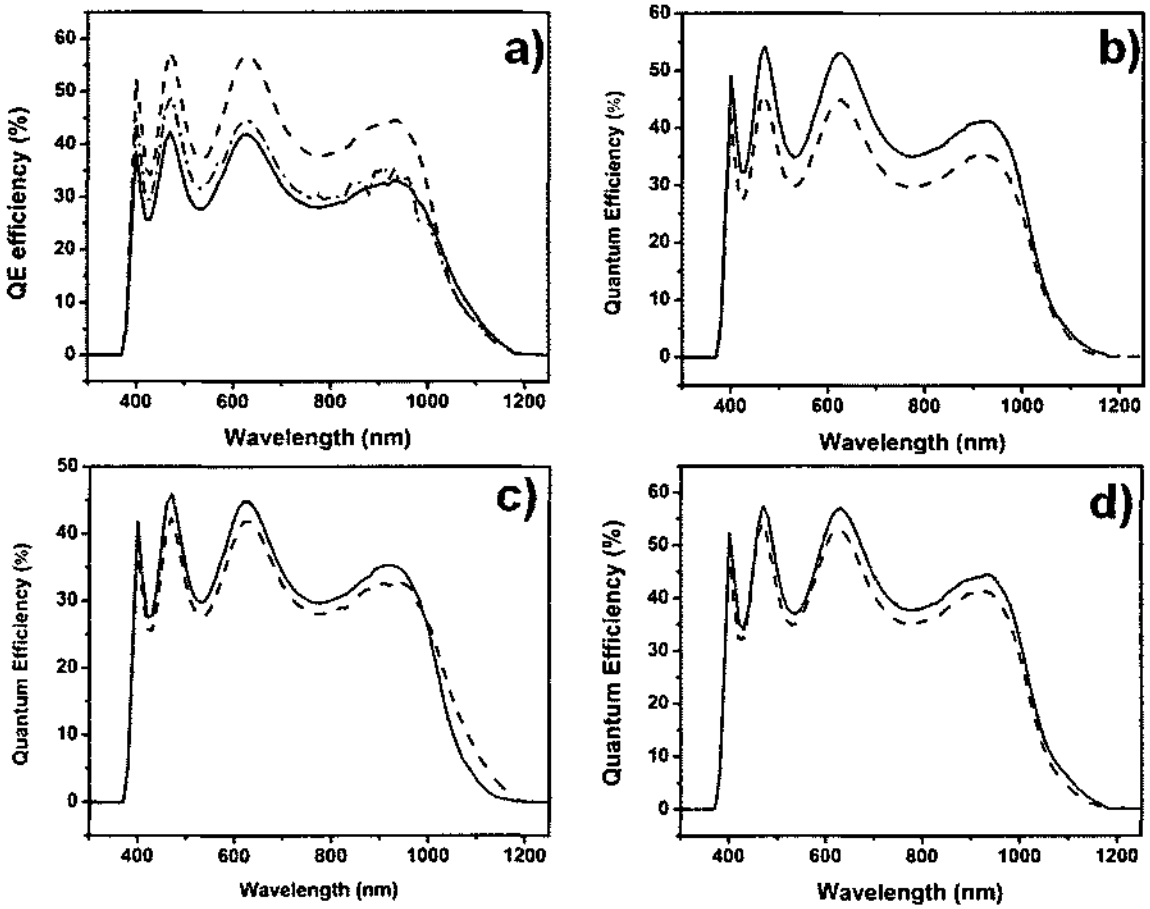

Figure 62. Quantum efficiency of ALD ZnO/Si photodiodes. a) QE using an Al electrode. (solid line) non cleaned sample, (dash-dot) after 15 minutes O_2 plasma clean, (dash) after 30 minutes O_2 plasma clean. b) QE of a Pt/ZnO/Si photodiode. (dash) non clean, (solid line) 30 minutes O_2 plasma clean. c) Comparison of Al/ZnO/Si and Pt/ZnO/Si

photodiodes not cleaned, d) Comparison of Al/ZnO/Si and Pt/ZnO/Si photodiodes after 30 minutes O_2 plasma clean.

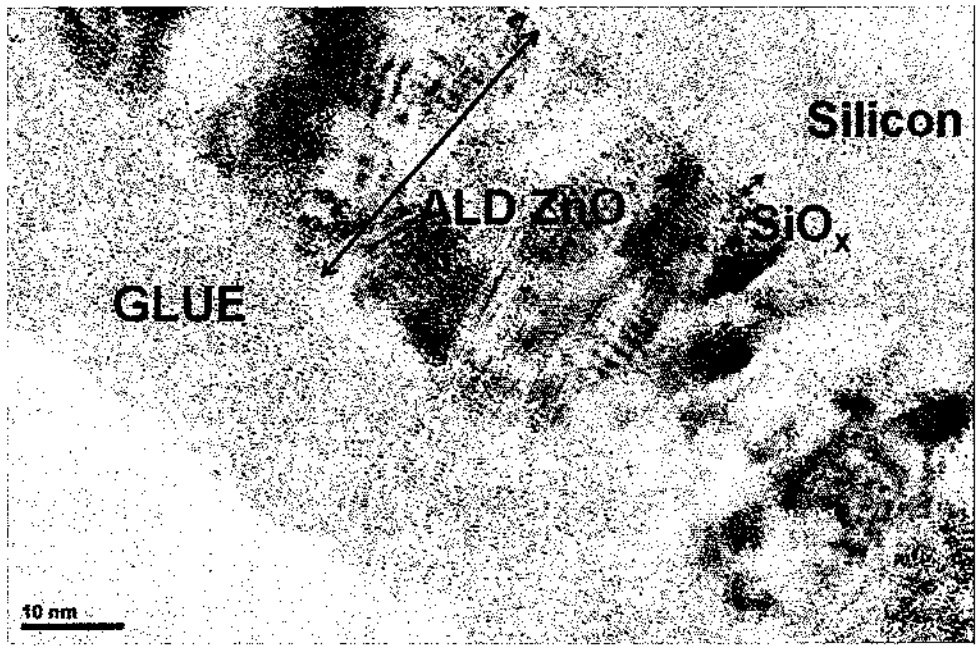

Figure 63. TEM showing thin oxide layer on Si responsible for interference fringes.

5.5 I-V Characteristics of n-ZnO/p-Si Photodiodes

In order to gain a better understanding of the QE measurements, the energy bands diagrams were simulated. The workfunctions of Pt and Al are 5.6 *eV* and 4.05 *eV* respectively. From our previous calculations the workfunction and electron affinity of ZnO are 4.45 *eV* and 4.5 *eV* respectively. A Schottky contact is defined as a metal junction contact where the metal work function is larger than that of the semiconductor workfunction. However, even when the metal work function is larger than that of the

semiconductor, a metal junction contact can behave as an Ohmic contact depending on the doping concentration of the semiconductor and on the interface defect density. When a metal-semiconductor junction is created, a depletion region is created underneath the metal. At thermodynamic equilibrium, electrons flow from the semiconductor to the metal in Schottky contacts. This flow causes a depletion region to form at the semiconductor-metal interface. Also, the potential barrier height, due to the work function difference between the semiconductor and the metal, prevents electrons from crossing from the metal side to semiconductor. Current flow occurs for forward bias and very little current flows in reverse bias. This results in a rectifying behavior for Schottky contacts. However, if the doping concentration in the semiconductor is very high, the depletion width in the semiconductor underneath the metal is reduced, allowing the electrons to tunnel through the barrier more readily and rendering the contact a virtual Ohmic contact. On the other hand, an Ohmic contact occurs when the work function of the metal is lower than that of the semiconductor. For Ohmic contacts, the contact resistance is as low as possible and follows Ohm's law V=IR. Pt metal, having a higher workfunction than the workfunction of ZnO, is expected to form a Schottky contact with ZnO. On the other hand, the Al workfunction is lower than that of ZnO; therefore Al is expected to form an Ohmic metal contact with ZnO. The ideal barrier height for Al and Pt with ALD ZnO are -0.405 eV and 1.2 eV respectively, see Appendix A for the calculation. Figure 64 shows the band alignment simulation of different metal contacts with ZnO/Si p-n heterojunctions and their potential barrier heights. The barrier height and depletion region of the metal/ZnO/Si photodiode are calculated as follows:

$$q\phi_b = qVi + E_{FN} = q\phi_{metal} - q\phi_{ZnO} + E_{FN} \tag{35}$$

$$W = \sqrt{\frac{2\varepsilon_{ZnO}}{qN_d} V_i} \tag{36}$$

The calculated depletion width of the metal electrodes on Si is shown in Table 12. It must be noted that the potential barrier is reduced when the bias voltage applied. Also, the barrier seen by the electrons from the semiconductor side might be smaller if interface states exist with levels higher than the conduction band minima.

Table 12. Workfunction, barrier height and depletion width of metals on ZnO/Si photodiodes

Metal	*W*	*Ti*	*Pt*	*Al*
Workfunction (*eV*)	4.55	4.33	5.6	4.05
Φ_b (*eV*)	0.145	-0.075	1.195	-0.355
W (*nm*)	2.36	2.59	8.01	4.72

The current-voltage measurements of the fabricated n-ZnO/p-Si photodiodes using Al, Pt metal electrodes are shown in Figure 65 as well as two other metals with workfunctions between those of Pt and Al. Ti and W were chosen because of their work functions of 4.33 *eV* and 4.55 *eV* respectively. The dark current measurements are shown in Figure 65a. A very good rectifying characteristic can be detected with Al, Pt, and W metal electrodes. Nevertheless, Ti electrodes show a deviation from the ideal diode

characteristics. Figure 65b shows the photogenerated current. One of the causes of the observed behavior of the I-V curves is the high ideality factor n. The ideality factor is heavily impacted by defect levels, surface conductivity and interface layers.

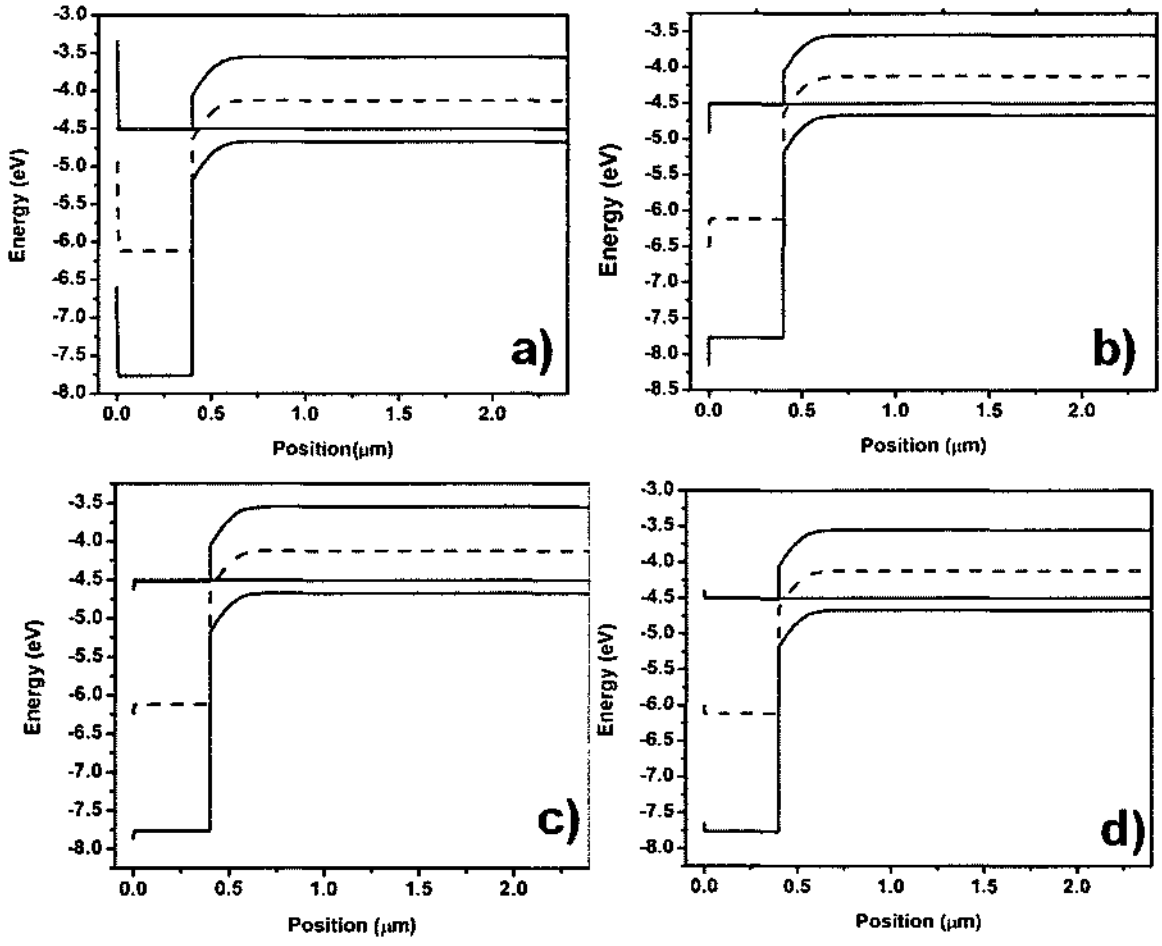

Figure 64. Band diagrams with metal electrode. a) Pt contact b) Al contact c) Ti contact d) W contact on n-ZnO/p-Si heterojunctions.

In fact, interface states created from the dangling bonds and impurities at the surface act as recombination centers and thus affect the electrical properties. Cleaning and surface preparation can reduce the surface conductivity, and surface recombination velocity. After O_2 plasma cleaning, the contact between the metal and ZnO improved considerably.

It can be seen from Figure 66 that the longer the O_2 plasma cleaning time lasts, the better the rectifying characteristics get and the smaller is the reverse bias current of the diode. This effect was consistent with all the different four metal types investigated. The O_2 plasma clean was performed as a surface preparation before the contact deposition. Since oxygen ions are bombarded on the substrate, the dangling bonds at the surface of ZnO are passivation. Thus, some of the surface defects and impurities on ZnO are eliminated by the cleaning step, which in turn improves the device characteristics. The turn-on voltages V_t and short circuit current as a function of cleaning are shown in Table 13. The short circuit current for dark measurements is the saturation current of the diode when the applied voltage is 0 *V*. The open circuit voltage is the voltage when the diode current is 0 *A* and is obtained graphically by extrapolation of the tangent to the I-V curve in the region of current flow. It can be seen from Table 13 that the reverse saturation current is reduced and the turn on voltage is improved with the O_2 plasma cleaning time for all metals. The saturation current of Pt contacts decreased from 0.00235 A/cm^2 to 0.00043 A/cm^2 after cleaning in O_2 plasma for 15 minutes. This explains the improvement in quantum efficiency of the UV ALD ZnO/Si photodetectors from 41 % to 49 % after surface cleaning in O_2 plasma. From the XPS studies, the ALD ZnO thin films were found to be terminated by adsorbed OH groups on the surface. The O_2 plasma

treatment removes those OH groups and saturates those dangling bonds and decreases the surface states, hence the recombination centers are decreased. As a result a sharper interface is created between the metal and the active layer ALD ZnO. The surface preparation also impacts the diode ideality factor n. As explained previously, n is strongly dependent on the doping concentration, defect density, interface states and surface recombination. Surface treatments reduce those defects; hence, the ideality factor improves.

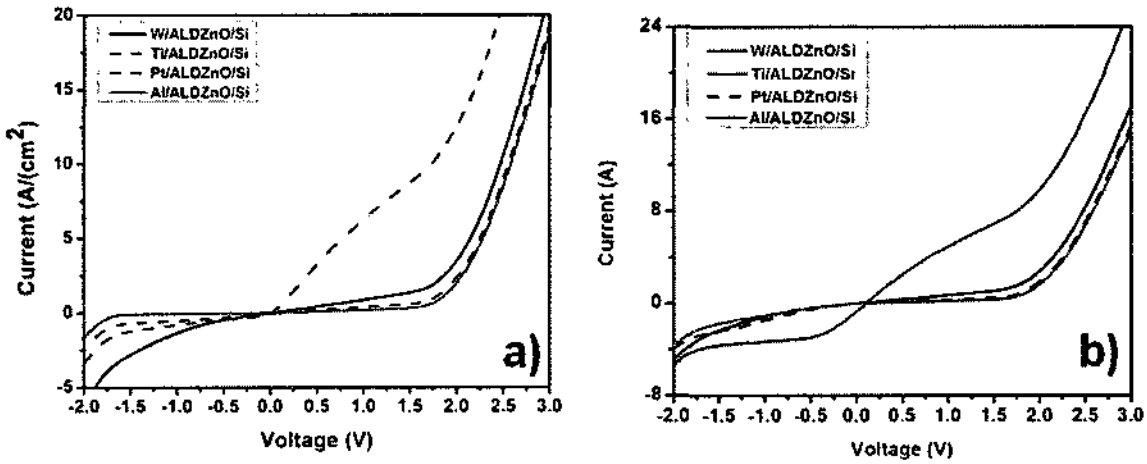

Figure 65. a) Dark I-V curve of metal/ZnO/Si with no surface cleaning. b) I-V curve under light source. Metals = W, Ti, Pt, and Al.

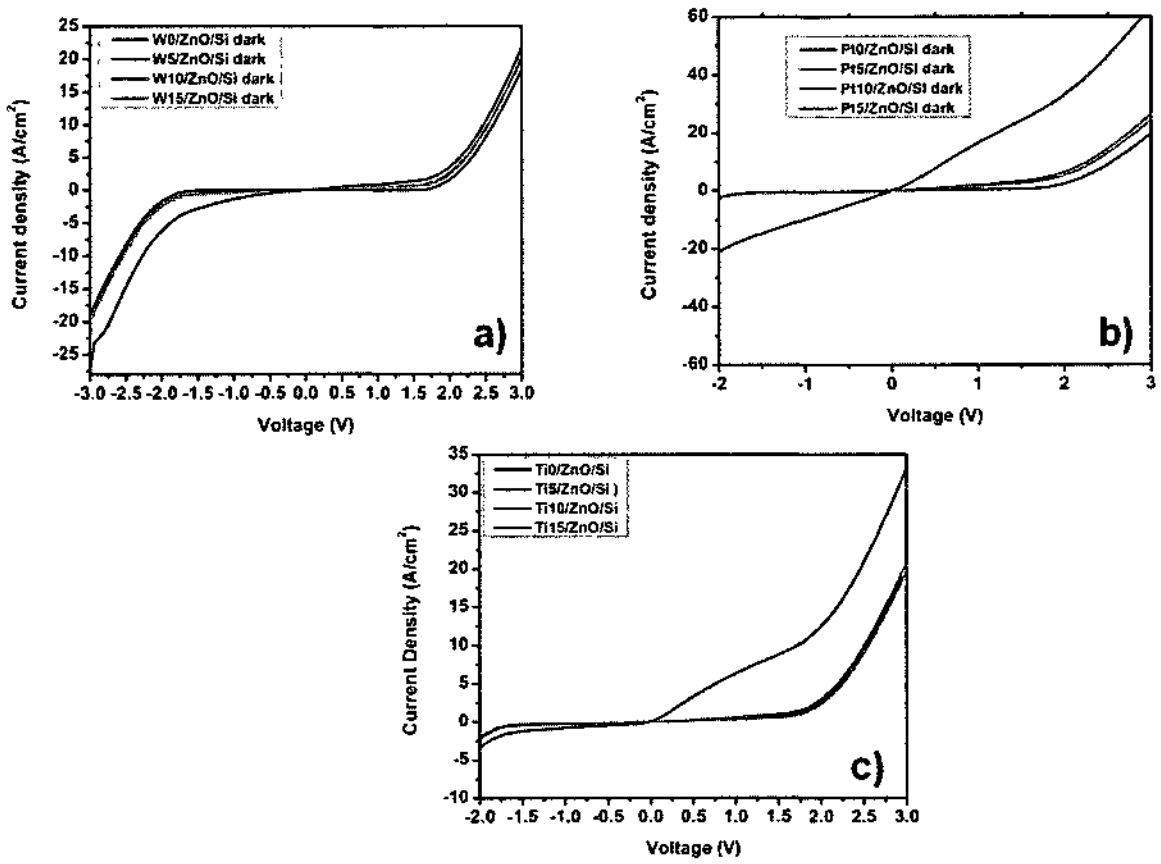

Figure 66. I-V characteristics of ZnO/Si photodiodes showing the effect of the surface cleaning. Sample were cleaned for 5, 10, 15 minutes in O_2 plasma.

Table 13. Summary of short circuit and open voltage of metal/ZnO/Si diode. Metals = W, Ti, Pt, Al

Metals electrodes	J_{sc} dark (A/cm^2)	V_t dark (V)	R_s (Ω/cm^2)	R_{sh} $(\times 10^5\ \Omega)$	J_{sc} Light (A/cm^2)	V_t (V) Light
W0	0.0002	2	0.051670947	5.982531009	0.03529	2.08
Ti0	0.00041	1.51	0.091162	3.006012	0.87012	1.7
Pt0	0.00235	2.09	0.054373735	0.519390582	0.04275232	2.07
Al	0.01149	2.1	0.055051	0.106358	0.0439	2.1
W5	0.0037	2.1	0.0535636	0.3298334	0.01645	2.1
Ti5	0.00204	2.1	0.053890244	0.599940006	0.06081	2.1
Pt5	0.00036	1.88	0.047010638	3.357582541	0.38087	1.95
W10	4.3×10^{-6}	2.11	0.0552375	283.99678	0.00017	2.11
Ti10	0.00245	2.1	0.055936709	0.498090652	0.0301	2.09
Pt10	0.00243	1.2	0.062783607	0.502638854	0.95181	1.2
W15	0.00029	2.11	0.0535636	4.1823505	0.04358	2.09
T15	0.0018	2.1	0.052607143	0.680735194	0.07872	2.1
Pt15	0.00043	1.95	0.0491	2.860684657	0.32183	1.95

A small voltage drop across the metal electrode is expected due to the metal finite resistivity. The DLTS measurements revealed the presence of deep level defects with a defect density $\sim 10^{15}\ cm^{-3}$. These defect levels act as recombination sites, known as Shockley Read Hall recombination sites. Therefore, the recombination current is

increased by the presence of defect in the active region. As a result, the total dark current of the photodiode is dependent not only on the diffusion current but also the recombination and the parasitic effect of the series and shunt contact.

The series resistance R_s is obtained from the slope of the I-V curve at I=0 and R_{sh} is obtained from the slope of the I-V at V=0 *V*. Ideally, R_s is 0 and R_{sh} is ∞. However, in practice they differ from their ideal values. R_s should be as small as possible and R_{sh} should be as large as possible in the order of $M\Omega$. R_s affects the open-circuit voltage and R_{sh} affects the short-circuit current. This effect can be discerned from Table 13. For example, the reverse saturation current of the as deposited W metal contacts is ~0.0002 A/cm^2 and the R_{sh} is ~6×10^5 Ω. Following a 10 minutes cleaning in O_2 plasma, the saturation current was improved to 4.3 $\mu A/cm^2$ and the R_{sh} increased to 2.83×10^7 Ω.

The ideal current equation can be re-written in terms of diffusion current, recombination current and parasitic effects by the contact resistance.

$$J = J_{diff} + J_{\mathrm{Rec}} + \frac{V - JR_s}{R_{sh}} = J_{S_1}(e^{\frac{q(V-JR_s)}{n_1KT}} - 1) + J_{S_2}(e^{\frac{q(V-JR_s)}{n_2KT}} - 1) + \frac{V - JR_s}{R_{Sh}} \qquad (37)$$

where J_{diff} = diffusion current, J_{Rec} = recombination current, R_s = series resistance, R_{sh} = shunt resistance, J_{s1} = saturation current due to diffusion, J_{s2} = saturation current due to recombination, V= applied voltage, n_1 = ideality factor in diffusion and n_2 = ideality factor in recombination. The photodiode, taking into account the diffusion, recombination and parasitic effect, can be represented as follow:

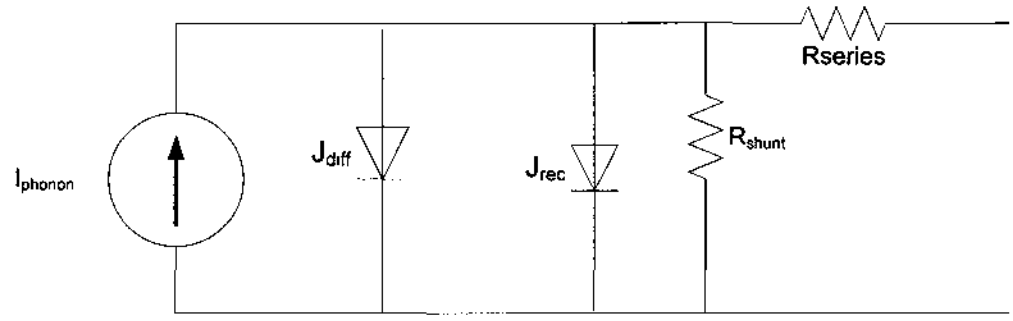

Figure 67. Circuit representation of a photodiode with recombination and diffusion currents and shunt and series resistances indicated

From the schematic model in Figure 67, it is apparent that one way to improve the photodiode behavior is to modulate the recombination current. This can be achieved by biasing the substrate. By applying a negative bias on the p-type Si substrate, the holes in the Si are attracted towards the bottom of the Si while the electrons are repelled from it. As a result, the depletion region is modulated and the recombination current is further reduced. The photodiode current is mainly dependent on the diffusion current. However, a positive bias on the substrate increases the recombination current, hence a much larger saturation current flows. This method can be used in conjunction with the surface cleaning to achieve improved performance in the UV photodiode. Figure 68 shows the effect of biases on the ALD ZnO/Si photodiodes. Positive bias on the Si shifts the I-V curve down. With a positive bias of voltage higher than 2 *V*, irradiation with light onto the photodiode has no effect on the current. On the other hand, negative bias on the Si substrate improves the photodiode rectifying characteristics. A negative voltage bias of -2 *V* achieved the optimum rectifying characteristics. In summary, heterojunction n-ZnO/p-

Si photodiodes can be employed as a UV photodetector. High efficiency ALD ZnO photodiodes have been fabricated and measured. The quantum efficiency improves with O_2 plasma ashing of the as deposited ALD ZnO. This is due to the fact that O_2 surface treatment reduces the surface recombination sites and provides a better metal-semiconductor interface. The diode can be tuned from a photosensitive diode to a regular rectifier by just applying bias on the Si substrate.

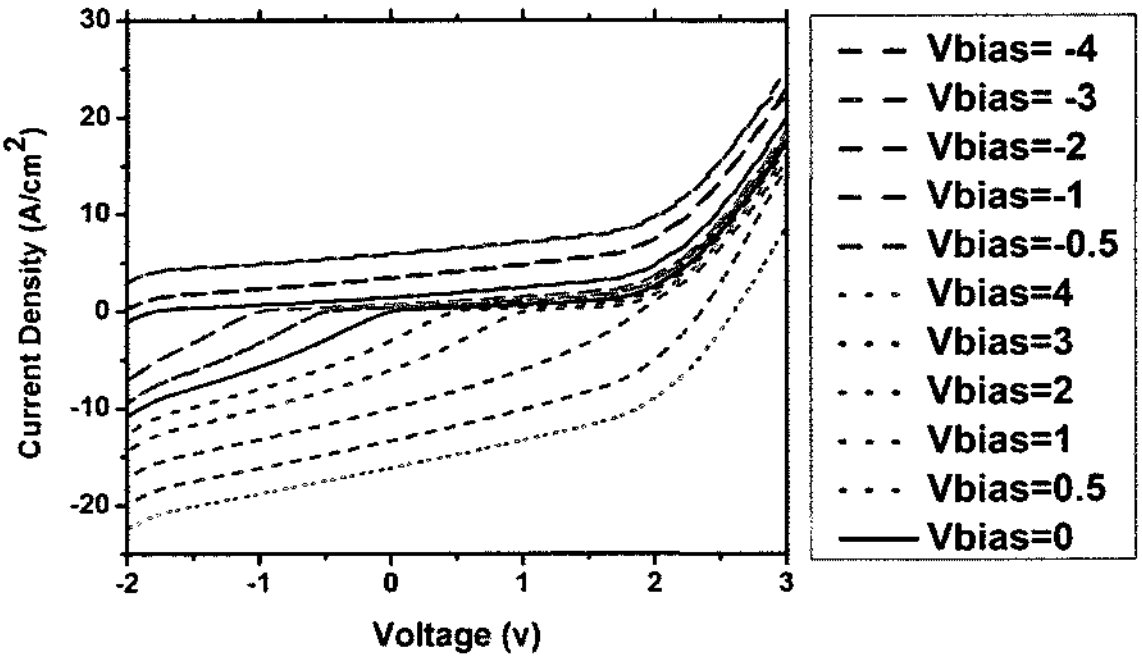

Figure 68. I-V characteristics of Ti/ZnO/Si photodiodes. (dash line) Negative biases. (dot line) Positive biases.

CHAPTER 6

SUMMARY AND FUTURE WORK

6.1 SUMMARY

ZnO is a versatile material that is attracting a lot of attention due to its numerous technologically interesting properties. It is a wide bandgap material with numerous properties. ZnO exhibits strong UV emission as well as related defect emission in the visible range. The UV emission peak in ZnO structures is explained by band-edge emission principle. On the other hand, the defect related emissions are observed in the green, yellow, red/orange, blue, and violet ranges. However, the origin of the defect emissions is still a largely unresolved issue in the optical properties of ZnO and subject to debate in the technical literature. In addition to elucidating the root cause of those defects, it is important to reduce and control the defect level in ZnO. In this study, ALD ZnO thin films were successfully deposited using diethyl zinc and H_2O as precursors. The deposition parameters were developed and optimized resulting in an ALD process window of 100 ^oC - 160 ^oC. The ALD ZnO films were characterized structurally, optically and electrically.

Good quality ZnO thin films were synthesized by atomic layer deposition. Our analysis reveals that ALD ZnO follows a Volmer-Weber type film growth. This growth mode can consistently explain the experimental results for varying with temperature and for different substrate materials. Once a nucleation site has formed, subsequent ALD cycles contribute to the growth of the crystallites resulting in appreciable grain growth.

The as-deposited ALD ZnO thin films were found to be polycrystalline with preferential growth direction in the (002) or in the c-axis for the hexagonal wurtzite crystallographic phase. As the film thickness increases from 239 ALD cycles to 1900 ALD cycles, the intensity of the (002) peak increases. The as-deposited (002) peak intensity increased with temperatures. This observation was consistent regardless of annealing ambient gas. In summary, the ALD ZnO crystal quality was improved by annealing. The built-in stress was characterized for the samples annealed in N_2, O_2 and room ambient. Annealing in N_2 ambient produced the lowest overall stress. During annealing in O_2 ambient gas, the concentration of the intrinsic defects responsible for the electrical properties such as oxygen vacancy and zinc interstitials is reduced; hence, an increase in resistivity is observed. The Raman spectroscopy study revealed a red shift in the Raman peak, which is indicative of built-in tensile stress. Our measurements show the appearance of the E_2 (high) optical phonon at frequency of 446.33 cm^{-1} for the thickest ZnO films. The peak at 384.75 cm^{-1} corresponds to the A_1 (TO) mode. There was no indication of any LO phonons; however, several phonon peaks at 280.93, 1343.6 and 1422.8 cm^{-1} were observed. The bulk single crystal ZnO sample exhibits a sharp E_2 (high) optical phonon mode at 442 cm^{-1}. In contrast to the polycrystalline ALD ZnO thin films, the ZnO single crystal did not display the A_1(TO) optical phonon. E_1 optical phonon mode was detected for neither bulk single crystal nor the ALD ZnO sample. The peak at 236 cm^{-1} for both bulk single crystal ZnO and ALD ZnO thin films might be due to intrinsic defects. The ALD ZnO showed broader peaks of the A_1(TO) than the single crystal bulk ZnO. Polycrystalline films tend to result in broader peaks compared to single crystal materials. The broader peak can be attributed to formation of the misfit and twin dislocation. The

stress increases with increasing ALD ZnO thickness up to a critical thickness and then begins to decrease. The critical thickness is dependent not only on the lattice parameters but also on the Poisson ratio. The optical bandgap was determined to be ~3.22 *eV*. The thin films exhibited very good electrical conductivity and transmission of 88 % - 90 % in the visible range. The as-deposited films showed n-type conductivity with a carrier density of ~10^{19} cm^{-3}. Such high carrier density results in a degenerate semiconductor. The defects responsible for the measured electrical and optical properties were identified in a series of experiments. Oxygen vacancies and Zn interstitials complexes were found to be the major defect levels in the forbidden bands. ALD ZnO/Si based UV photodetectors were fabricated, tested, analyzed and optimized. The measurements revealed a QE of 38.48 % for Al/ZnO/Si photodiodes and 41.83 % for Pt/ZnO/Si photodiodes for the as-deposited samples at a wavelength on 380 *nm* which matches exactly the band edge of our ALD ZnO films. The QE was found to increase after O_2 plasma treatment of the ZnO surface to around a value of 49.05 % and 52 % for Pt and Al respectively. Even though as-grown ALD ZnO films exhibit intrinsic defects in the films, high quantum efficiency was obtained. Different methods have been proposed to further improve the performance of the ALD ZnO based electronic devices.

6.2 Future Work

Due to the lack of reproducible p-type ZnO, achieving good homojunction ZnO-based photodiodes such as UV-photodetectors remains a big technological challenge. ZnO is an n-type semiconductor material with numerous intrinsic defects levels responsible for the electrical and optical behaviors. Reducing those intrinsic defects will result in higher device efficiency for heterojunction photodiodes. Because of the lattice mismatch between Si and ZnO, the grown ZnO layer will exhibit some additional extrinsic defects in the film. ZnO has a smaller lattice constant than Si and is thus under tensile stress. When the grown thickness exceeds the critical thickness, the film relaxes by generating defects. One way to improve the crystal structure is to grow the ZnO layer on a buffer layer such as ZnS. The lattice constant of ZnS is 5.42 Å which represents a lattice matched system with Si (0.18 % mismatch). ZnS is a wide bandgap direct semiconductor with a bandgap about that of ZnO. Thus, by introducing oxygen in ZnS to form $ZnO_{1-x}S_x$, the lattice constant of the ternary compound is further reduced to match that of ZnO. ZnO can be grown on Si using a buffer system such as the one described above which would result in defect-free film. This can help to increase the efficiency measurements. Another possible improvement in the growth of ALD ZnO is through confining the defects. This has been demonstrated with growing GaAs on Si.[81] Li et al have demonstrated defect pinning through SiO_2 masking.[81] Figure 69 shows the mechanism of ALD ZnO with SiO_2 masking. A SiO_2 layer is grown and patterned on a Si substrate wafer. Then, the ALD ZnO films are deposited on the structured sample. The lattice mismatch between the Si and ZnO places some stress on the growing ZnO film. As the film relaxes, defects are created and propagate. The presence of SiO_2 patterned structures pinned those defects

and stop them from propagating. After a certain intermediate thickness, defect free films can be grown which would result in higher efficiency ALD ZnO/Si UV photodetectors.

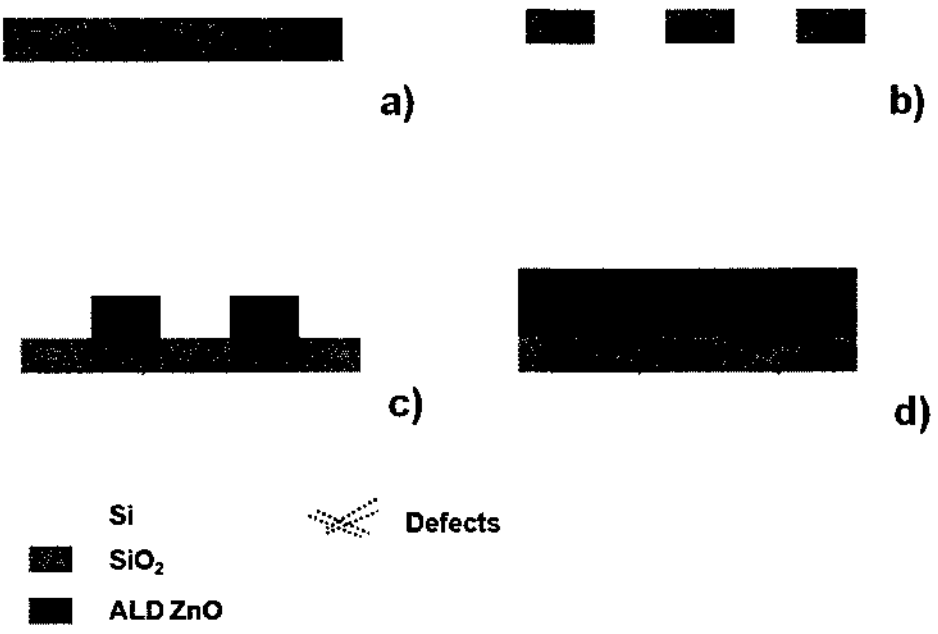

Figure 69. Proposed defect pinning in ALD ZnO on Si substrates. a) Deposition of SiO_2 layer on Si. b) Patterning of the SiO_2 Layer. c) Deposition of the ALD ZnO layer. d) defects are pinned by the SiO_2 layer.

Above all, designing homojunction photodiodes on top of p-type ZnO will result in much higher efficiency. Another advantage of forming a homojunction is the prevention of the native oxide underneath the device layer as seen in Figure 63 and the lattice matching issue. Therefore, depositing p-type ZnO is critical to homojunction ZnO p-n diodes. One way of growing p-type ZnO is through doping by group V elements such as N, As, P. One doping implementation is through ion implantation. Due to the high

concentration of native intrinsic defects, multiple implantation doses and depths are necessary to limit the doping compensation by the intrinsic defects of ALD ZnO. Figure 70 shows the implantation profile of P ions in ZnO using different ion energy and fluence. Due to the low solubility of P in ZnO, only very small ion fluence can be used.

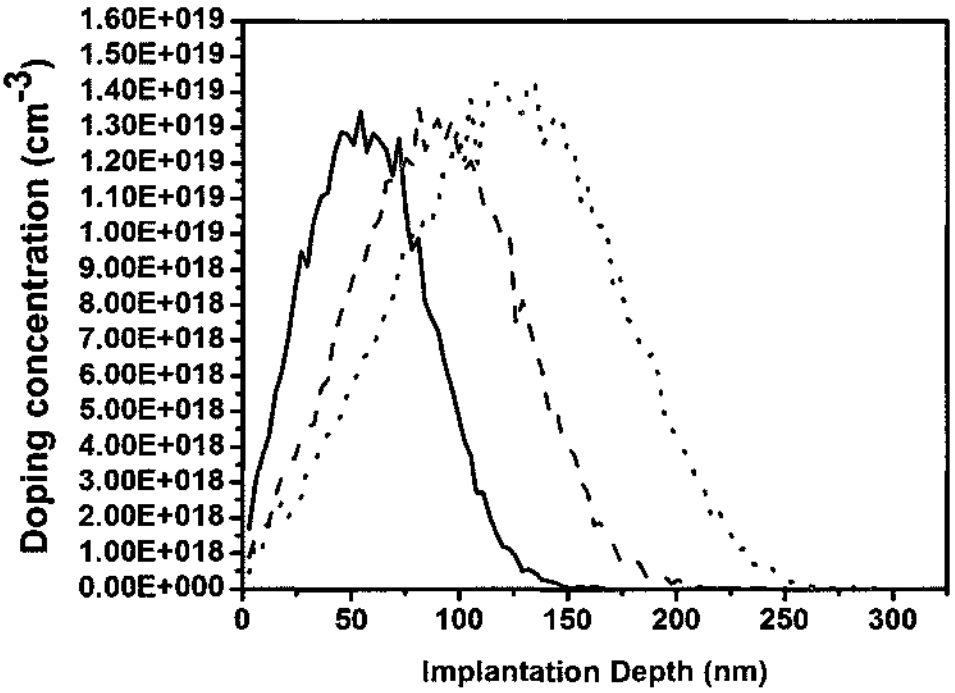

Figure 70. Phosphor ion implantation simulation at various implantation fluences. (solid) 1.4×10^{14} cm^{-2} P-fluence at 80 *KeV.* (dash line) 1.2×10^{14} cm^{-2} P-fluence at 110 *KeV.* (dotted line) 1.8×10^{14} cm^{-2} P-fluence at 150 *KeV.* The simulations were done using a SRIM software.

Dopant activation temperature and ambient is also critical. Therefore, two activation methods are proposed:

- Rapid thermal annealing

  RTA uses high power tungsten lamps to evenly increase the temperature of the sample from 50 $^{o}C/s$ to 120 $^{o}C/s$. The fast increase in temperature limits the compensation effect from the ALD ZnO; however, the long inconvenient cooling time is the drawback of the RTA annealing method.

- Pico and Femto secondLaser quenching

  Fast laser pulses from femtosecond lasers (Ti:sapphire) or picosecond laser can be used to rapidly anneal and electrically activate the dopants in the ALD ZnO sample and quench the profile down super fast. This method shows the most significant way to electrically activate samples such as the implanted ALD ZnO and to stop and prevent carrier compensation by intrinsic defects. The drawback of laser annealing is the slow process due to the small laser size. This is time consuming particularly for big samples.

Another doping method that can be achieved through the ALD deposition is the use of three chemical precursor lines instead of two. The other two chemical precursor lines are similar to the ALD ZnO deposition with H_2O and diethyl zinc. The third precursor line can be used as a supply of NH_3 gas. By controlling the dose of NH_3 gas in between cycles and the deposition temperature, N doping could be achieved hence p-type doping.

Nanostructures offer a few advantages over thin films due to their high surface areas. Designing ZnO nanotube photodiodes on Si can result in higher efficiency. ZnO

was deposited into anodic aluminum oxide (AAO) pores with an aspect ratio of 300 (pore diameter: 200 *nm*, depth: 60 μm) by ALD. A conformal and complete ZnO coating inside the AAO pores was achieved by extended exposure time for the precursors during deposition. SEM pictures of the nanotubes are shown in Figure 71. The fully release nanotubes can be deposited on Si wafers to form p-n junctions.

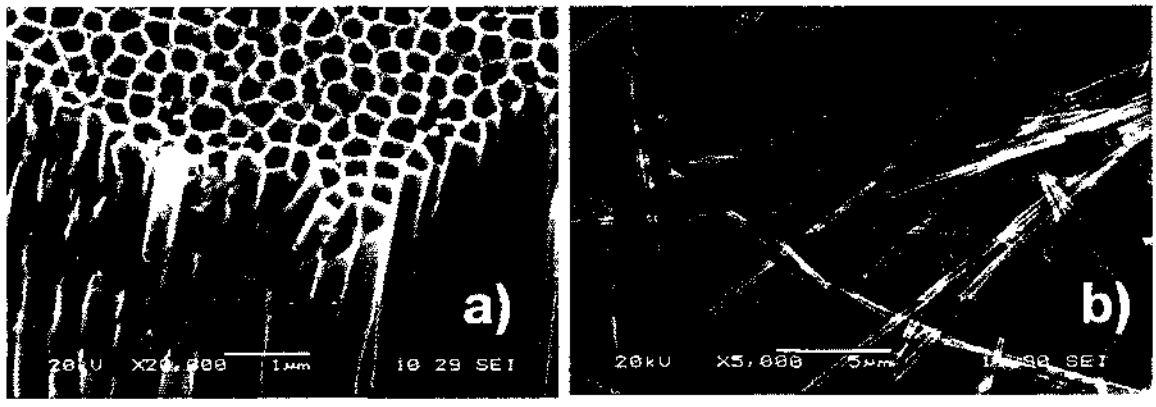

Figure 71. SEM picture of ALD ZnO nanotubes. (Top) high magnification of partially release nanotubes. (bottom) fully release ALD ZnO nanotubes.

6.3 Applications

A potential application of the ALD ZnO is in the lighting industry. Trichromatic RGB mixtures of phosphors for white light, either for cathodoluminescent (CL) applications such as BLU or ESL, or for photoluminescent (PL) applications, such as compact fluorescent (CFL) or near-UV LED, typically use a red component of Y_2O_3:Eu or Y_2O_2S:Eu, depending on the degree of saturation desired. Although these compounds represent the best red phosphors available, they suffer from diminishing efficacy and

lifetime with increasing power density. The severe loss in efficacy is a result of the poor thermal and electrical conductivity (in CL use) of Y_2O_3:Eu particles. The situation is worsened in that most white-light applications need to be operated at high power densities. Furthermore, phosphor screens often employ silicate binders for adherence to the glass lamp, further diminishing thermal conductivity. The first demonstration of coating of Y_2O_3:Eu red phosphor powder with ALD ZnO is presented here. ALD provides unique features such as precise thickness control of ZnO thin films with atomic resolution, high uniformity and absolute conformity. As demonstrated in this dissertation the as deposited thin films exhibit very high conductivity and transparency in the visible range. ALD is capable of coating complex surface morphologies capable to penetrate minute voids. A thin layer of red phosphor powder was deposited on a Si substrate by sedimentation technique and coated with a 100 nm thick film of ALD ZnO at 150 ^{o}C. Figure 72 is an SEM image of loosely packed red phosphor particles and shows that every single red phosphor particle was coated with 100 *nm* ZnO including the Si substrate. After coating the red phosphor, the four-point probe measurements revealed very low resistivity (~0.02 Ω-*cm*) for the as-deposited 100 *nm* ALD ZnO thin films. The photoluminescence study revealed a bright red emission of $Y_2O_3:Eu^{2+}$. After coating with ALD ZnO, the photoluminescence measurements show that the red emission of $Y_2O_3:Eu^{2+}$ is conserved, as shown in Figure 73. The results demonstrate that not only can the silicate binder be replaced with luminescent ZnO, but thermal and electrical conductivity can be enhanced, in order to improve efficacy, lifetime, and thermal stability, by the same process. The preliminary results suggest a 30 % increase in the

efficiency from the cathodoluminescence measurements of the red phosphors coated by ALD ZnO.

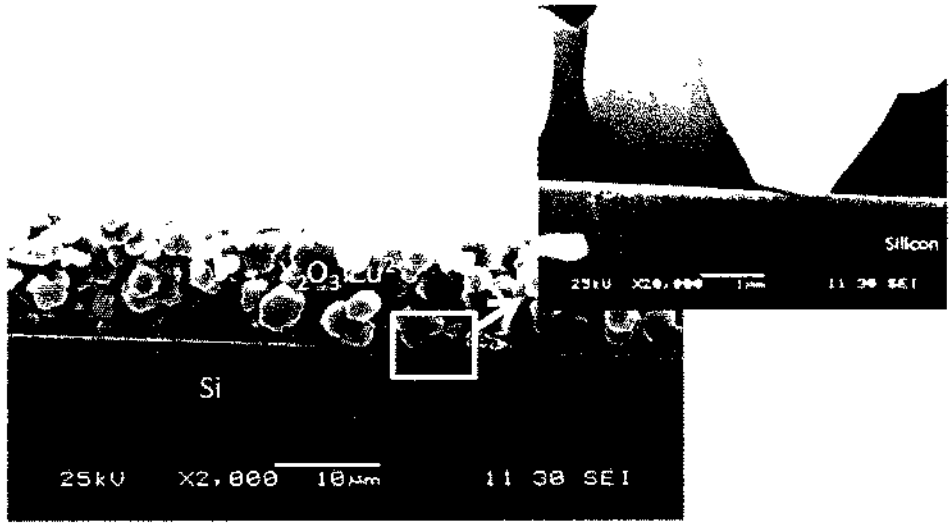

Figure 72. SEM image of (a) loosely packed $Y_2O_3:Eu^{2+}$ particles deposited by sedimentation and (b) higher magnification of $Y_2O_3:Eu^{2+}$ particles coated with 100 *nm* of ALD ZnO film.

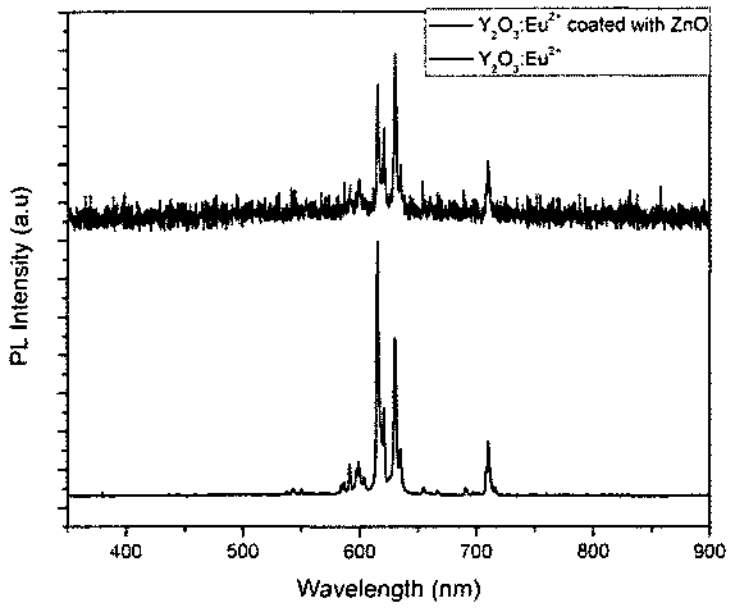

Figure 73. Photoluminescence measurement of red phosphor without ALD ZnO coating and with ALD ZnO.

REFERENCES

[1] C. A Arguello, D. L Rousseau, S. P. S Porto, "First-Order Raman Effect in Wurtzite-Type Crystals", *Phys. Rev*, **181**(3), 1351-1363 (1968).

[2] L. Stolt, J. Hedstrom, J. Kessler, V. Ruckh, K. U Velthaus, H. W Shock, "ZnO/CdS/$CuInSe_2$ thin-film solar cells with improved performance", *Appl. Phys. Lett.*, **62**, 597-599 (1993).

[3] C-Y. Lee, H-T. Haung, W-F. Su, C-F. Lin, "Electroluminescence from ZnO nanoparticles/organic nanocomposites",*Appl. Phys. Lett.*, **89**, 231116-1 - 231116-3 (2006)

[4] A. Ohtomo, K. Tamura, M. Kawasaki, T. Makino, Y. Segawa, Z. K Tang, G. K. L. Wong, Y. Matsumoto, H. Koinuma, "Room-temperature stimulated emission of excitons in ZnO/(Mg,Zn)O superlattices", *Appl. Phys. Lett.,* **77** 2204-2206 (2000).

[5] F. P. Koffyberg, "Thermoreflectance spectra of CdO: Band gaps and band-population effects",*Phys. Rev.B*, **13**, 4470-4476 (1976).

[6] Y.F Hsu, A.B. Djuris˘ic´, K.H. Tam, "Morphology and optical properties of ZnO nanostructures grown underzinc and oxygen-rich conditions", *J. Cryst. Growth*, **304**, 47-52 (2007).

[7] P.-A. Hu, Y.-Q. Liu, L. Fu, X.-B. Wang and D.-B. Zhu, "Creation of novel ZnO nanostructures: self-assembled nanoribbon/nanoneedle junction networks and faceted nanoneedles on hexagonal microcrystals", *Appl. Phys. A,* **78**, 15-19 (2004).

[8] A.B. Djurišić, Y.H. Leung, K.H. Tam, L. Ding, W.K. Ge, H.Y. Chen and S. Gwo," Green, yellow, and orange defect emission from ZnO nanostructures: influence of excitation wavelength", *Appl. Phys. Lett.*, **88**, 103107:1-3 (2006).

[9] B.D. Yao, Y.F. Chan, N. Wang, " Formation of ZnO Nanostructures by a Simple Way of Thermal Evaporation", *Appl. Phys. Lett.*, **81**, 757-759 (2002).

[10] C.S. Lao, P.X. Gao, R.S. Yang, Y. Zhang, Y. Dai, Z.L. Wang, "Formation of double-side teethed nanocombs of ZnO and self-catalysis of Zn-terminated polar surface" *Chem. Phys. Lett.*, **417**, 359-363 (2005).

[11] Y. Dai, Y. Zhang, Q.K. Li, C.W. Nan, "Synthesis and Optical Properties of Tetrapod-like Zinc Oxide Nanorods*", Chem. Phys. Lett.*, **358**, 83-86 (2002).

[12] T. J Hsueh, C. L Hsu, S. J Chang, Y. R Lin, T. S Lon, I. C Chen, "Growth and Characterization of Sparsely Dispersed ZnO Nanowires", *J. Electrochem. Soc*, **154**, H153-H156 (2007).

[13] J-H Kim, H. Song, E. K Kim, S. Lee, Y. Shon, "Electrical Properties of Zn(Mn,Co)O Films Grown by Pulsed Laser Deposition Method", *ECS Transactions,* **16**, 27-31 (2008).

[14] B. Bayraktaroglu, K. Leedy, *ECS Transactions,* "Pulsed Laser Deposited ZnO for Thin Film Transistor Applications", **16**, 61-73 (2008).

[15] M. J Zheng, L.D Zhang, G. H Li, W. Z Shen, "Fabrication and optical properties of large-scale uniform zinc oxide nanowire arrays by one-step electrochemical deposition technique", *Chem. Phys. Lett,* **363**, 123-128 (2002).

[16] M. Haupt, A. Ladenburger, R. Sauer, K. Thonke, R. Glass, W. Roos, J. P Spatz, H. Rauscher, S. Riethmuller, M. J Moller, "Ultraviolet-emitting ZnO nanowhiskers prepared by a vapor transport process on prestructured surfaces with self-assembled polymers",*J. Appl. Phys*, **93**, 6252-6257 (2003).

[17] N. Yoshii, A. Nakamura, S. Hosaka, J. Temmyo, "Controlled Structure of Zinc Oxide by Means of Side Flow Type MOCVD", *ECS Transactions*, **16**, 3-11 (2008).

[18] A. Bakin, A. Wagner, E. Schlenker, B. Postels, M. Al-Suleiman, A. Behrends, A-H Elshaer, V. Petukhov, A. Waag, "ZnO Nanostructures and Thin Layers for Device Applications", *ECS Transactions,***16**, 107-115 (2008).

[19] S. J Lim, S. Kwon, H. Kim, "ZnO thin films prepared by atomic layer deposition and rf sputtering as an active layer for thin film transistor", *Thin Solids Films,***516**, 1523-1528 (2008).

[20]D. M King, X. Liang, C. S Carney, L. F Hakim, P. Li, A. W Weimer, "Atomic Layer Deposition of UV-Absorbing ZnO Films on SiO_2 and TiO_2 Nanoparticles Using a Fluidized Bed Reactor", *Adv. Funct. Mater.*, **18**, 607-615 (2008).

[21] S. Singh, P. Thiyagarajan, K. M Kant,D. Anita, S. Thirupathiah, N. Rama, B. Tiwari,M. Kottaisamy, M. S.R Rao, "Structure, microstructure and physical properties of ZnO based materials in various forms: bulk, thin film and nano", *J. Phys. D: Appl. Phys.*, **40**, 6312-6327 (2007).

[22] U. Ozgur, Y.I Alivov, C. Liu, A. Teke, M.A Reshchikov, S. Douan, A. Avrutin, S.J Cho, H. Morkoc, "A comprehensive review of ZnO materials and devices", *J. Appl. Phys.*, **98**, 041301 :1-103 (2005).

[23] K. Vanheusden, C. H. Seager, W.L. Warren, D.R Tallant, J.A Voigt, " Correlation between photoluminescence and oxygen vacancies in ZnO phosphors", *Appl. Phys. Lett.*, **68**, 403-405 (1996).

[24] A.Van Dijken, E.A Meulenkamp, D. Vanmaekelbergh, A. Meijerink, " The kinetics of the Radiative and Nonradiative Processes in Nanocrystalline ZnO Particles upon Photoexcitation", *J. Phys. Chem.B*, **104**, 1715-1723 (2000).

[25] A.B. Djuris˘ic´ , W.C.H. Choy, V.A.L. Roy, Y.H. Leung, C.Y. Kwong, K.W. Cheah, T.K. Gundu Rao, W.K. Chan, H.F. Lui, C. Surya, "Photoluminescence and EPR of ZnO tetrapod structures", *Adv. Funct. Mater.*, **14**, 856-864 (2004).

[26] S. A Studenikin, N. Golego, M. Cocivera, "Optical and electrical properties of undoped ZnO films grown by spray pyrolysis of zinc nitrate solution", *J. Appl. Phys.*, **83**, 2104-2111 (1998).

[27] V.A.L. Roy, A.B. Djurisic , W.K. Chan, J. Gao, H.F. Lui, C. Surya, "Luminescent and structural properties of ZnO nanorods prepared under different conditions", *Appl. Phys. Lett.*, **83**, 141-143 (2003).

[28] C. G. Van de Walle, " Hydrogen as a Cause of Doping in Zinc Oxide", *Phys. Rev. Lett.*, **85**, 1012-1015 (2000).

[29] A.B.M.A. Ashrafi, I. Suemune, H. Kumano, S. Tanaka, "Nitrogen-Doped p-Type ZnO Layers Prepared with H_2O Vapor-Assisted Metalorganic Molecular-Beam Epitaxy", *Jpn. J.Appl. Phys.*, Part 2 41, L1281-L1284 (2002).

[30] A. S. H. van der Heide, A. Schonecker, J. H. Bultman, W. C. Sinke, " Explanation of High Solar Cell Diode Factors by Nonuniform Contact Resistance", *Prog. Photovolt: Res. Appl.*, **13**, 3-16 (2005).

[31] T. S Suntola, J. Antson, A. Pakkala, S. Lindfors, *SID 80 Dig*, 11, 108 (1980).

[32] A. Sherman, *Atomic Layer Deposition for Nanotechnology*, P.1, Ivoryton Press, CT (2008).

[33] J.S. Becker, Phd. Thesis, Department of Chemistry and Chemical Biology, Harvard University, Cambridge, MA (2002).

[34] M. Ritala, M. Leskela, *Handbook of Thin Film Materials*, edited by H. S. Nalwa, 1, 103, Academic Press, San Diego, Ca (2002).

[35] J. N Hilfiker, B. Singh, R.A Synowicki, C.L Bungay, "Optical characterization in the vacuum ultraviolet with variable angle spectroscopic ellipsometry: 157 nm and below", *Proc. SPIE*, **3998**, 390-398 (2000).

[36] C. R Brundle, C. A. Evans, S. Wilson, *Encyclopedia of Materials Characterization*, Butterworth-Heinmann, p.99 (1992).

[37] A. C Fisher-Cripps, *Nanoindentation,* P.16, Springer, NY (2004).

[38] E. Guziewicz, I. A. Kowalik, M. Godlewski, K. Kopaliko, V. Osinniy, A. Wojcik, S. Yatsunenko, E. Lusakowska, W. Paszkowicz, M. Guziewcz, "Extremely low temperature growth of ZnO by atomic layer deposition", *J. Appl. Phys.*, **103,** 033515:1-6 (2008).

[39] H.G Thompkins, W.A McGahan, *Spectroscopic Ellipsometry and Reflectometry*, John Wiley & Sons, Inc., New York, 1999, p.93.

[40] J.A Venables, G.D. T Spiller, M. Hanbucken, "Nucleation and Growth of Thin Films", *Rep. Prog. Phys.*, **47**, 399-459 (1984).

[41] B.B Mandelbrot, D. E Passoja, A. J Paullay, "Fractal Character of Fracture Surfaces of Metals", *Nature*, **308,** 721-722 (1984).

[42] W. Zahn, A. Zosch, "Fractal dimension of thin-film surfaces obtained by Fourier spectral analysis", *Surf. Interface. Aanalysis*, **25**, 488-491 (1997).

[43] G. Guisbiers, O. Van Overschelde, M. Wautelet, P.h Leclere, R. Lazzaroni, "Fractal dimension, growth mode and residual stress of metal thin films", *J. Phys. D: Appl. Phys.*,**40**, 1077-1079 (2007).

[44] T-H Fang, S-R Jian, D-S Chuu, "Nanotribology and fractal analysis of ZnO thin films using scanning probe microscopy", *J. Phys. D: Appl. Phys.*, **36**, 878-883 (2003).

[45] http://nanotec.es

[46] I. Horcas, R. Fernández,J. M. Gómez-Rodríguez,J. Colchero,J. Gómez-Herrero,A. M. Baro, "WSXM: A software for scanning probe microscopy and a tool for nanotechnology", *Rev. Sci. Instrum.*,**78**, 013705:1-8 (2007)

[47] Andre Guinier, X-ray diffraction in crystals, imperfect crystals, and amorphous bodies, Courier Dover Publications, p. 124 (1994)

[48] H. Morkoc, U. Ozgur, Zinc Oxide Fundamentals, Materials and Device Technology,Wiley VCH, p.50 (2009).

[49] R B Roberts, "Thermal expansion reference data : silicon 300-850K", *J. Phys. D: Appl. Phys.*, **14,** L163-166 (1981).

[50] R. Hong, J Huang, H. He, Z. Fan, J. Shao, "Influence of different post-treatments on the structure and optical properties of zinc oxide thin films", *Appl. Surf. Sci,* **242**, 346-352, (2005).

[51] N.C. Hosking, M.A. Strom, P.H. Shipway, C.D. Rudd, "Corrosion Resistance of Zinc-Magnesium Coated steel", *Corrosion Science*, **49**, 3669-3695 (2007).

[52] W.S. Baer, "Faraday Rotation in ZnO: Determination of Electron Effective Mass", *Phys. Rev.*, **154**, 785-789 (1967).

[53] I. Hamberg, C.G. Granqvist, K.-F. Berggren, B.E. Sernelius, L. Engström, "Band-gap Widening of in Heavily Sn-doped In_2O_3", *Phys. Rev. B*, **30**, 3240-3249 (1984).

[54] K.J. Button, C.G. Fonstad, W. Dreybrodt," Determination of the Electron Masses in Stannic Oxide by Submillimeter Cyclotron Resonance", *Phys. Rev. B*, **4**, 4539-4542 (1971).

[55] J.F Wager, "Transparent electronics: Schottky barrier and heterojunction considerations", *Thin Solid Films*, **516**, 1755-1764 (2008).

[56] V. A. Coleman, J. E. Bradby, ,C. Jagadish, M. R. Phillips, "Observation of enhanced defect emission and excitonic quenching from spherically indented ZnO", *Appl. Phys. Lett.*, **89**, 082102:1-3 (2006).

[57] C. A Arguello, D. L Rousseau, S. P. S Porto, "First Order Raman Effect in Wurtzite-Type Crystals", *Phys. Rev*, **181**, 1351-1363 (1969).

[58] Y. Gu, X. Lia, W. Yu, X. Gao, J. Zhao, C. Yang, "Microstructures, electrical and optical characteristics of ZnO thin films by oxygen plasma-assisted pulsed laser deposition", *J. Cryst. Growth*, **305,** 36-39 (2007).

[59] K. Tapily, D. Gu, H. Baumgart, "Growth Mechanism of ALD ZnO Films Investigated by Physical Characterization", *ECS Transactions,* **33,** 355-363 (2010).

[60] M. Tzolov, N. Tzelov, D. Dimova-Malinovska, C. Pizzuto, G. Vitali, G. Zollo, I. Ivanov, "Vibrational properties and structure of undoped and Al-doped ZnO films deposited by RF magnetron sputtering", *Thin Solid Films*, **379**, 28-36 (2000).

[61] K. Mcguire, Z. W Pan, Z. L Wang, D. Milkie, J. Menendez, A. M Rao, "Raman studies of semiconducting oxide nanobelts", *J. Nanosci. Nanotech*, **2**, 499-502, (2002).

[62] S. Desgreniers, "High-density phases of ZnO: Structural and compressive parameters", *Phys. Rev. B*, **58**, 14102-14105 (1998).

[63] H. Ruf, A.G Evans, "Toughening by Monoclinic Zirconia", *J. Am. Ceram. Soc.*, **66**, 328-332 (1983).

[64] H-K Yoon, Y-S Yu, "Hardness and elastic modulus of ZnO deposited materials by PLD method", *International Symposium on Electronics Materials and Packaging*, **EMAP 2005**, 169-173 (2005).

[65]S.O Kucheyev, J. E Bradby, J. Williams, C. Jagadish, M. V Swain, "Mechanical deformation of single-crystal ZnO", *Appl. Phys. Lett.*, **80**, 956-958 (2002).

[66]A. C Fischer-Cripps, 2nd ed. (Springer-Verlag, Berlin, Germany, 2002), pp.164.

[67] S Ruffell, J E Bradby, J SWilliams, D Munoz-Paniagua, S Tadayyon, L L Coatsworth, P. R Norton, "Nanoindentation-induced phase transformations in silicon at elevated temperatures", *Nanotechnol.*, **20**, 135603:1-5 (2009).

[68]J. Yan, H. Takahashi, X. Gai, H. Harada, J. Tamaki, T. Kuriyagawa, "Load effects on the phase transformation of single-crystal silicon during nanoindentation tests", *Mater. Sci. Eng. A*, **423**, 19-23 (2006).

[69] V. Domnich, Y. Gogotsi, S. Dub, "Effect of phase transformations on the shape of the unloading curve in the nanoindentation of silicon", *Appl. Phys. Lett.*, **76**, 2214-2216 (2000).

[70] T.Y. Tsui, G.M. Pharr, "Substrate effects on nanoindentation mechanical property of soft film on hard substrate ", *J. Mater. Res.*, **14**, 292-301 (1999).

[71] W-S. Lee, F-J. Fong, "Microstructural study of annealed gold–silicon thin films under nanoindentation", *Mater. Sci. Eng. A*, **475**, 319-326, (2008).

[72]D.S. Stone, "Elastic Rebound between an Indenter and a Layered Specimen I: Model", *J. Mater. Res.*, **13**, 3207-3213 (1998).

[73] K. Narayandas, M. Radhakrishnan, C. Balasubramanian, "Defect Density and Electrical Properties of Vacuum Evaporated Copper Films From Annealing Studies of Electrical Resistance", *Electrocomp. Sci. Technol.*, **9**,171-178 (1982).

[74] **N.** Artunç, S. Selvi, Z.Z. Öztürk**,** "The effects of surface and interface scattering on the electrical resistivity of Cu/Ag double-layered thin films", *Thin Solid Films,* **221,**207-213 (1992).

[75] B. Vincent Crist, Handbooks of Monochromatic XPS Spectra: Commercially Pure Binary Oxides, **2**, pp. 821, Wiley (1999).

[76] J.C Simpson, J.F Cordaro, "Characterization of deep levels in zinc oxide", *J. Appl. Phys.*, 63, 1781-1782 (1988).

[77]A. Rohatgi, S. K. Pang, T.K Gupta, W. D. Straub, "The deep level transient spectroscopy studies of a ZnO varistor as a function of annealing", *J. Appl. Phys.*, **63**, 5375-5379 (1988).

[78] D. C. Look, "Recent advances in ZnO materials and devices", *Mater. Sci. Eng. B*, **80**, 383-387 (2001).

[79] L. A. Kosyachenko,1, G. V. Lashkarev, V. M. Sklyarchuk, A. I. Ievtushenko, O. F. Sklyarchuk, V. I. Lazorenko, A. Ulyashin, "ZnO-based photodetector with internal photocurrent gain", *Phys. Status Solidi A*, **207**,1972-1977 (2010).

[80] Y. I. Alivov, Ü. Özgür, S. Dogan, D. Johnstone, V. Avrutin, N. Onojima, C. Liu, J. Xie, Q. Fan, H. Morkoç, "Photoresponse of n-ZnO/p-SiC heterojunction diodes grown by plasma-assisted molecular-beam epitaxy", *Appl. Phys. Lett.*, **86**, 241108:1-3 (2005).

[81] J. Z. Li, J. Bai, J-S. Park, B. Adekore, K. Fox, M. Carroll, A. Lochtefeld, Z. Shellenbarger, "Defect reduction of GaAs epitaxy on Si (001) using selective aspect ratio trapping", *Appl. Phys. Lett.*, **91**, 021114:1-3 (2007).

APPENDIX A

THEORETICAL CALCULATION OF BAND ALLIGNMENT

Position of Fermi level in ZnO with respect to the conduction band

$$E_{FN} = \frac{KT}{q}\ln(\frac{N_D}{N_C})$$

Similarly, Position of Fermi level in Si from the valence band:

$$E_{Fp} = \frac{KT}{q}\ln(\frac{N_A}{N_V})$$

Where $N_C = 2\left(\frac{2\pi m_n^* KT}{h^2}\right)^{3/2}$ and $N_V = 2\left(\frac{2\pi m_p^* KT}{h^2}\right)^{3/2}$ are the effective density of states of conduction and valence band respectively.

See material properties for N_c and N_v values for both ZnO and Si.

$$E_{FN} = 0.026\ln(\frac{1.7\times10^{19}}{3\times10^{18}}) = 0.0451eV$$

Position of Fermi level in Si from the valence band:

$$E_{Fp} = 0.026\ln(\frac{1.33\times10^{16}}{1.04\times10^{19}}) = 0.17327eV$$

Or E_{Fp}= 1.12 – 0.17327 = 0.947 eV from conduction band of Si.

Workfunction calculation

$$\phi_{ZnO} = 4.5 - 0.045 = 4.45eV$$

$$\phi_{Si} = 4.05 + 0.947 = 4.9967eV$$

Band offsets using Anderson's rule for ideal heterojunction

$$\Delta E_C = \chi_{ZnO} - \chi_{Si} = 4.5 - 4.05 = 0.45eV$$

$$\Delta E_g = Eg_{ZnO} - Eg_{Si} = 3.22 - 1.12 = 2.10eV$$

$$\Delta E_V = (\chi_{ZnO} + Eg_{ZnO}) - (\chi_{Si} + Eg_{Si}) = \Delta E_c + \Delta Eg = .45 - 2.08 = 2.55eV$$

Built-In voltage

$$V_{bi} = \phi_{ZnO} - \phi_{Si} = 4.45 - 4.9967 = -0.54673V$$

Depletion region

$$W = X_{ZnO} - X_{Si} = \sqrt{\frac{2\varepsilon_{ZnO}\varepsilon_{Si}(N_{ASi} + N_{DZnO})^2 V_{bi}}{qN_{ASi}N_{DZnO}(\varepsilon_{Si}N_{ASi} + \varepsilon_{ZnO}N_{DZnO})}} = 0.23077\mu m$$

$\varepsilon_{ZnO} = \varepsilon_0 k_{ZnO}$ and $\varepsilon_{Si} = \varepsilon_0 k_{Si}$

$$X_{ZnO} = w\frac{N_{ASi}}{N_{ASi} + N_{DZnO}} = 0.0018\mu m$$

$$X_{Si} = w\frac{N_{DZnO}}{N_{ASi} + N_{DZnO}} = 0.2305\mu m$$

$$C_j = \sqrt{\frac{q\varepsilon_{ZnO}\varepsilon_{Si}N_{ASi}N_{DZnO}}{2V_{bi}(\varepsilon_{Si}N_{ASi} + \varepsilon_{ZnO}N_{DZnO})}} = 4.488 \times 10^{-8} F/cm^2$$

Diffusion Length

Using Einstein relation, the diffusivity is :

$$D = \frac{kT}{q}\mu_n = 7.8cm^2/s$$

The diffusion length is:

$$L = \sqrt{D\tau} = 364nm$$

Where τ is the electron lifetime. For optimum device performance the deposited ZnO layer should be about the diffusion length (364 *nm*).

Barrier height of the different metal electrodes

$$J = J_s(e^{\frac{qV}{nKT}} - 1) = A^{**}T^2 e^{\frac{-q\phi_B}{KT}}(e^{\frac{qV}{nKT}} - 1)$$

Saturation current is:

$$\rightarrow J_s = A^{**}T^2 e^{\frac{-q\phi_B}{KT}} \rightarrow \phi_B = -\frac{KT}{q}\ln(\frac{Js}{A^{**}T^2})$$

Contact resistance

$$\rho_C = \left(\left.\frac{dJ}{dV}\right|_{V=0}\right)^{-1} \quad (\Omega\text{-}cm^2)$$

$$\rho_C = \frac{k}{qA^{**}T} e^{\frac{q\phi_b}{kT}}$$

Metal	*W*	*Ti*	*Pt*	*Al*
Barrier height (eV)	0.614	0.596	0.55	0.509
Workfunction (eV)	5.11	5.10	5.05	5.01

Ideality factor

$$J = J_s(e^{\frac{qV}{nKT}} - 1) \rightarrow \log(\frac{J}{J_s}) = \frac{qV}{nKT}\log e \rightarrow \log(\frac{J}{J_s}) = \frac{qV}{nKT}\log e \rightarrow n = \frac{q}{slopeKT}\log e$$

APPENDIX B

MATERIAL PROPERTIES

Properties	*ZnO*	*Si*
Bandgap (*eV*)	3.22	1.12
Nc (cm^{-3})	3×10^{18}	2.8×10^{19}
N_v (cm^{-3})	1.8×10^{19}	1.04×10^{19}
Dielectric constant	8.6	11.7
Carrier density (cm^{-3})	1.7×10^{19}	1.33×10^{16}
Electron affinity (*eV*)	4.5	4.05
Electron Mobility (cm^2/Vs)	34	1471
Hole Mobility (cm^2/Vs)	10	471
Electron lifetime (*s*)	1.7×10^{-10}	5×10^{-10}
Hole lifetime (*s*)	1.7×10^{-10}	5×10^{-10}
Electron velocity (*cm/s*)	225×10^{5}	270×10^{3}
Hole velocity (*cm/s*)	200×10^{4}	160×10^{3}
Modulus/Hardness (*GPa*)	143/6.5	130/12

APPENDIX C

SOURCE CODE

```
*title  ZnO/Si N-p Heterojunction
mesh    nx=250 xres=1.0
* layer N ZnO
layer   tm=0.40 nd=1.7e19 eg=3.25 nc=3e18
+       nv=1.8e19 ks=8.565 chi=4.5 un=34. up=1.
+       eaa=-1.0 ead=-1.0 taup.shr=1.7e-10 taun.shr=1.7e-10
+       et.shr=0.0 vsatn=2.25e7 vsatp=0.2e7
* layer p Si
layer   tm=1 na=1.0e16 eg=1.12 nc=2.8e19
+       nv=1.04e19 ks=11.7 chi=4.05 un=1417. up=471.
+       eaa=-1.0 ead=-1.0 taup.shr=5.0e-10 taun.shr=5.0e-9
+       et.shr=0.0 vsatn=2.7e5 vsatp=1.6e5
* Boundary condidtion wdfrt= workfunction metal - affinity semiconductor
BC      MBC=2   wdfrt=0.7 wdbck=0.94
i-v     vstart=0.0 vstop=2.0 dv=0.05
solve   itmax=100
output  info=5 step=1
```

VITA

EDUCATION

Doctor of Philosophy in Electrical and Computer Engineering May 2011
Old Dominion University, Norfolk, VA
Dissertation title: Synthesis of ALD ZnO and Thin Film Materials for UV Photodetector Applications.
Bachelor of Science in Electrical Engineering, Magna Cum laude May 2006
Minor: Computer Engineering
Old Dominion University, Norfolk, VA
Fundamentals of Engineering (FE) Certification May 2006

HONORS,AWARDS & MEMBERSHIPS

Electrochemical Society Electronic & Photonics Division Best Poster Award, ECS Fall Meeting, Las Vegas, NV 2010
NJIT/NSF 2010
PhD Research Award Old Dominion University 2010
Electrochemical Society Travel Grant Award 2007-2010
Electrochemical Society Electronis & Photonics Division Student Research Award, ECS Fall Meeting, Honolulu, Hawaii 2008
Senior Design II Contest 3rd Place and Design III 2nd place 2005&2006
Virginia Microelectronics Consortium Scholar 2005
The Edgar and Kathleen Kovner Scholarship 2005
Honors College Scholarship 2003-2006
Outstanding International Sophomore Award Old Dominion University 2002
Electrochemical Society ECS Student Member 2007-Present
Tau Beta Pi (TBP) Engineering Honor society member 2003-Present

List of Publications

JOURNAL PUBLICATIONS (7 Proceedings with 2 listed)

- **K. Tapily**, J. Jakes, D.S. Stone, P. Shrestha, D. Gu, H. Baumgart, A.A Elmustafa, "Nanoindentation Investigation of HfO_2 and Al_2O_3 Films Grown by Atomic Layer Deposition", *Journal of Electrochemical Society,* 155, p.H545, (2008).
- D. Gu, **K. Tapily**, P. Shrestha, M.Y Zhu , G. Celler, H. Baumgart, Experimental study of ALD HfO_2 deposited on strained Silicon-on-insulator (sSOI & xsSOI) and SOI", *Journal of Electrochemical Society,* 155, p.G129, (2008).

CONFERENCE PROCEEDINGS (19 Proceedings with 1 listed)

- **K. Tapily**, A. Sneha Raj, et al., "Hall Effect, DLTS, C-V Characterization of ALD HfO_2 and ZnO Thin Films", *ECS Transaction*, 33 (3), 281 (2010).